2.4 Measurements at AUG

2.4.1 AUG July/August 1999 (30 keV pure He-beam)

Our first He beam emission measurements were parasitic. As described in chapter 2.1 a pure He beam at half the nominal energy was injected at the end of the heating beam injection for 200 ms. The conversion of one PINI to He operation was possible for an experimental program with low NBI power needs. This was the case for the investigation of neo-classical tearing-modes (NTMs) where pulses with only 3 MW NBI heating power were used.

The CER diagnostic was needed for the ion temperature measurements. However, not all of its fibres (viewing lines) are used by the spectrometer, therefore it was possible to connect four CER-fibres to a spectrometer from the Li-beam (LIB) diagnostics which remains unused for normal operation. For about 20 pulses He was injected, and the LIB spectrometer was set to the wavelength of one of the n = 3→2 or n = 4→2 HeI transitions for each pulse. In that way the 11 most intensive visible HeI lines [29] were covered, but no HeI beam emission signal could be identified.

Unfortunately, it was discovered later that the image amplifier has not been working, and the sensitivity of the CCD sensor on its own was not high enough to resolve the beam emission signal.

For some repetitive pulses it was not necessary to measure the ion temperature for each pulse, therefore the CER diagnostic could be used to measure the HeI beam emission. In that way the beam emission profile of three HeI lines (see Tab. V) could be measured with the CER spectrometer. These results were presented in [29].

AUG pulse	wavelength [nm]	HeI transition	beam energy [keV]	equi. beam current [A]	maximum intensity of beam emission
12635	502 nm	2^1S-3^1P	27 keV	14.2 A	1.7 e19 ph/m³s
12643	587.6 nm	2^3P-3^3D	27 keV	14.2 A	50.0 e19 ph/m³s
12644	667.8 nm	2^1P-3^1D	27 keV	14.2 A	4.0 e19 ph/m³s

Tab. V: Observed HeI transitions, beam parameters, and maximum intensity of the beam emission profiles for three successful pulses of the first campaign at AUG.

The intensity of the Doppler-shifted beam emission was weak and the resulting emission profile had a large scatter. As for the viewing lines close to the plasma edge the Doppler-shift was too small, the beam emission peak could not be separated from the unshifted passive emission from the edge. Therefore the plasma edge was outside the accessible radial region, and it was also not possible to identify the beam emission as an increase of the total emission (shifted plus unshifted).

2.4.2 AUG Mai 2000 (60 keV doped He/D-beam)

After the first campaign at AUG (chapter 2.4.1) successful measurements with a He/D-doping system have been made at JET (chapter 2.5.1). Consequently a similar system has been installed at AUG in April 2000. Between 25/4/2000 and 8/6/2000 the new system was tested and HeI beam emission measurements have been carried out.

The He/D doping system can be used for parasitic measurements without restrictions to the NBI heating power. By installing the doping system at the ion source Q3 the accessible radial range could be extended (details see chapter 2.1).

For the beam emission measurements the CER spectrometer was needed, therefore only pulses where the ion temperature measurements have not been needed could be used for our parasitic experiments. Furthermore, we were interested in a series or repetitive pulses, in order to obtain a set of comparable beam emission profiles. The ideal candidate meeting these requirements was the standard H-mode pulse.

Standard H-mode discharge

The AUG standard H-mode pulse is routinely performed during the start-up sequence of AUG. It is well characterised and the measurement of the ion temperature is not necessary. Fig. 2.23 shows the time trace of some important signals of the standard H-mode discharge #13665.

AUG pulse number	13646	13665	13667	13782	time [s]
stored energy [MJ]	0.589	0.594	0.625	0.562	3.5
heating power [MW]	4.88	4.87	4.88	4.94	3.5
density [10^{19} 1/m^3]	*6.29*	5.13	5.27	5.12	3.5
stored energy [MJ]	0.567	0.537	0.56	0.558	6.3
heating power [MW]	4.76	4.86	4.84	4.85	6.3
density [10^{19} 1/m^3]	*12.5*	10.26	10.32	10.38	6.3

Table VI: Reproducibility of the AUG standard H-mode pulse at low density.

The two flat top phases, one with a line average density of $5{\cdot}10^{19}$ m^{-3} between 2.5 and 4.5 s, and another one with a line average density of 10^{20} m^{-3} between 5.5 and 7 s, had been used for the HeI beam emission measurements. The stored energy of the AUG plasma is roughly the same in both periods, which means that the electron temperature is correspondingly lower in the high density phase of the discharge. Helium gas for producing a doped He/D beam was injected into the ion source between 3.5 and 3.7 s and between 6.1 and 6.3 s. The reproducibility of the discharges was very good with only one pulse (#13646) showing a 20 % higher density in table VI. The standard H-mode pulse was used for measuring the beam emission of all visible He lines which were accessible (the spectrometer could not be set to wavelengths above 7000 Å).

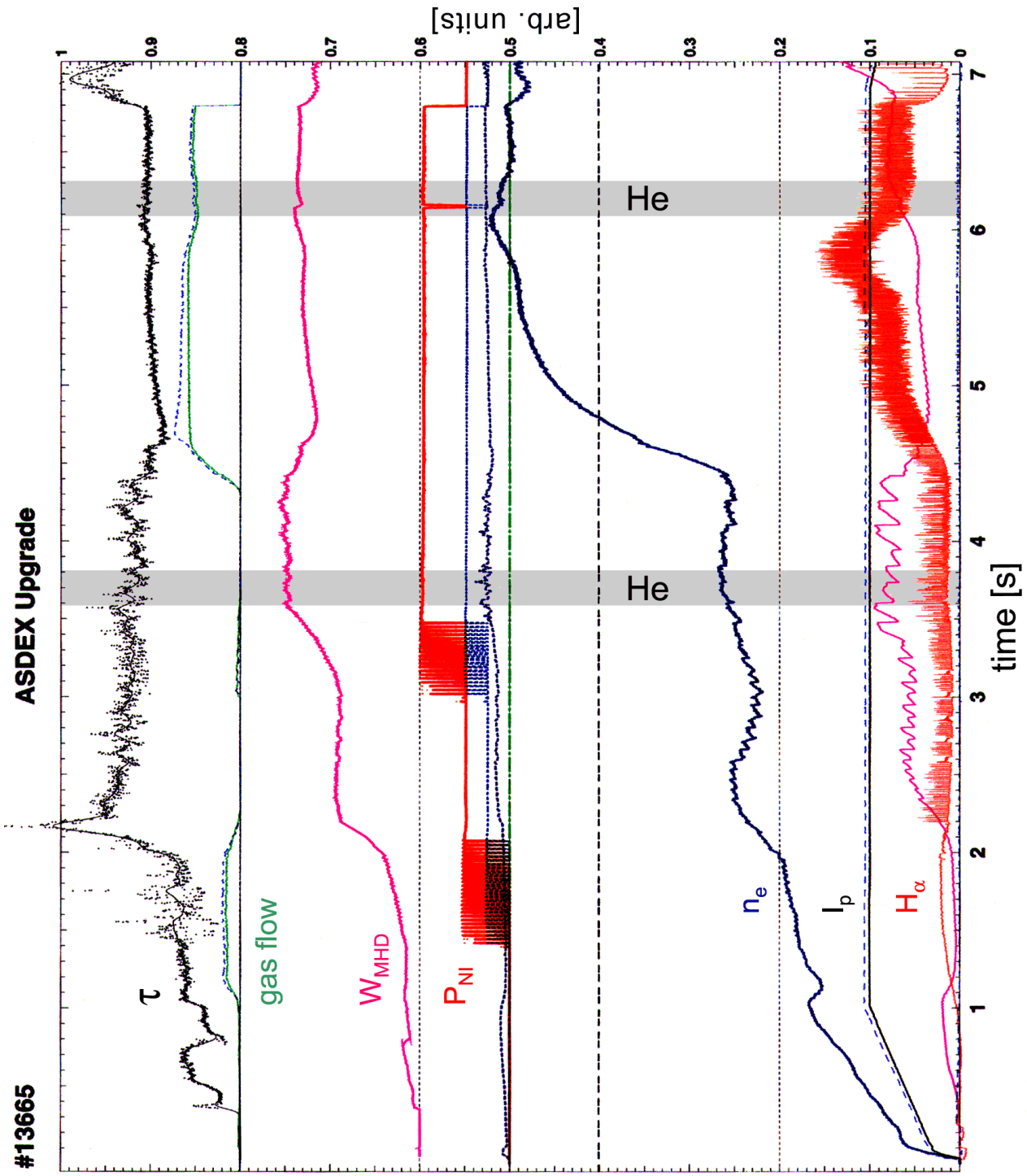

Fig. 2.23: Plasma parameters of the AUG standard H-mode discharge #13665. He doping, marked by grey bars, was performed at 3.5 and 6.1 s. The transition into H-mode at t = 2 s is characterised by an increase in confinement (stored energy W_{MHD}, confinement time τ, and electron density n_e).

Other abbreviations: P_{NI} ....injected neutral beam power
I_p .....plasma current
H_α ....passive plasma H_α-emission (ELM-activity).

The ramp-up of the plasma current up to Ip = 1 MA occurs during the first second of the discharge (ohmic phase). Subsequently the NBI heating power is being ramped up between 1.4 and 2.1 s to about 3.75 MW (on/off modulation). At t = 2.2 s the transition into the H-mode occurs. This can be seen from the significant increase of the energy confinement time τ from 0.06 to 0.13 s and the increase of the stored energy up to W_{MHD} = 0.36 MJ. The plasma density (electron density n_e) increases as well, although the gas flow decreases at the same time, indicating an increased particle confinement. For a short time after the L-H-transition the energy confinement time goes up to τ = 0.2 s, and is lost again shortly thereafter with the first ELM-event. The ELMs (edge localised modes) can be identified from the H_α-signal (Balmer-alpha line at 656 nm), which increases during an ELM-event when the unstable plasma edge collapses.

During the first flat-top phase (t = 2.5 - 4.5 s) the average plasma density settles at $n_e = 5 \cdot 10^{19}\ m^{-3}$. This means that during this phase the density is above the set-point and only defined by the gas flux from the wall. From t = 3 to 3.5 s the beam power is ramped-up to 7 MW.

After the second power ramp-up the first He injection into the ion source was triggered.

After t = 4.4 s the control parameter for the plasma density is doubled ($n_e = 1 \cdot 10^{20}\ m^{-3}$). This can also be seen in the gas flow. At about t = 5.5 s the density of the second flat-top phase is reached and kept constant till t = 7 s.

Other discharges at AUG

Emission from the strongest He lines could also be measured in two other discharges that are characterised in table VII.

pulse & number		time [s]	stored energy [MJ]	heating power [MW]	density [1/m^3]
Killer pellet	#13647 / 8	2.5	0.476	4.99	$5.09 \cdot 10^{19}$
ITB	#13742 / 3	1.6	0.64	5.38	$4.18 \cdot 10^{19}$

Table VII: Main plasma parameters of two further AUG pulses with He beam emission data

The “killer pellet pulse” is a pulse driven towards a high-density disruption and then terminated by a killer pellet. The increase of the density starts at 2.9 s, termination with the pellet occurs shortly before 6 seconds. Helium for the doped beam was injected into the ion source before the density rise at 2.5 s. At his time the discharge is a flat-top H-mode discharge without additional gas fuelling and consequently very similar in density to the first phase of the standard H-mode pulse.

The second pulse type was a so-called ITB discharge. A characteristics for this type of discharge is that additional heating is already supplied during the current rise phase. At the time of the He injection (1.6 s) there is no additional gas fuelling. The density is lower than in the case of the standard H-mode pulse, while the stored energy is higher.

Density profiles

Density profiles can be obtained from different diagnostics. The signal "DCN+Li" from the ddf-database is a combination of the profile obtained from several laser channels of the Interferometry (DCN) and the profile delivered by the Li beam diagnostics (limited to the scrape-off layer). The profile is smoothed and regarded as most reliable. Thomson scattering and reflectometry are other diagnostics yielding density profiles. Not all diagnostics are available for every pulse and the range of some diagnostics can be limited. For some pulses the Thomson scattering system was moved to view the divertor and was therefore not available for evaluation of the core plasma.

The density profile can normally be well presented by

$$n(\rho) = n_0 \times (1+\alpha\rho^2) \times \begin{cases} 1 & \text{for } \rho < \rho_s \\ \left(1 - e^{-\frac{\rho-\rho_s}{\lambda}}\right) & \text{for } \rho \geq \rho_s \end{cases} \qquad \begin{array}{l} \rho \text{ .... normalised flux radius} \\ \rho_s \text{ .... radial position of step in profile} \end{array} \tag{3}$$

as Fig. 2.24 shows by using interferometric data.

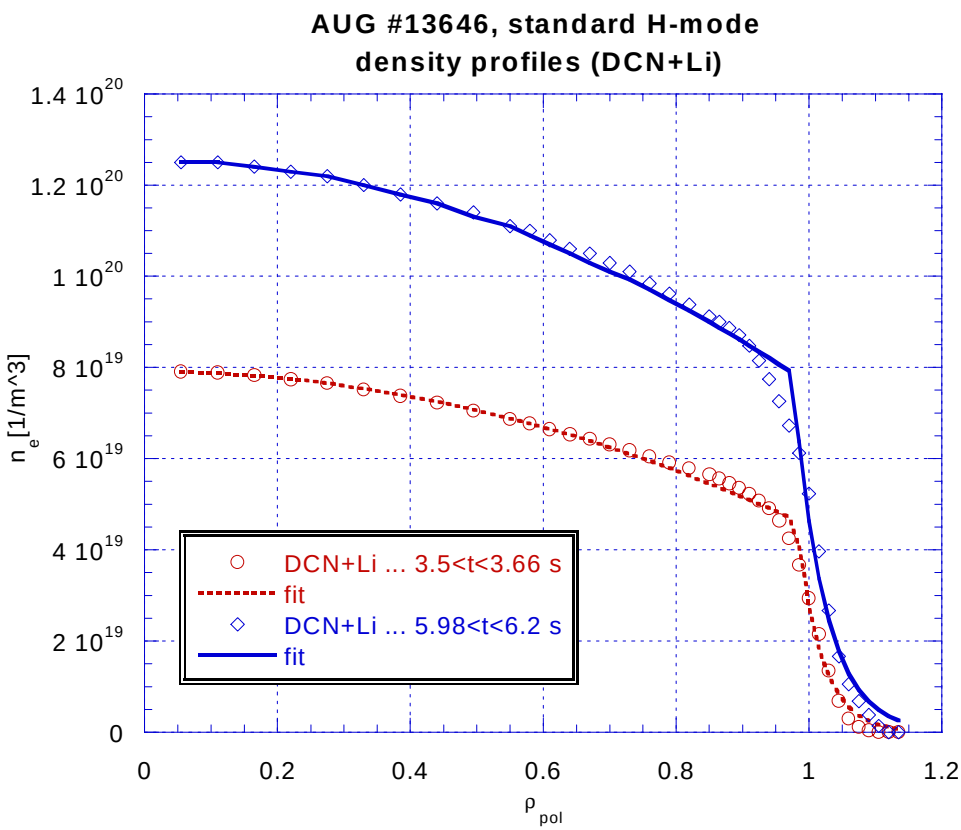

Fig. 2.24: AUG standard H-mode. Density profiles at 3.6 and 6 s taken from DCN and Li beam diagnostics at time intervals with He doped beam.

Temperature profiles

At AUG the main diagnostics for electron temperature profiles are Thomson scattering and the ECE radiometer. From Thomson scattering also a fitted profile called "Thomson fit" is stored in the AUG ddf database. When available, the "Thomson fit" data is being used for the temperature profile. For pulses without Thomson fit data the ECE radiometer data looks most promising, although its scatter can be considerable.

Fig. 2.25 shows the electron temperature profile for the standard H-mode pulse #13665 as derived from Thomson scattering data.

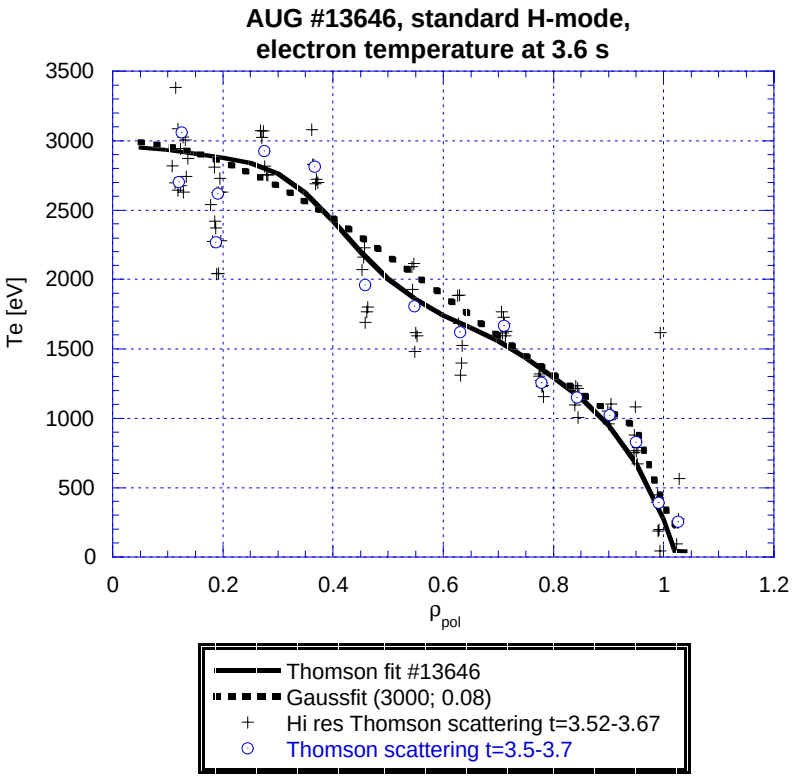

Fig. 2.25: Electron temperature profile for the standard H-mode discharge #13646 at t = 3.6 s. Symbols are straight data from Thomson scattering (standard and high resolution), the fit is from the standard Thomson scattering. Data points and Thomson fit show a centrally peaked profile. However, also a Gauß fit is consistent with the data due to its large scatter.

HeI beam emission for the standard H-mode discharge

The straight HeI beam emission profiles show a high systematic scatter. As described in chapter 3.6, this can be explained by the alignment of the CER diagnostic to the beam and is being corrected. Even for the most intensive singlet line the signal intensity was close to the noise level, leading to a considerable scatter in the beam emission profile. For evaluation of the HeI spectra we used the standard CER fitting routine (`cer_wid`), which was not optimised for our requirements.

Figs. 2.26 and 2.27 show the corrected beam emission profiles for the most intensive singlet (2^1P-3^1D) and triplet (2^3P-3^3D) line measured during the low density phase of standard H-mode discharges. In order to obtain a smoother profile, an average over 3 measurements from 3 equivalent discharges has been made as shown in Fig 2.26.

The singlet beam emission measurement can be reproduced by the model calculations if an initial population of the metastable 2^1S state of 1% is assumed. For these model calculations `scotty_fwd` was used, with n_e and T_e from Fig. 2.24 and 2.25 mapped onto the He beam axis.

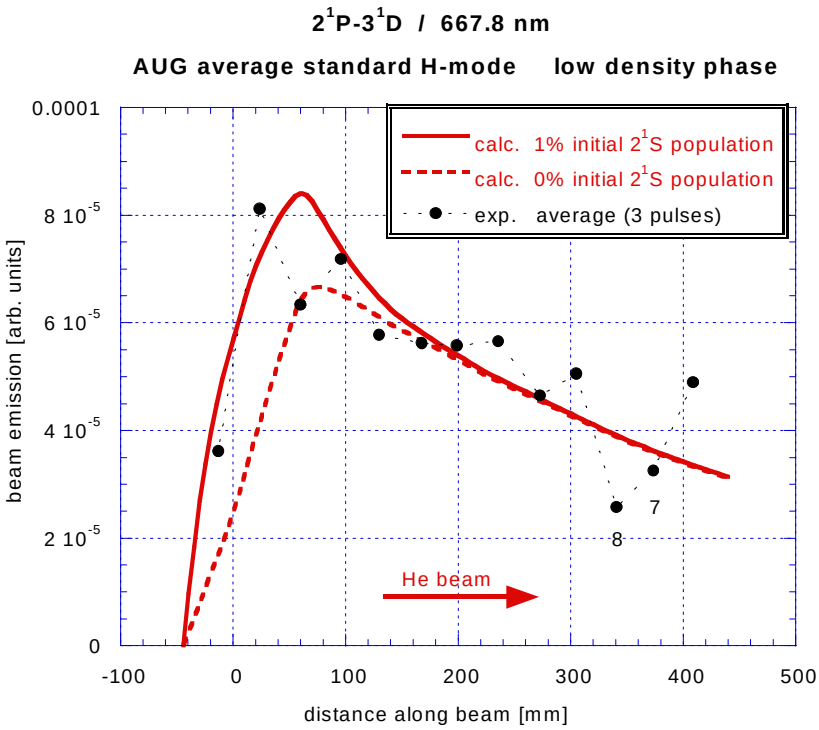

Fig. 2.26: He beam emission measurements (average over AUG #13646, #13667, #13880) and modelling of the HeI transition 2^1P-3^1D (667.8 nm). The measurements can be reproduced by the model calculations if an initial population of the 2^1S state of 1% is assumed.

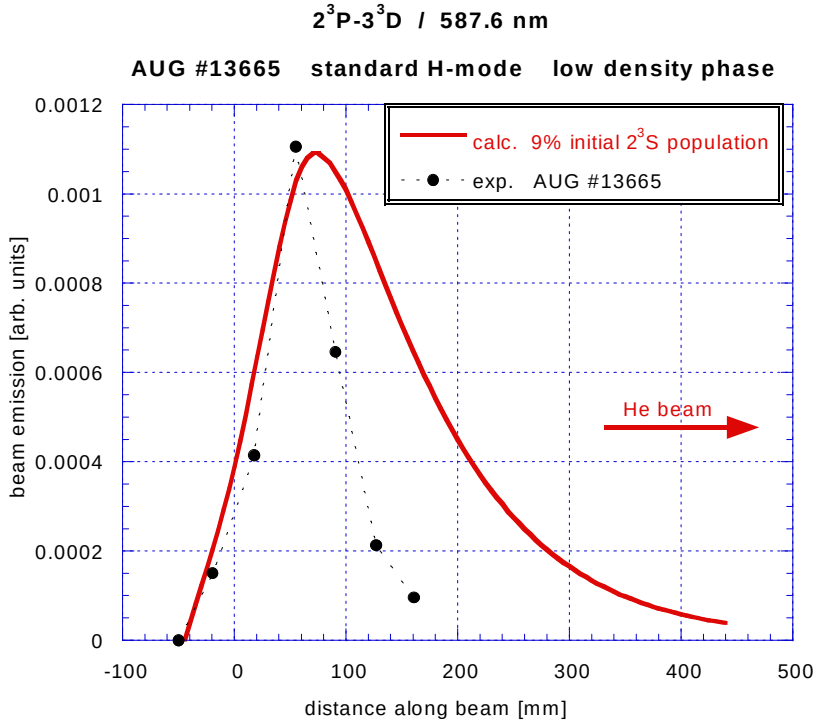

Fig. 2.27: Beam emission measurement and modelling of the HeI transition 2^3P-3^3D (587.6 nm) for the AUG discharge #13665. The obvious discrepancy in the curve width is discussed in chapter 2.6.3.

The two points labelled in Fig. 2.26 with their fibre numbers 7 and 8 show a clear tendency of too low values for different discharges and wavelengths. See also Fig. 3.12 in chapter 3.6. This could be due to calibration errors for these channels.

In Fig 2.27 an obvious discrepancy between the curve width of the measured and the calculated profile can be seen. This problem is discussed in chapter 2.6.3.

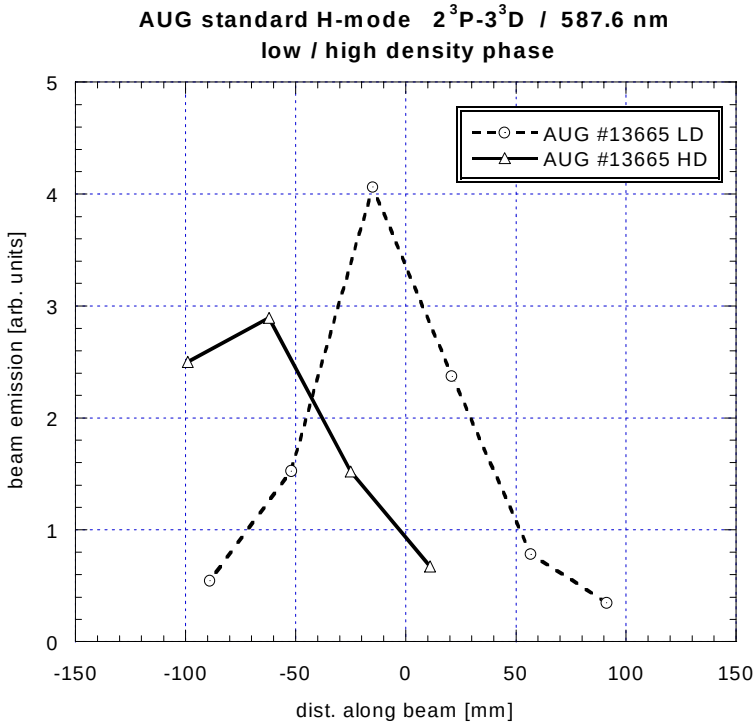

Fig. 2.28: Comparison of the triplet HeI beam emission (2^3P-3^3D) for low and high density phase.

The profiles measured during the high density phase are shifted relative to the profiles measured during the low density phase by about 40 to 50 mm. In Fig 2.28 the triplet emission profiles from the low and the high density phase are plotted in the same graph. The abscissa is defined as the distance along the beam, where the position of the LCFS defines zero. For the high density case the position of the maximum emission appears to be moved outwards beyond the LCFS and only the decaying part of the emission profile is within the range of the CER lines-of-sight. In the low density case (Fig. 2.26 and 2.27) the position of the steep increase of the emission profile is in agreement with the model calculations. For the high density case the modelled emission profiles need to be shifted outwards to match the measurement. In the plot of Fig 2.29 good agreement between the measured data and the model calculation could be achieved with a shift of 40 mm. This shift could be explained by a mapping error (EFIT) or by an error in the density profile used for the modelling.

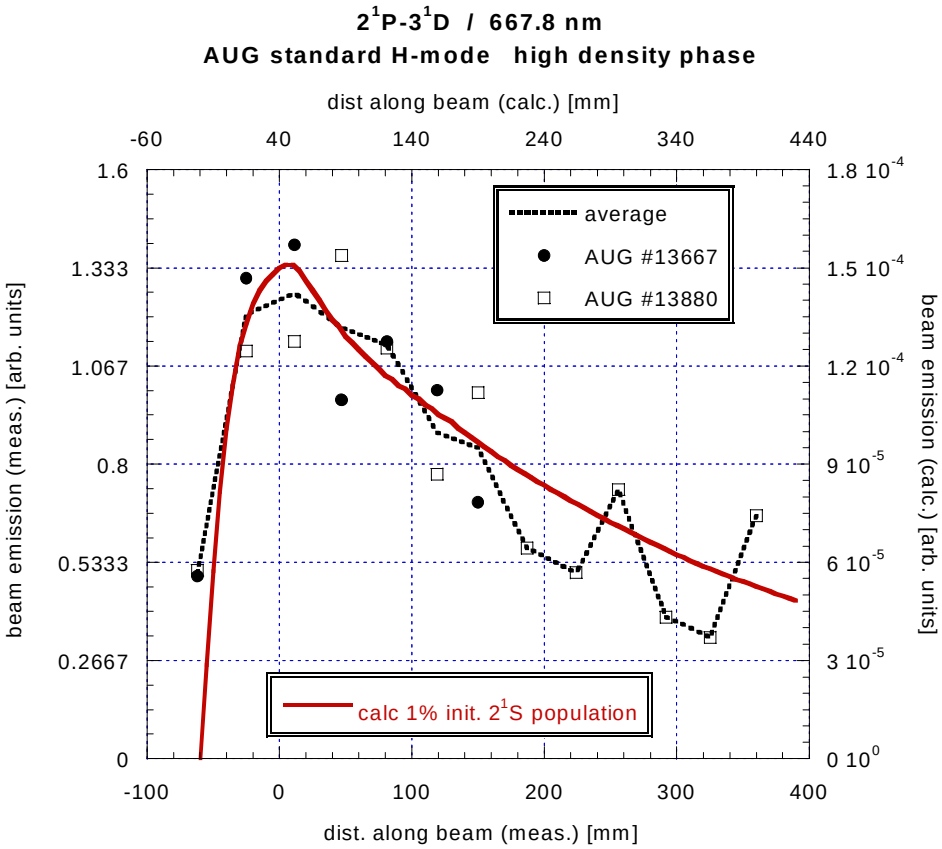

Fig. 2.29: Beam emission measurements (AUG #13667, #13880, and average) and modelling of the HeI line (2^1P-3^1D). The two abscissas (meas. and calc.) were shifted against each other by 40 mm.

2.4.3 Conclusions from Experiments at AUG

The generation of a fast He beam at AUG was achieved for both pure and doped D/He beams. The doped D/He beam had the advantage that the diagnostic PINI could be used for it, which provided a better viewing geometry giving access to a wider radial range. Another advantage was that the timing of the He doping is freely selectable and that the available NBI power stays unchanged. This gives access to relevant phases of a plasma discharge, whereas experiments using the pure He beam had to be scheduled at the end of the heating period.

Such beam emission experiments could be carried out parasitically with the only restriction that the CER diagnostic is not available for the ion standard temperature measurement.

The HeI lines 2^1P-3^1S, 2^3P-3^3S, and 2^3S-3^3P were not accessible due to technical limitations of the spectrometer. With regard to the other $n = 3 \rightarrow 2$ and $n = 4 \rightarrow 2$ HeI transitions, the sensitivity of the CER spectrometer was only high enough for the two strongest lines (transition 2^1P-3^1D at 667.8 nm and 2^3P-3^3D at 587.6 nm). For these two accessible lines we obtained beam emission profile for 4 different discharges and made repetitive measurements which allowed to estimate the error in the data to ±10%. This relatively high scatter is due to the low intensity of the signal. A systematic deviation of some channels indicates their non-perfect calibration.

The alignment of the beam to the CER viewing-lines was unfavourable and made an intensity correction of the different channels necessary. In particular, the outer lines-of-sight are very sensitive to misalignment. Furthermore, the intensity of the observed signal is lower.

The triplet emission was only measurable over the outer 200 mm of the plasma. This range is only roughly twice the range of the 50 kV lithium beam.

Since our last measurements the alignment and calibration of the CER diagnostic has been improved, which should lead to a higher beam emission signal and a lower scatter of the derived emission profile. The settings of the spectrometer (slit-width and exposure time) can be optimised in view to the signal intensity.

At JET a cross-calibration of neighbouring channels could be achieved by sweeping the plasma across the viewing-lines (see chapter 2.3.2). The application of this procedure to AUG is being investigated and would improve the achievable profile quality.

2.5 Measurements at JET

2.5.1 JET October/November 1999 (80 keV doped He/D-beam)

The He-doping system has been developed and tested at the JET test-bed [28] and was then first installed at PINI 6 of the octant 4 injector at JET in the beginning of October 1999 (for details see chapter 2.1). The doped He/D-beam was operated close to the nominal extraction voltage of the octant 4 injector of 80 kV, and He was injected into the ion source for 500 ms.

Wavelength scan of HeI lines (18/19. 10. 1999)

The aim of the first series of measurements was to asses the signal intensities of the modelled $n = 3 \rightarrow 2$ and $n = 4 \rightarrow 2$ HeI lines, and to investigate whether the He peak can be easily recognised and separated from other emission in the close spectral vicinity.

For observation of the HeI beam emission from the He-doped beam at octant 4 the KS7 spectrometer (CXRS) was used. Its observation system provides more fibres then the 16 used for the CX-measurements. Six spare fibres with suitable viewing-lines were connected to the single entrance slit of the 6-fibre setup of the spectrometer (details see chapter 2.2.2). The radial positions of the active volumes (cross-section of the beam and respective lines-of-sight) of the viewing-lines from the upper and the lower chords are given in Fig. 2.30. The positions corresponding to the six selected fibres are marked by solid dots. The expected Doppler-shift for the different viewing-lines is indicated by the grey triangles. No Doppler-shift occurs at a major radius $R_{maj} = 3.4$ m viewed by the upper and at $R_{maj} = 3.75$ m viewed by the lower cord. Within a radial range of about ± 100 mm of these positions the Doppler-shifts are too small and the Doppler shifted peak will overlap with the unshifted background emission. For this reason most of the viewing lines of the lower chords were not suitable for directly measuring a beam emission signal.

Using the 6-fibre setup had some advantages and disadvantages:

+ The switching between the standard setup (for CX) and the 6-fibre setup is very quick and only requires the turning of a mirror (by hand) and the changing of the wavelength setting (remote controlled) to switch over from CX-observation to HeI-observation and vice versa.
+ The spectral range is about 10 times higher compared to the standard setup and thus large enough to measure the Doppler shifted intensity and the unshifted intensity with similar sensitivity.
– 6 fibres are not sufficient for a profile measurement over the whole plasma range.

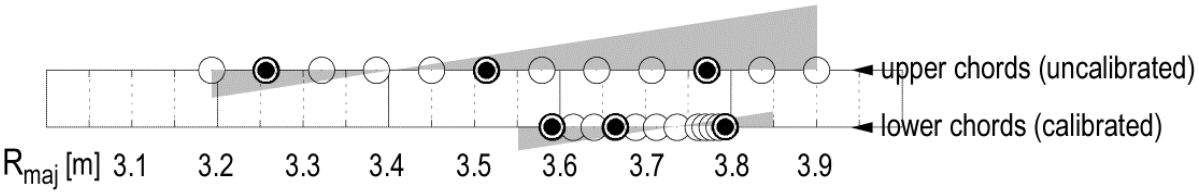

Fig. 2.30: Radial position of the active volumes for the viewing-lines of the KS7 diagnostic. The solid dots indicate the selected fibres for described measurements.

Using the KS7 diagnostic for the HeI beam emission measurements implied that the ion temperature (T_i) of the plasma edge could not be measured. For ten pulses dedicated to pellet experiments performed between 18. and 19. 10. 1999 the measurement of the edge-T_i was not required and KS7 could thus be switched to HeI beam emission. The HeI beam emission experiment were carried out with a doped deuterium/helium beam. Helium for the beam doping was injected during the flat-top phase of the discharge just before the first pellet was injected. The plasma parameters of these pulses, as shown in Tab. VIII varied considerably from pulse to pulse, as these experiments included plasma density- and heating power scans. Consequently, the electron density- and temperature profiles varied from pulse to pulse and the resulting HeI beam emission profiles were not directly comparable. However, in this way the observability of the HeI lines could be assessed.

JET pulse #	HeI transition	wavelength [nm]	P_{NBI} [MW]	P_{RF} [MW]	$n_e \cdot dl$ [10^{19} 1/m^2]
49029	2^1P-3^1D	667.8	6	-	11
49030	2^3P-3^3D	587.6	4.5	-	15
49031	2^3P-4^3D	447.1	5.4	-	14.6
49032	2^3P-3^3S	706.5	4.6	-	14.4
49044	2^1S-3^1P (502) 2^1P-4^1S (505)	503.0	1.16	7.0	19.6
49045	2^1P-3^1S	728.6	1.16	4.5	21.6
49046	2^3P-3^3D	388.9	1.16	4.5	22.2
49047	2^1P-4^1D	4920	1.16	4.5	23.7
49048	2^3P-3^3D	587.6	1.16	4.5	20.6

Tab. VIII: Wavelength settings of the KS7 spectrometer and plasma parameters of JET pulses used for the HeI beam emission measurements (18/19. 10. 1999). All discharges involved a toroidal magnetic field of B_t = 3.2 T and a plasma current of I_p = 2.5 MA. Grey font is used for pulses where the beam emission for the selected wavelength was below the detection limit.

In Fig. 2.31 the intensities of the Doppler-shifted HeI beam emission peak (solid dots) and the corresponding unshifted passive emission (open symbols) are plotted for the pulses # 49029 .. 48. For wavelengths where no beam emission signal could be identified the respective symbol is placed on the abscissa. The data are taken from the viewing line with the radial position R_{maj} = 3.8 m for all wavelengths, because both singlet and triplet line profiles are close to the maximum at this radial position.

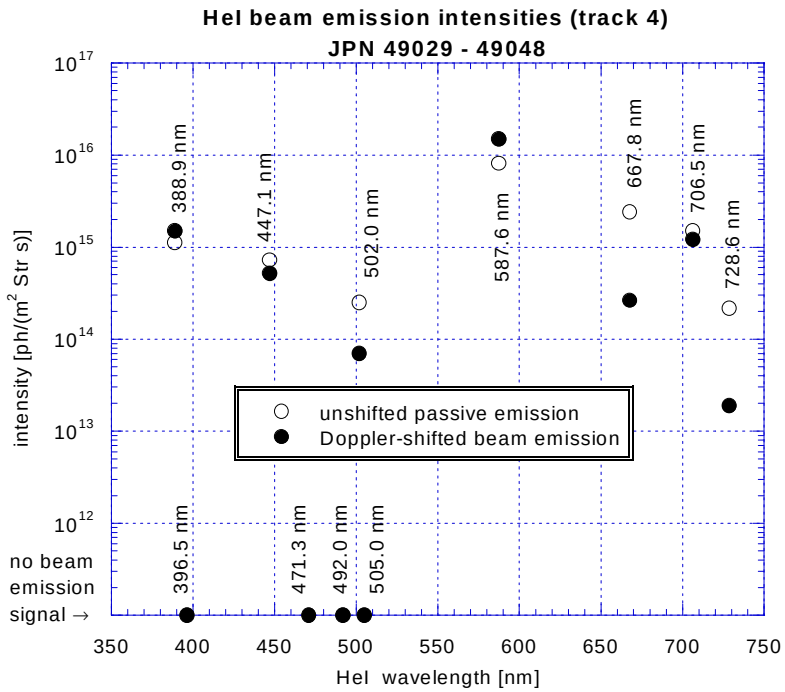

Fig. 2.31: Intensity of the Doppler-shifted HeI beam emission peaks (solid dots) and the corresponding unshifted passive emission (open symbols). Wavelengths where no beam emission signal could be identified are indicated on the abscissa.

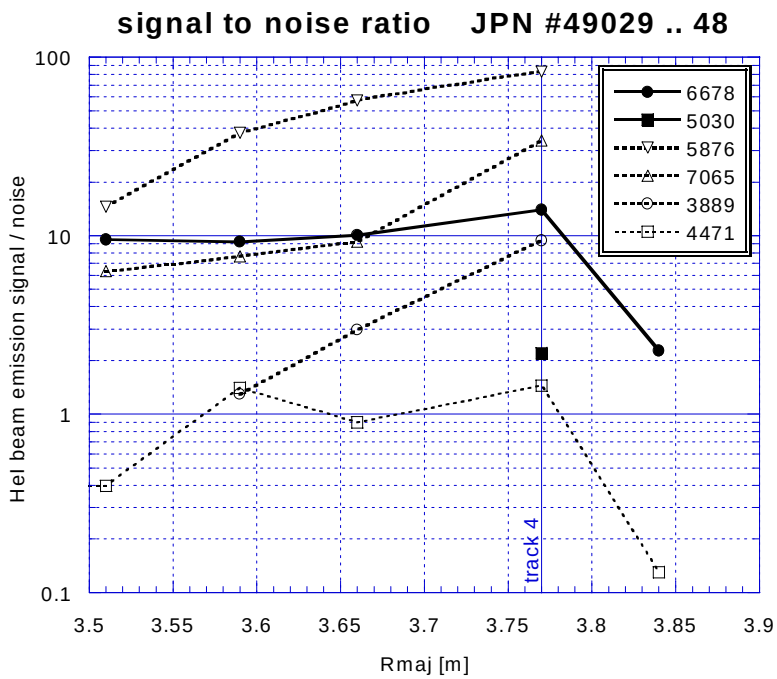

Fig. 2.32: Signal-to-noise ratio (SNR) of the 6 most intensive HeI lines. The low SNR of the 388.9 nm and 447.1 nm lines compared to their relative high absolute signal intensities is due to the low sensitivity of the spectroscopic system at this wavelength. The lines are for guidance only.

In Fig. 2.32 the signal to noise ratio (SNR) of the Doppler-shifted HeI beam emission signals are plotted for the 6 most intensive HeI lines.

The sensitivity of the KS7 system dropped sharply at 500 nm. This can be seen in Fig 2.33, where the quantum efficiency of the KS7 CCD sensor and the transmission of the optical system are plotted vs. the wavelength-range of interest. This drop explains why the two lines with the lowest wavelengths (388.9 and 447.1 nm) show a high intensity in Fig. 2.31 but a low signal to noise ratio in Fig. 2.32. The transmission of the optical system, including the optical head, 5 m Superguide fibre, and 70 m QSF-600 fibre, was calculated from manufacturers data [34].

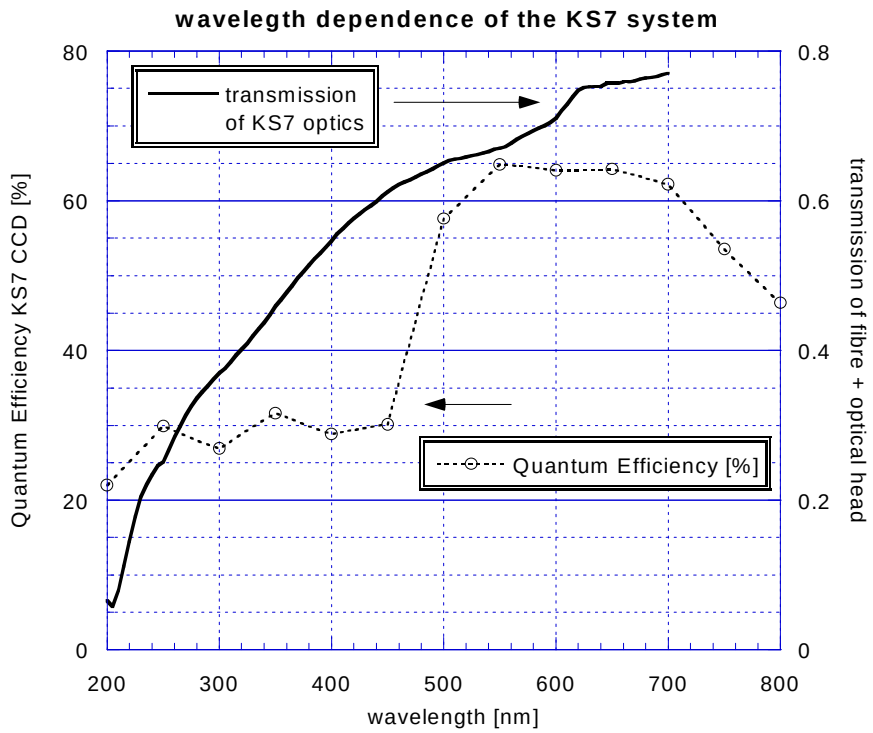

Fig. 2.33: Measured quantum efficiency of the KS7 CCD sensor and calculated transmission of the optical system.

Influence of the He doping on the global Z_{eff} of the plasma

These first measurements using a He doped beam with 500 ms of He puffing into the beam source showed that the pressure in the beam duct stayed well below the limiting pressure, and that the reliability of the doped PINI 6 was unaffected by the addition of helium.

The doped He/D beam produced an increase of the passive HeI line emission from the plasma edge (Fig. 2.34). The red peak is the Doppler-shifted beam emission which appears during the He-doping. The passive emission shows a sharp rise during the He-doping to twice the value and a slow decay over a number of seconds after the end of the He injection. This is due to the influx of He-gas from the beam box. The passive HeI emission is only emitted from the cold outer part of the plasma edge and gives therefore no information about the core plasma.

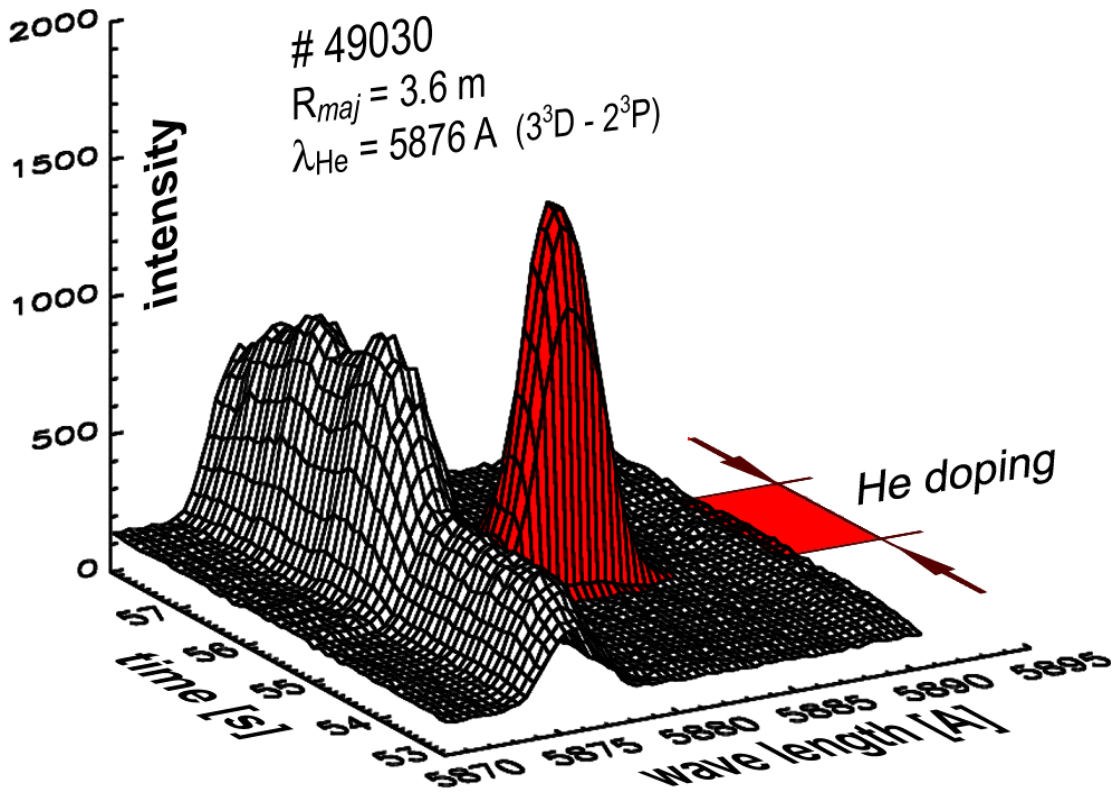

Fig. 2.34: Time development of a HeI spectrum recorded for one viewing-line. The appearance of the Doppler-shifted beam emission peak (red) indicates the time of He doping. At the same time the unshifted peak from the passive edge emission increases.

In Fig. 2.35 the time trace of the global Z_{eff} measurement is plotted together with the injected power of the doped He/D-PINI. The time of the He doping can be identified by the increase of the injected power, when He is being fed into the ion source between 55 and 55.5 s. The subsequent decay of the helium partial pressure in the beam source manifests itself by the decay in the beam current. No increase of Z_{eff} can be seen during or after the He injection.

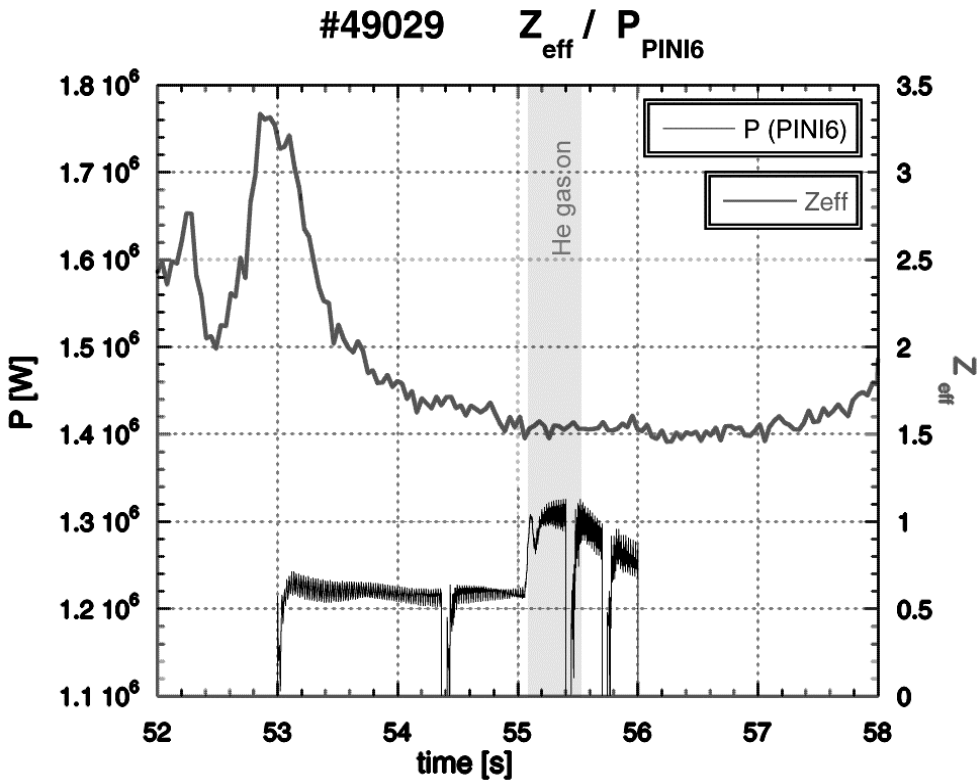

Fig. 2.35: Time trace of the mean Z_{eff}, together with the injected beam power from the He doped PINI. During and after the He injection no increase in Z_{eff} can be seen.

HeI beam emission profile measurements using 16-fibre setup

After this first successful test of the HeI doping system on JET and the assessment of the different HeI line intensities, emission profiles for the three most intensive lines have been measured. In order to obtain a better spatial coverage for these measurements, KS7 was used in its standard setup with 16 fibres. Tab IX shows a list of these pulses with doped He beam injection ("parasitic" beam emission measurements).

JET pulse	Info	HeI transition	wavelength [nm]	P_{NBI} [MW]	P_{RF} [MW]	$<n_e \cdot dl>$ [10^{19} 1/m²]
49225		2^3P-3^3D	587.6	3.2	-	18.6
49226		2^1P-3^1D	667.8	3.2	-	29
49227		2^3P-3^3S	706.5	3.2	-	24
49503	H-mode	2^3P-3^3D	587.6	15	1.2	7.3
49504	H-mode	2^1P-3^1D	667.8	14.7	0.97	10
49555	modulation	2^3P-3^3D	587.6	12.1	1.0	8.9

Tab. IX: Pulses with KS7 in standard setup (1.-19. 11. 1999)

The analysis of this data shows that the reduced bandwidth of KS7 in its standard 16 fibre setup severely limits the quality of the measurement, as further detailed below.

Limitations of the KS7 spectrometer in "standard"-mode

1) Non-uniform magnification

A detailed description of the KS7 spectrometer is given in chapter 2.2.2 and [33,34]. It basically consists of two Czerny-Turner spectrometers in series with a 4x4-array of entrance slits. The first spectrometer acts as a band-bass filter, the second one as the spectral analyser. The purpose of the "band-pass" spectrometer is to mask the spectra, allowing to fit four of then side-by-side onto one row of the CCD-sensor and to prevent cross-talk from adjacent spectra. The CCD is partitioned into 4 tracks corresponding to the 4 rows of entrance slits. The four spectra from each track are extracted during the data analysis and the respective wavelengths are assigned. The transmission function for each entrance slit of the 4x4-array is determined by measuring the signal produced by a white light source. Fig. 2.36 shows the transmission measurement for entrance-slit 2 (of 4) from the first row over the whole width of the CCD sensor (all 385 pixel). The pixel position on the CCD sensor corresponds to a certain wavelength.

One can see that the flat-top region of the transmission function is typically 25 pixel wide, which corresponds to a wavelength range of about 1 nm. Without the "band-pass"-spectrometer the intensity would be constant over the whole sensor width.

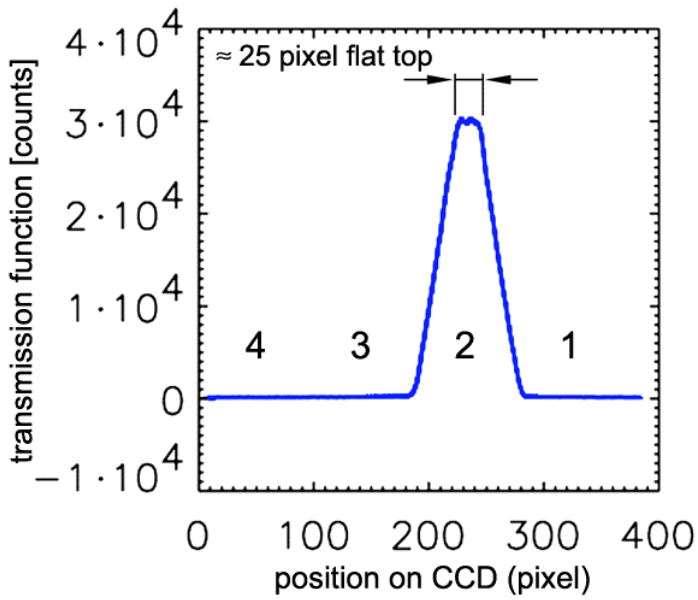

Fig. 2.36: The transmission-function of one slit (second of the first row). The numbers 1 ... 4 indicate the position of all four transmission function of the first row of the slit-array.

Due to the anamorphic magnification of the Cerny-Turner spectrometer the image of the entrance slit-array on the CCD sensor is distorted. In order to get an undistorted image, the entrance slits are shaped to compensate the non-uniform magnification. This shape has been calculated for the design wavelength (λ = 529.1 nm) by ray tracing through two spectrometers.

For wavelengths different from the design wavelength the centre of the transmission function and the position of the centre wavelength are shifted against each other. The direction and amount of the shift depends on the position on the CCD sensor. The shift is more pronounced for slits further away from the optical axis. This can be seen in Fig 2.37, where all spectra (solid lines) and transmission functions (dotted line) of the 4x4 spectra are plotted for a measurement with the central wavelength of 706.5 nm. The positions of the central wavelength are indicated by the black arrows and the positions of the centre of the transmission function is at the centre of each plot (pixel 50).

A problem arises if a spectral line of interest is situated in the wings of the transmission function. For a spectrum near the edge of the CCD-Image and a wavelength setting sufficiently far away (> ±60 nm) from the design wavelength, the central wavelength is already situated in the wing of the transmission function, while the central wavelength of a spectrum in the middle of the sensor is still at the right location. In these cases it is not possible to find a spectrometer setting suitable for all entrance slits. The situation is even worse for the Doppler-shifted line of the beam emission. E.g. the grey shaded peak in Fig. 2.37 is situated in a position at the wing where the transmission is less then half the flat-top value.

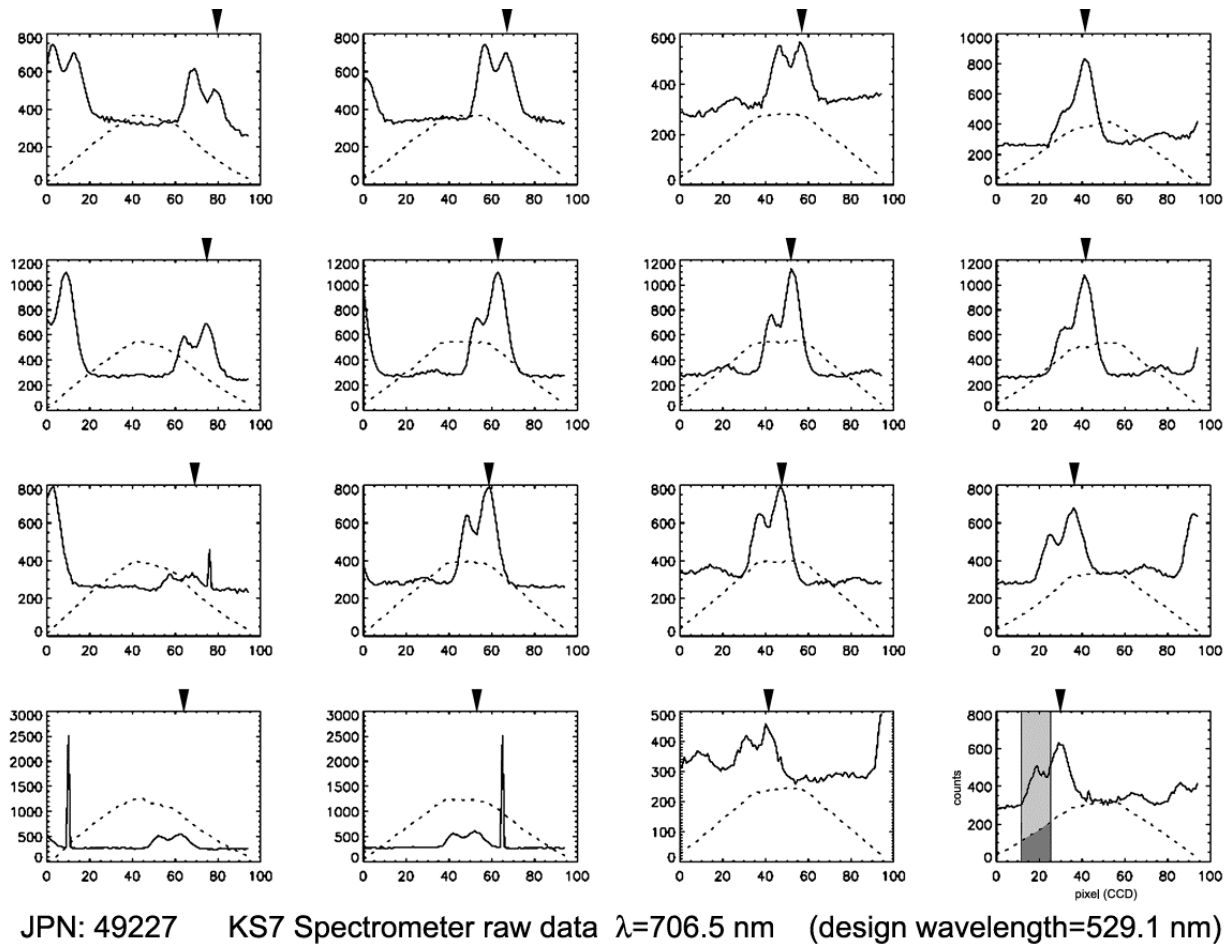

Fig 2.37: The 4x4 spectra (solid lines) and respective transmission functions (dotted lines). The centre wavelength is 706.5 nm. The position of the unshifted peak (equal to the centre wavelength) varies with the position on the CCD sensor (black arrow).

The signal intensities can be corrected for most of the slits by dividing the measured spectrum intensity by the normalised transmission function. However, the noise in the range of the wing is increased significantly, leading to a big scatter for the derived beam emission profile. For wavelength far from the design-wavelength (> ±60 nm) the introduced error thus becomes intolerable large.

2) Problem for the absolute calibration due to different sets of chord-fiber-slits

The optical system of the KS7 diagnostic can be divided into the optical head mounted in the port of the torus, the fibres leading from there to the diagnostics room, and the spectrometer (incl. fibres from the fibre panel to the entrance slits).

The configuration of chords (viewing lines), fibres and entrance slits can be changed on the fibre panel. This makes the system flexible but introduces problems with its calibration. For the absolute calibration the transmission of the whole system (for 5291Å) has been measured for a limited number of chord-fibre-slit configurations.

Subsequently, the total transmission of the system has been divided into the transmission of chord, fibres and entrance slit by a least-squares-fit using the measured set of calibrated configurations. Because this division is not exact, errors are likely to be introduced for other configurations then the ones used for the calibrated systems. This was the case for the He beam emission measurements. A clear deviation was observed for two lines-of-sight. The corresponding beam emission signal was too low for all measured wavelengths. This can be seen in the triplet emission profile of Fig. 2.38, where the two tracks at the radial position R_{maj} = *3.78 m* and *3.82 m* appear as clearly too low.

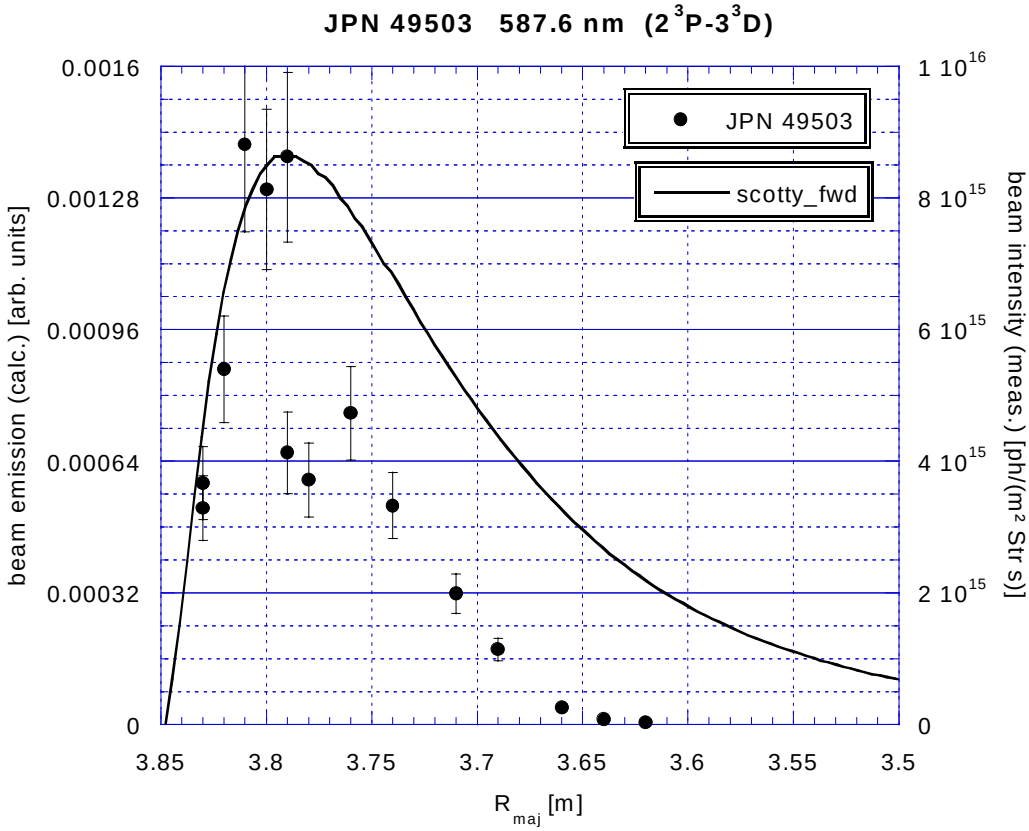

Fig. 2.38: Beam emission profile of the 587.6 nm He I line (2^3P-3^3D) measured during the pulse JPN 49503. The intensities of the two tracks at the radial position R_{maj} = 3.81 m and 3.82 m are too low, indicating an incorrect calibration.

3) cross-calibration of new upper chords

In order to get signals from further inside the plasma and to bridge the Doppler-shift gap of the lower chords, also fibres from the new upper chords have been used. In Fig 2.30 one can see, that position with R_{maj} < 3.58 m cannot be accessed with the lower chords. The optical head for the upper fan of chords had just been installed during the shutdown prior to the operating campaign and no absolute intensity calibration was available at the time of the measurement.

Several attempts to cross-calibrate these fibres against the old lower chords were either unsuccessful or of low quality.

- It was also attempted to use the Bremsstrahlung background for a cross calibration. This failed as well since the Bremsstrahlung signal for viewing-lines close to the plasma edge (most of the KS7 viewing-lines) is too weak.
- The signals of the 667.8 nm HeI emission generated by a short D beam-pulse into He-gas were extremely weak (SNR about unity). Possible differences in the beam alignment with and without magnetic fields added additional uncertainties and this attempt had also to be discarded.
- A comparison of carbon concentration profiles derived from CX-measurements by KS4/5 and KS7 was not successful either. This was due to the large error in the measurement of the C-profile, the different beam energies (75 and 135 keV) used for the two systems, and different wavelengths used for this calibration attempt and the HeI beam emission.

<u>“time-trace” procedure / modulated beam (JPN 49555)</u>

Since the Doppler-shift of the HeI beam emission observed by the KS7 system is small, for most lines-of-sight the beam emission peak was overlapping with the passive HeI emission peak. For these tracks either the fit-procedure failed or the uncertainties of the fit-results were large. The data was therefore additionally analysed with a different procedure.

A so-called “time-trace” procedure integrates the spectrum over the spectral range of the Doppler-shifted peak and analyses its variation with time. In this procedure it is important to apply the correct time dependent background subtraction. An interpolation between the spectrum recorded just before and the one just after the He doping could be used for the background subtraction, because the He doping was relatively short (500 ms) and took place during the flat-top phase of the plasma discharge. However, a linear interpolation over time is only meaningful as long as the unshifted peak is outside the integration range. As seen in Fig 2.34 the intensity of the unshifted peak increases rapidly at the beginning of the He injection and shows only a slow decay after the He injection. Assuming that the increase of the passive He emission is caused by the He-gas influx from the neutral injection box (NIB) the time dependence of the unshifted background emission can be modelled using a constant flow rate while the valve admitting the helium into the beam source is open, and an exponential decay in the helium flow when the trapped volume discharges into the beam source after valve closure [28]. The background intensity from the last frame before and the first frame after the He doping is being used for normalisation.

By modulating the beam during the He-doping the background (incl. the passive HeI-line) can be monitored and used for a more precise background subtraction. For the pulse JPN 49555 the doped He/D-beam has been modulated with 100 ms beam-on and -off time. The exposure time of the KS7 spectrometer has been set to 50 ms. This guarantees that one entire frame is taken while the beam is either off or on.

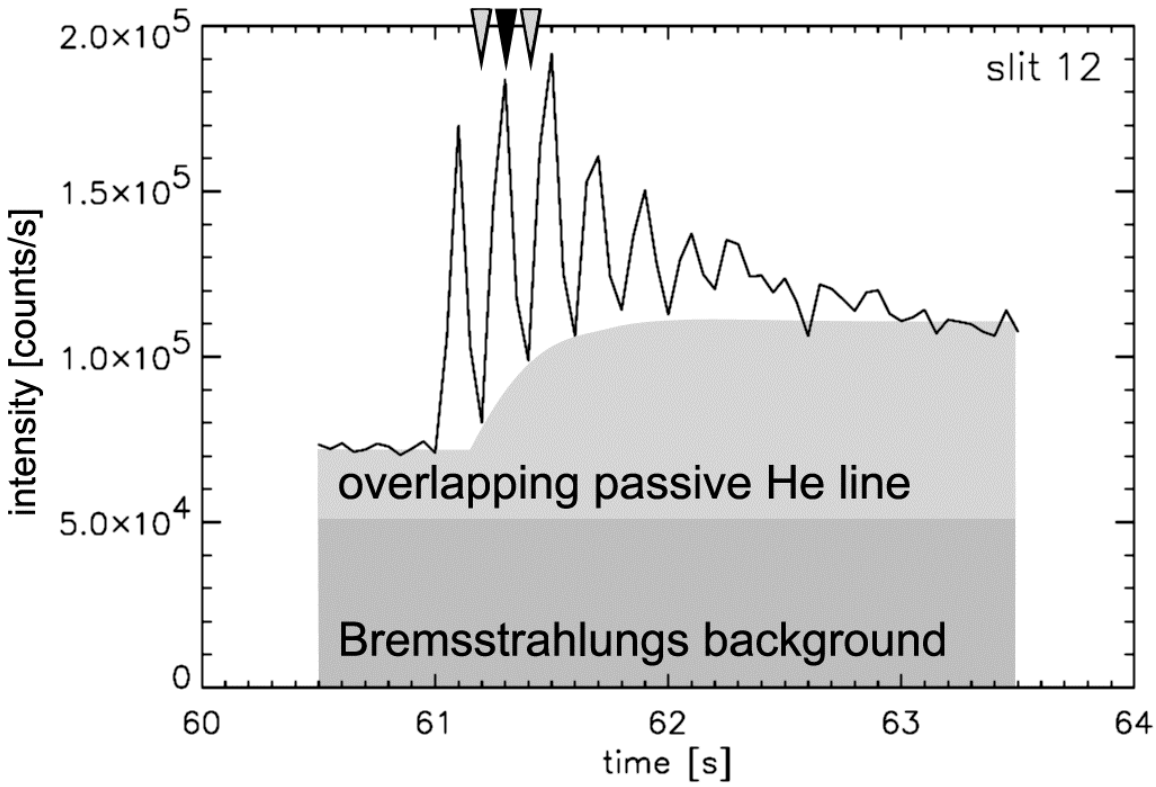

Fig. 2.39: Time trace of the HeI beam emission integrated over the wavelength-range of the Doppler-shifted peak for the pulse JPN 49555. Besides the beam emission the integrated value includes the continuous Bremsstrahlung background (dark grey) and the fraction of the passive He line (light grey) in the spectral range (schematically). The arrows mark the frames used for the spectra in Fig. 2.40.

Fig 2.39 shows the time-trace of the He beam emission integrated over the wavelength range of the Doppler-shifted peak for viewing line 12. On top of the beam emission the integrated value includes also the continuous Bremsstrahlung background emission (dark grey) and the fraction of the passive He line emission (light grey) within the spectral integration range. The modulation of the beam can be seen in the beam emission part of the integrated signal. Fig 2.40 shows the 16 HeI spectra (587.6 nm / 2^1P-3^3D) measured during the pulse JPN 49555 for the viewing lines used. In each graph the spectrum measured during the beam-on phase at t = 61.3 s, the background spectrum, and the difference between the two (blue) are plotted. The “background” spectrum is the linear interpolation of the spectra measured during the beam-off times at t = 61.2 and 61.4 s.

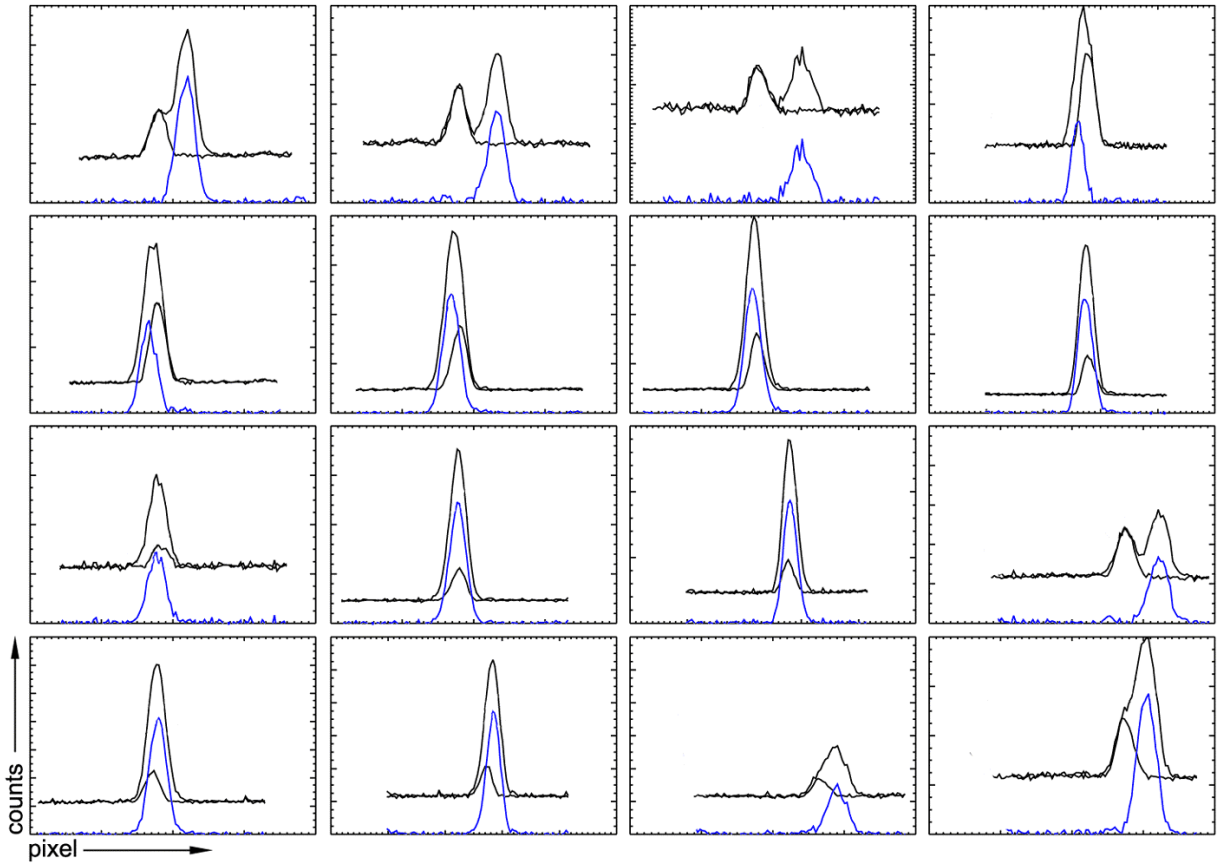

Fig 2.40: The HeI (587.6 nm / 2^1P-3^3D) spectra measured in the pulse JPN 49555 for 16 viewing lines. In each graph the spectrum measured during a beam on phase (t = 61.3 s), the background spectrum (linear interpolation of the spectra from t = 61.2 and 61.4 s), and the difference between the two (blue) are plotted.

The three arrows in Fig 2.39 indicate the timing of the spectra used for the background calculation (grey) and for the beam emission (black). Spectra with well separated beam- and passive emission (e.g., 2nd and 3rd plot in the first row of Fig. 2.40) show that the correct background subtraction is being applied, as the passive emission peak of these spectra disappears completely and only the Doppler-shifted beam emission is left.

By modulating the beam the interference with the unshifted passive HeI line can be eliminated, but at the same time the total beam emission signal is halved. For the measured triplet line (2^1P-3^3D) the signal intensity was nevertheless strong enough in spite of the beam modulation. However, the limited accuracy of the calibration of the individual viewing lines still degraded the quality of the resulting beam emission profiles.

2.5.2 JET December 2000 (sweep experiment with 70keV doped He/D-beam)

For this campaign the pre-set pneumatic timing system of the He doping system has been replaced by a more versatile electronic one. From the experience of the previous measurements in 1999 it was clear that:

1) KS7 can only be used in its 6-fibres setup, and consequently the loss of spatial coverage must be compensated.
2) a cross-calibration of the different channels (viewing lines) is crucial for an improved quality of the measured profiles.

As a full experimental shift of approximately 15 plasma pulses was dedicated to our HeI beam emission experiments, a suitable pulse-type could be chosen. The outcome was the sweep experiment described in chapter 2.3, which met all the above criteria.

The experiments were all performed using the same pulse type, a high clearance diverted L-mode discharge characterised in table II. During the experimental campaign in December 2000, PINI 6 from the neutral beam injector at octant 4, rated for 80 kV, was operated with a doped deuterium helium beam at 70.3 kV. The beam emission was measured with the KS7 spectrometer in its 6-fibre setup. The individual pulses are listed in table X. The column "Gas puff" indicates which gas was puffed into the plasma during the sweep phase. The different gases were used in order to change Z_{eff} of the plasma. The most intensive singlet and triplet HeI beam emission profiles are shown in Fig. 2.41. The data are plotted in the coordinate system used for the model calculations, which is the distance *z* along the beam axis starting from the LCFS.

Pulse	Wavelength [nm]	HeI Transition	Gas puff	line integrated density [$10^{19}m^2$]	Z_{eff}
52796	667.8	$2^1P - 3^1D$	D_2	7.0	1.5
52797	"	"	CD_4	7.5	1.9
52798	587.6	$2^3P - 3^3D$	D_2	7.0	1.7
52799	706.5	$2^3P - 3^3S$	D_2	7.2	1.7
52800	388.9	$2^1S - 4^1P$	"	7.0	1.7
52801	728.1	$2^1P - 3^1S$	"	7.1	1.6
52802	501.5	$2^1S - 3^1P$	"	7.0	1.6
52803	656.1	D_α	"	7.0	1.6
52804	587.6	$2^3P - 3^3D$	CD_4	7.5	1.9
52805	587.6	$2^3P - 3^3D$	CD_4	8.5	2.0

Tab. X: List of plasma and spectrometer parameters used for the sweep experiments in Dec. 2000 at JET.

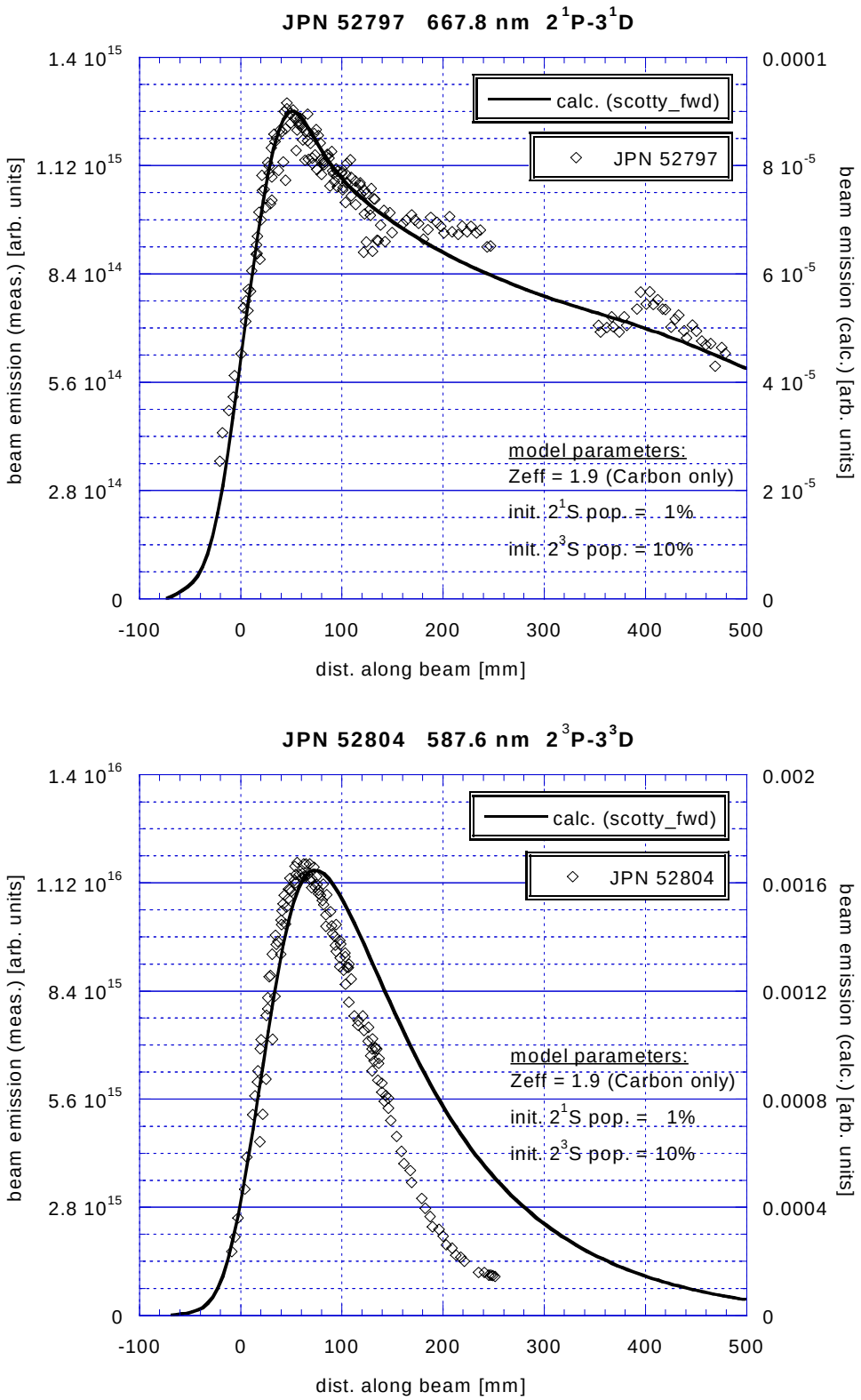

Fig. 2.41: He beam emission profiles from a doped 70.3 keV He beam observed with KS7, compared with model calculations (scotty_fwd). Upper graph: JPN52797, HeI singlet line (2^1P-3^1D) at 667.8 nm Lower graph: JPN52804, HeI triplet line (2^3P-3^3D) at 587.6 nm

For these experiments the fibre viewing the range around $z = 300\ mm$ turned out to be inoperative. As a consequence the fibre viewing the range around $z = 410\ mm$ could not be cross-calibrated (for details on the cross-calibration see chapter 2.3.2).

The triplet emission was quite strong and peaked around $z = 60\ mm$ ($R_{maj} = 3.65\ m$). For z > 300 mm the signal was below the noise level. The singlet emission was by one order of magnitude lower in intensity than the triplet emission, even for the most intensive line, but could nevertheless be detected over the whole range covered by the spectrometer.

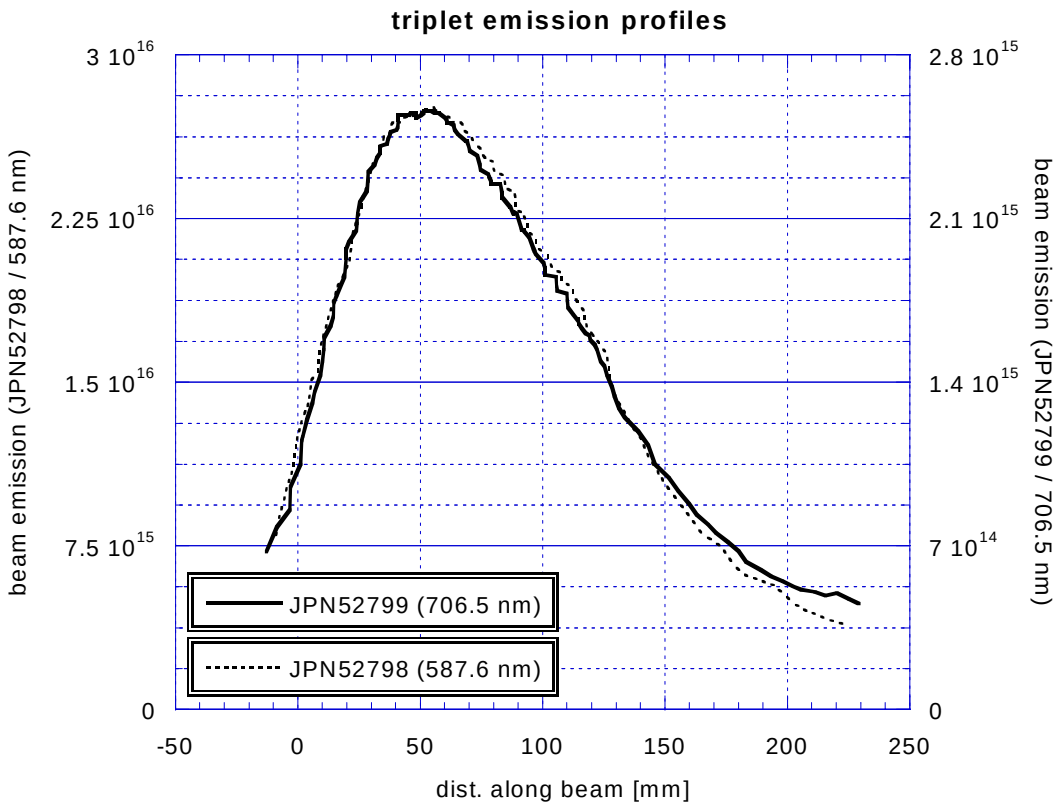

Fig. 2.42: Smoothed HeI beam emission profiles from two different triplet lines measured in successive, basically identical discharges. The shape of the profiles is identical, but the intensity differs by one order of magnitude.

The pulses JPN52798 and JPN52799 were almost identical, with only a small difference in the line average density (7.0 and $7.2 \cdot 10^{19}\ m^{-2}$). The measured He beam emission profiles of the 2^3P-3^3S and the 2^3P-3^3D lines at 587.6 nm and 706.5 nm are basically identical in shape. From this we conclude that no additional information is to be gained from measuring the second triplet line profile. The intensity of the two profiles differs by a factor 10.7 (Fig. 2.42), nevertheless the amount of scatter is the same for both lines, in spite of the large difference in intensities. This indicates, that, at least in this case, the scatter is caused by the plasma turbulence rather than by statistical noise of the sensor.

In the pair of pulses shown in Fig. 2.43 (JPN52798 and JPN52804) one pulse has been performed with a D_2 puff (Z_{eff} = 1.7), the other with a CD_4 puff (Z_{eff} = 1.9). The line-average-density was marginally (7%) higher in the pulse with the CD_4 puff. The beam emission profile from the pulse with CD_4 puff shows a significantly lower intensity (by a factor 2.38) and a slightly reduced penetration compared with the profile from the pulse with D_2 puff. From this we conclude that the metastable triplet population is strongly influenced by the impurity level in the plasma.

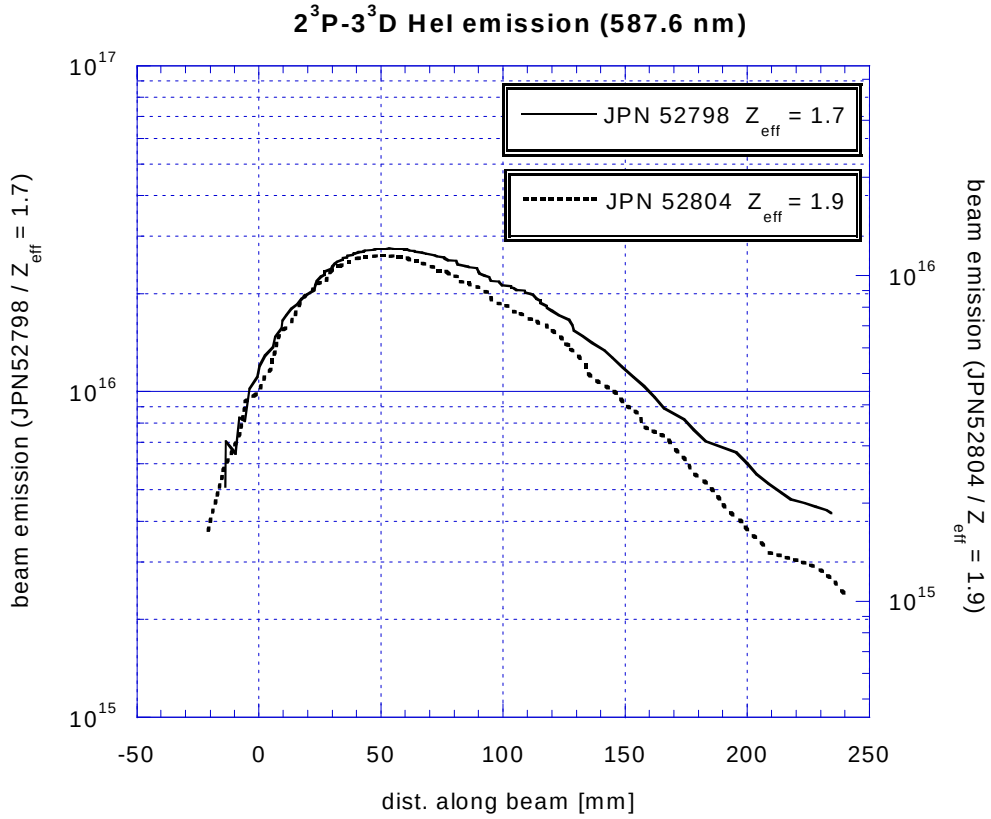

Fig. 2.43: HeI beam emission profiles of the 2^3P-3^3D triplet line (587.6 nm) in plasma discharges with and without CD_4 puff. The CD_4 puff causes a significantly reduced intensity (right scale) and a small reduction in penetration.

2.5.3 JET March 2001 (sweep experiment with 135 keV doped and 73 keV pure He-beam)

During the shutdown preceeding this experimental phase the He doping system has been transferred from octant 4 to the octant 8 injector. Therefore, the doped He-beam was operated from the octant 8 injector, rated for 140 kV. The octant 4 injector had been converted to operate with a pure helium beam. Both spectrometers have been used, KS5 looking at the doped He/D_2 beam from the octant 8 injector and KS7 looking at the pure He beam from the octant 4 injector. The plasma discharges were of the same pulse type as in the Dec. 2000 campaign: a high clearance diverted L-mode discharge, characterised in table II. Compared to the Dec. 2000 campaign, the sweep range was moved in radial direction in order to keep the strike point on the vertical target, which was beneficial for keeping the plasma density constant. The pulse list of this shift is shown in table XI.

pulse JPN	gas puff	line integr. density [10^{19} m^{-2}]	Z_{eff}	KS5a (doped He)		KS7 (pure He)	
				Wavelength [nm]	transition	Wavelength [nm]	transition
53872	CD_4	8.9	2.1	667.8	2^1P-3^1D	501.5	2^1S-3^1P
52873	D_2	11.8	1.7	667.8	2^1P-3^1D	501.5	2^1S-3^1P
53874	CD_4	9.3	2.1	667.8	2^1P-3^1D	447.1	2^3P-4^3D
53875	D_2	10.5	1.7	667.8	2^1P-3^1D	447.1	2^3P-4^3D
53876	D_2	10.0	1.8	656.1	D_α	501.5	2^1S-3^1P
53877	CD_4	10.0	2.1	653.6	D_α	492.2	2^1P-4^1D
53878	CD_4	10.0	2.1	468.6	HeII CX	587.6	2^3P-3^3D
53879	D_2	10.0	1.9	653.6	D_α	587.6	2^3P-3^3D
53880	D_2	10.0	1.9	468.6	HeII CX	501.5	2^1S-3^1P
53881	D_2	10.0	1.9	706.5	2^3P-3^3S	667.8	2^1P-3^1D
53882	D_2	10.0	1.9	587.6	2^3P-3^3D	706.5	2^3P-3^3S

Table XI: Listing of pulses from the shift on 2. March 2001 with 134.5 keV doped He-beam from octant 8 (KS5a) and a pure 72.6 keV He beam from octant 4 (KS7).

The first four pulses where used to set-up the flow rate of the D_2 and CD_4 gas puff in order to get the same plasma density with either puff.

<u>Profiles taken from KS5 (134.5 keV doped He beam)</u>

Two profiles from plasmas with CD_4 puff (JPN53872 and JPN53874) were more peaked than those from plasmas with D_2 puff (JPN53873 and JPN53875). This can be seen in Fig. 2.44, where the first two pulses are overlaid using the same scales for both pulses. Apart from the peak near *z = 100 mm*, both pulses are quite similar in profile shape and intensity, as if the higher density in one pulse would be compensated by the higher Z_{eff} in the other pulse. In the case of 70 keV beam energy, for the triplet profile in Fig 2.2.43 the pulse with the higher impurity level has a

reduced peak intensity, while in Fig 2.44 the 135 keV singlet profile shows a higher peak intensity for the pulse with the higher impurity level.

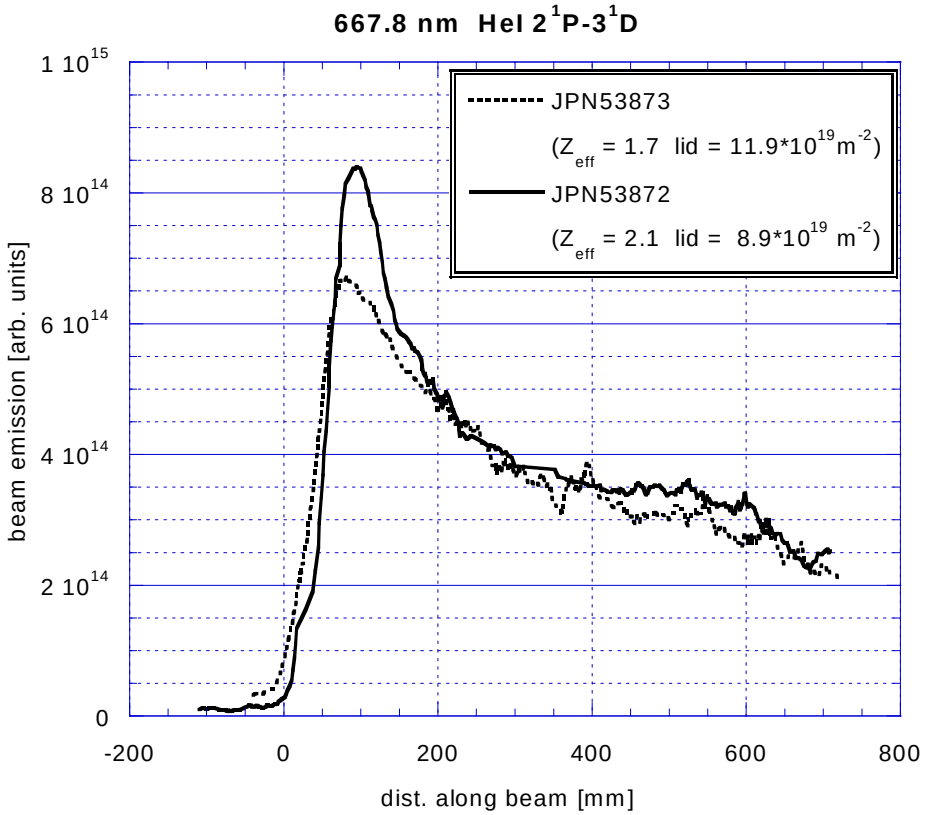

Fig. 2.44: Singlet beam emission profiles of two discharges with and without CD_4 puff. Take not of the significantly narrower peak which forms in the pulse with CD_4 puff.

Two different HeI triplet emission profiles have been measured with KS5a using a 134.5 kV beam. Both profiles, overlaid in Fig. 2.45, have essentially the same shape but differ in intensity. At the radial position *z = 160 mm* we note a deviation between the two profiles, which is limited to one viewing line (# 4). It is likely that this deviation is caused by an impurity line contributing to the measured intensity of the Doppler-shifted beam emission line, which appears at the same spectral location for this particular viewing line. Furthermore, comparing the profile of the 2^3P - 3^3S transition (706.5 nm) measured at 135 keV beam energy with KS5a with that of the same transition measured with KS7 at a beam energy of 73 keV, we also find identical shaped profiles (Fig. 2.46), indicating that their sensitivity to He beam energy is weak. The fact that the same profile is obtained with two independent systems gives additional confidence in our measuring- and evaluation procedures.

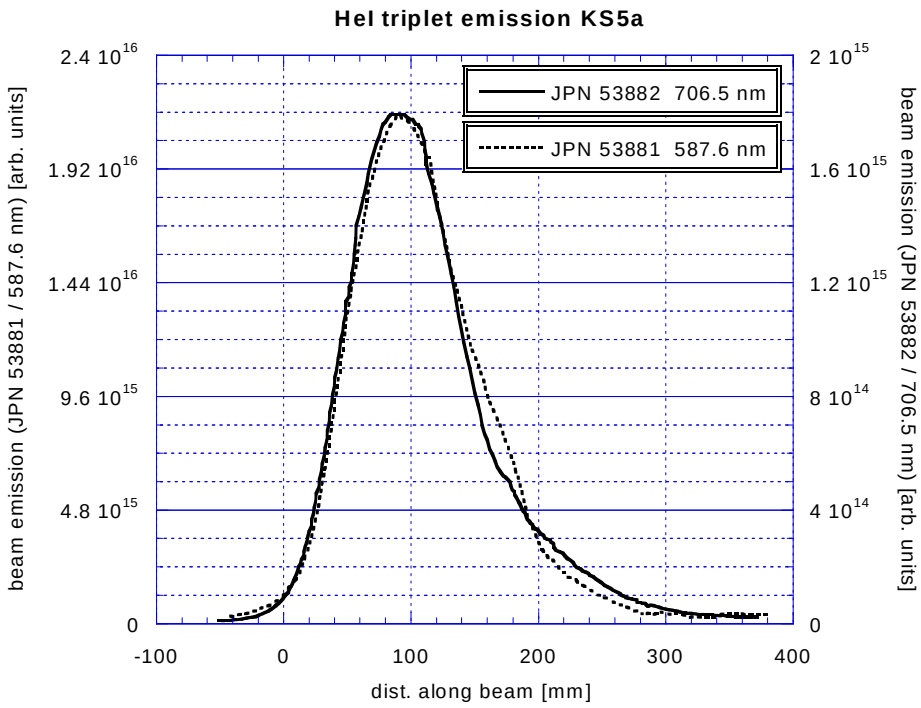

Fig. 2.45: Comparison of the beam emission profile for the 2^3P – 3^3D transition at 587.6 nm (JPN 53881) with the one for the 2^3P – 3^3S transition at 706.6 nm (JPN 53882).

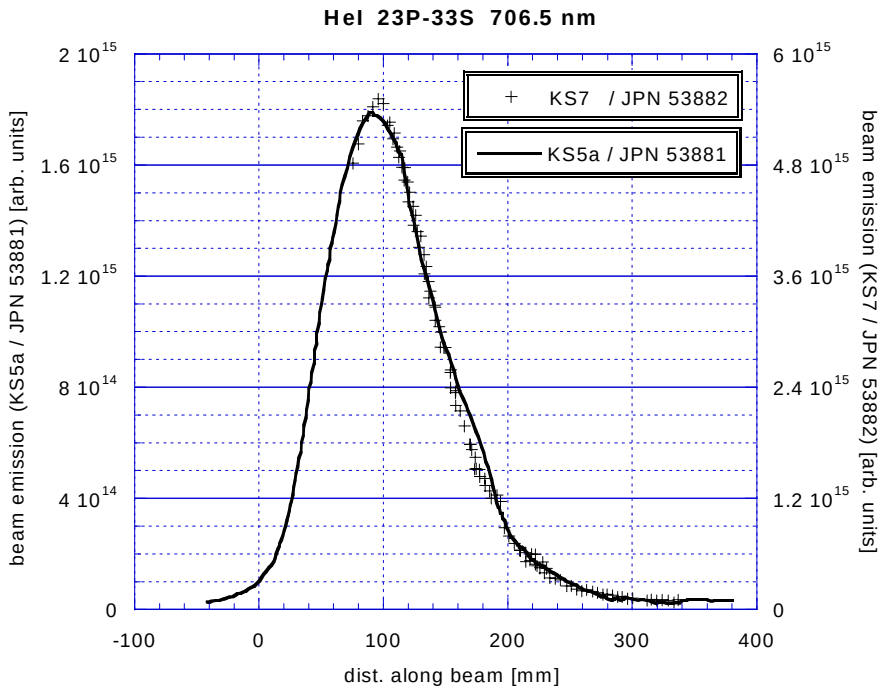

Fig. 2.46: Comparison of HeI 2^3P-3^3S (706.5 nm) beam emission profiles taken from comparable plasma pulses with different He beam energy. KS5a observed a 135 keV doped He beam and KS7 a 73 keV pure He beam.

Profiles obtained with KS7 (72.6 keV pure He beam)

These measurements are different from the above ones in two respects:

1) The pure helium beam is expected to have a lower initial metastable fraction than the doped He/D beam, as the fast He^+ ions are neutralised in pure helium rather than in a deuterium dominated He/D gas mixture for the doped beam (for details see chapter 2.6.2).
2) The helium beam current is higher in the case of the pure helium beam and the beam divergence is likely to be lower. Both effects are leading to a higher He flux density of the pure helium beam.

Fig. 2.47 shows the HeI emission profile from the 2^1S – 3^1P singlet line at 501.5 nm. The transition is sufficiently intense to give a profile as obtained from the smoothed data (9 point average).

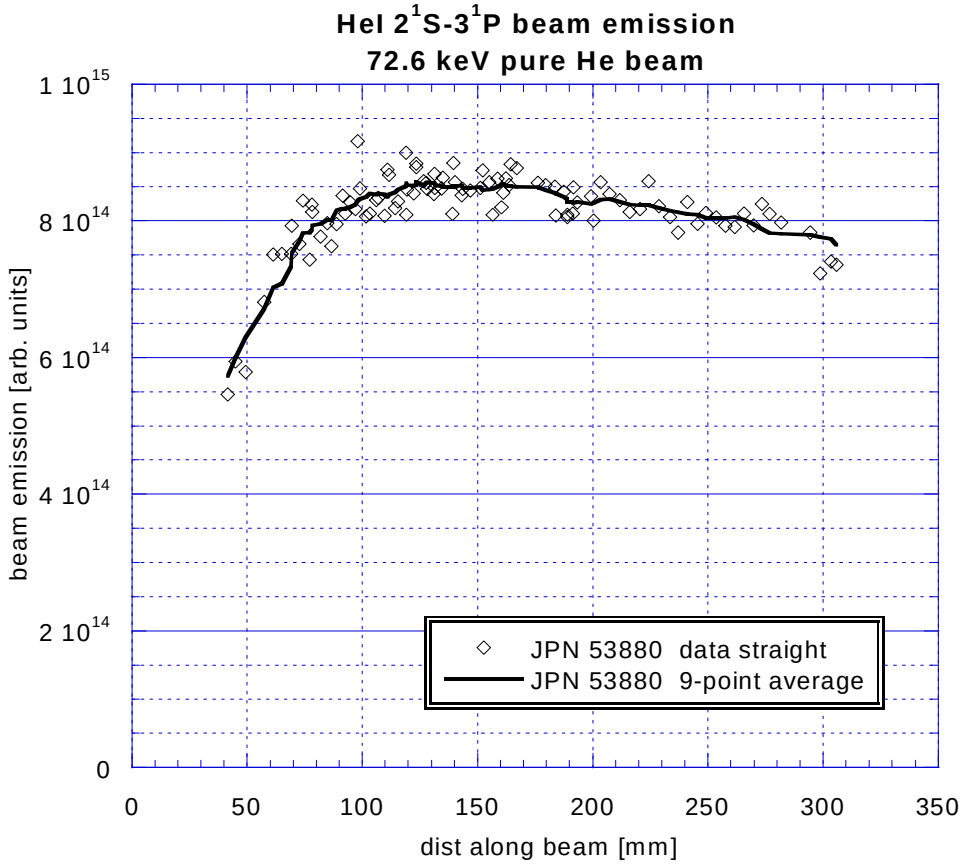

Fig. 2.47: HeI emission profile from the 2^1S – 3^1P singlet line at 501.5 nm.

The singlet profiles from the doped beam show their peak at about *z = 100 mm*, which is characteristic for emission originating from metastable atoms. This peak is not present in singlet profiles from the pure He beam, indicating that the pure He beam has a considerably lower metastable 2^1S fraction than the doped beam, as expected from its neutralisation in He. The small metastable 2^1S fraction is also obvious from the model calculations shown in Fig. 2.48. Here, the measured emission profile is compared with calculations assuming 0 % and 0.5 % of initial 2^1S population. In the profile calculated for 0.5 % metastable fraction a characteristic peak just appears which can not be seen in the measurements, indicating that the initial 2^1S population of the pure He beam is well below 0.5 %.

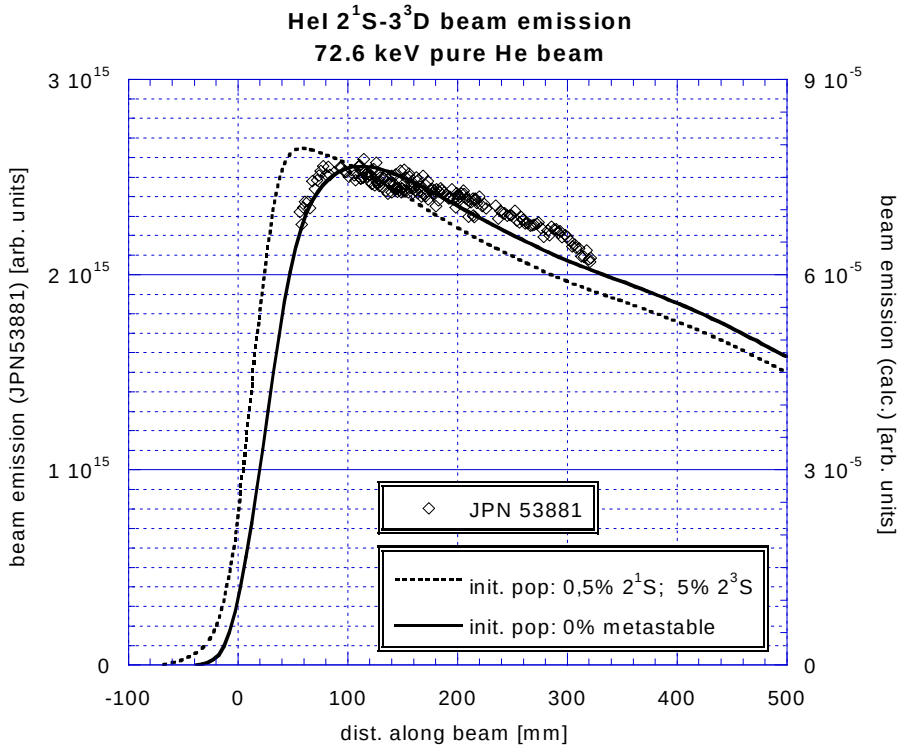

Fig. 2.48: Comparison of the measured 2^1P-3^1D transition (667.8 nm) with model calculations. The two lines are calculations assuming either 0 % (solid line) or 0.5 % (dashed line) initial 2^1S population of the He beam.

Fig 2.49 compares singlet HeI beam emission profiles from the 2^1S-3^1P and 2^1P-3^1D transition measured with a pure He beam. The intensities were normalised to the model calculations. In the outer region up to *z = 150 mm* the profile shapes are noticeably different. This is also reproduced by the model calculations. Further inside the plasma the profiles are similar in shape and the intensity of the most intense singlet line 2^1P-3^1D (667.8 nm) is by a factor of 2.8 higher than for the 2^1S - 3^1P line (501.5 nm).

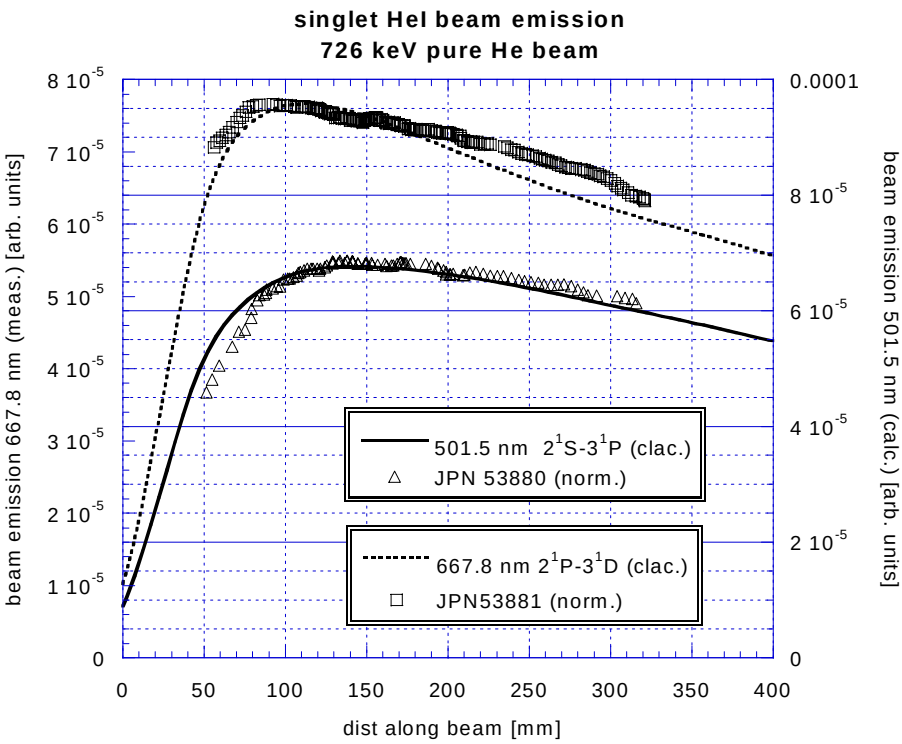

Fig. 2.49: Comparison of the 2^1S - 3^1P singlet line profile at 501.5 nm with the profile from the 2^1P-3^1D transition (667.8 nm). The plasma discharges are comparable, and for both discharges a pure He beam was used.

The triplet HeI beam emission 2^3P-3^3D at 587.6 nm of a pure He beam is plotted on a logarithmic scale in Fig. 2.50. As this was the strongest observed line, the signal-to-noise ratio is excellent in a wide range and the decay can be observed over two decades. From $z = 200$ to $z = 300$ the decay of the triplet line is very well represented by an exponential decay with a decay-length of 39 mm. In that region the density of the plasma is almost constant at $n_e = 4.10^{19}\ 1/m^3$ and the electron temperature increases from 900 to 1200 eV.

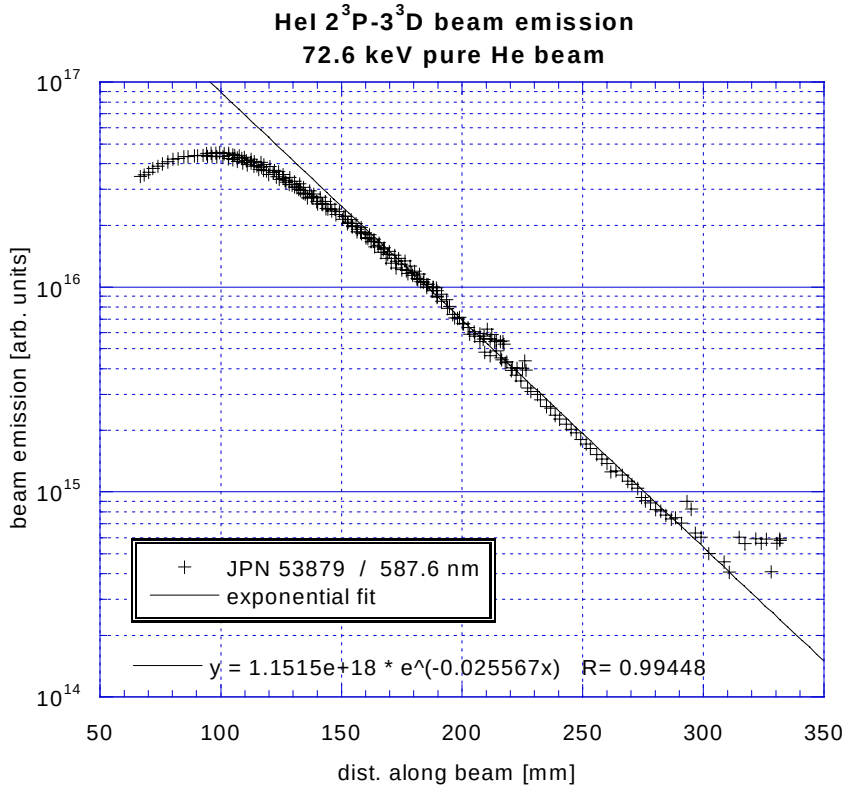

Fig. 2.50: Triplet HeI beam emission 2^3P-3^3D at 587.6 nm for injection of a pure He beam (JPN 53879), plotted on a logarithmic scale. The solid line is an exponential fit to the decay inside the plasma.

2.5.4 Conclusions from the Experiments at JET

As result of the radially swept high clearance L-mode plasma experiments, singlet and triplet profiles could be measured with good spatial resolution. The results were also suitable for the development of a reversion code. The problem from inaccurate calibration of the spectroscopic systems could be overcome by in-situ cross-calibration of neighbouring channels. The HeI beam emission appears in the spectra as s clean Doppler-shifted peak, undisturbed by impurity peaks for most of the wavelength region.

For the doped He beams only one singlet- (2^1P-3^1D) and two triplet lines (2^3P-3^3D and 2^3P-3^3S) could be measured with sufficient SNR. The SNR for lines on both ends of the visible range were low due to a low sensitivity of the detector. Especially, emission at the 388.9 nm line (2^3S-3^3P) is high, but it shows only a weak signal. With the pure He beam more suitable line transitions were accessible and an emission profile for the 501.5 nm line (2^1S-3^1P) could be measured additionally.

The triplet emission line intensity is dominated by the initial fraction of the 2^3S level and its attenuation inside the plasma. The lower intensity of the equilibrium emission could not yet be resolved by the available spectroscopic systems. A significant peak in the singlet profiles measured with a doped He beam indicates an initial metastable 2^1S population of about 1 %, although the metastable population should be predominantly in the 2^3S state [35].

For the most intense lines the noise was dominated by the plasma even for an integration time of only 50 ms, and therefore also the prospect of measuring plasma fluctuations has to be mentioned. This would, however, require a faster detector with higher sensitivity (e.g. photomultiplier tubes with interference filters).

Variation of the impurity content showed that Z_{eff} is of influence on the shape of both the singlet- and the triplet lines. The profiles of the triplet emission becomes narrower with increasing Z_{eff}. The potential of using this sensitivity to impurity levels for developing a Z_{eff}-profile diagnostics should be examined further.

2.6 Discussion of the Results

2.6.1 Estimate of He flux in the doped beam

The two beam emission profiles for pulses JPN 52797 and JPN 53881 were measured with the spectrometer KS7 for plasma pulses with a line-averaged impurity Z_{eff} of 1.9. Pulse 53881 was observed with a pure He beam of 72.6 kV and for pulse 52797 a doped helium beam of 70.3 keV was used. The pure helium beam passed through a plasma with a line-density of 10^{20} /m^2, compared with the line density of 0.75 10^{20}/m^2 for the doped beam. The intensity of the beam emission is a factor of 2.37 higher for the pure beam than for the doped beam. From the known neutral beam current of the pure beam (16 A) we can estimate the neutral He beam current in the doped beam as

$$I_{doped} = I_{pure} \frac{n_{e_{doped}}}{n_{e_{pure}}} \frac{S_{doped}}{S_{pure}} . \qquad (4)$$

S_{doped} ... line emission inensity / doped He beam
S_{pure} ... line emission inensity / pure He beam

With the data above we can derive a doped beam current I_{doped} of

$$I_{doped} = 16 \frac{7.5}{10} \frac{1}{2.37} = 5.06\,\mathrm{A} . \qquad (5)$$

The respective beam emission profiles are shown in Fig. 2.51 together with the modelled beam emission. The profile from the doped beam shows a characteristic peak near the LCFS, which is typical for the emission originated from metastable ions. This peak is not present in the profile from the pure He beam, indicating that the pure He beam has a much lower metastable 2^1S population. This is also reproduced by the modelling where a 1% initial 2^1S population was assumed for the doped beam and no initial metastable 2^1S fraction for the pure beam.

The scale for the model calculations is correct for the pulse with the pure He beam. In order to match the measurement of the doped beam with the corresponding calculated intensity, the latter had to be multiplied with the factor 0.32. This factor is the ratio of the He flux in the pure- and the dopedHe beam and is in agreement with the upper estimation.

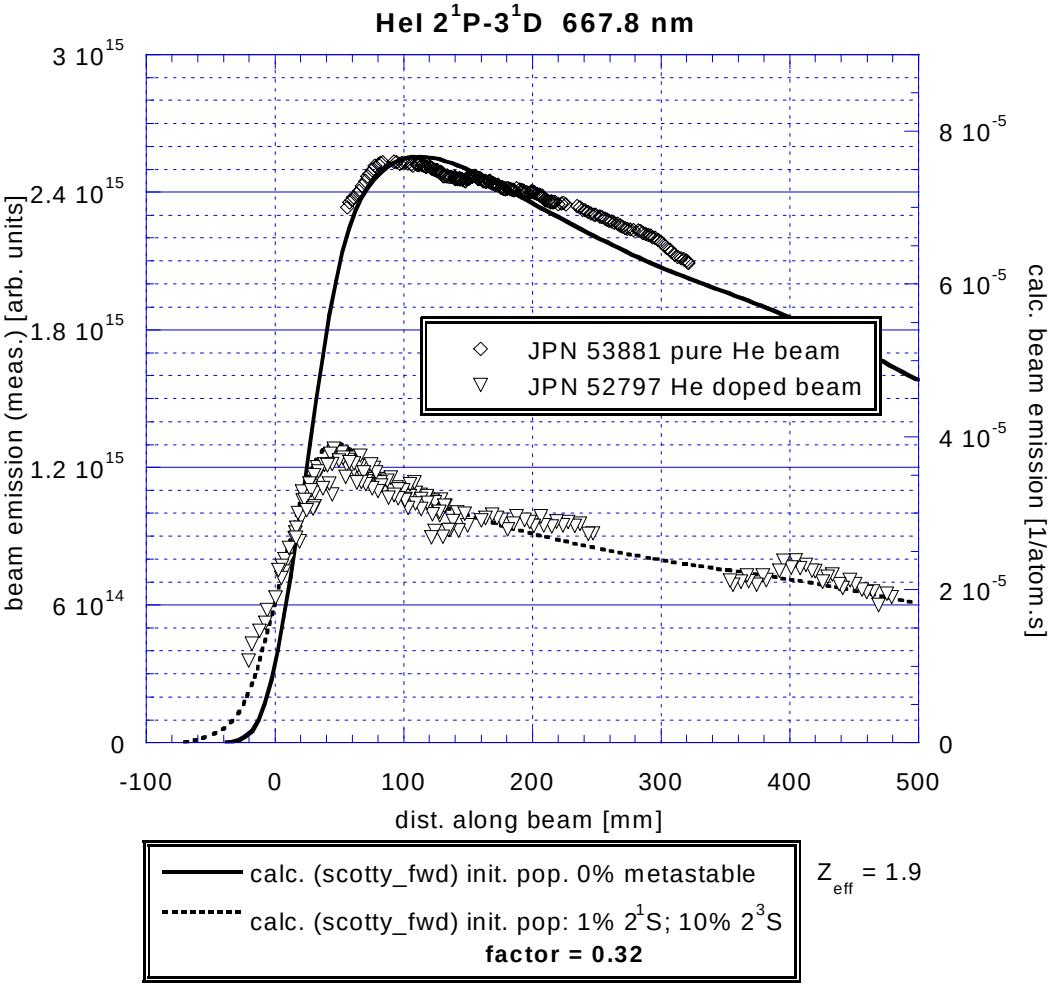

Fig. 2.51: He beam emission of the 2^1P-3^1D transition at 667.8 nm measured with pure and a doped helium beams. The modelled beam emission was calculated for an initial metastable 2^1S population of zero in the case of the pure beam and of 1 % in the case of the doped beam.

2.6.2 Initial metastable fractions in the He beam

The fast He beam consists of atoms produced by charge exchange from accelerated ions. These charge-exchanged atoms are either in the 1^1S ground state or in one of the two metastable states 2^1S and 2^3S. The fraction of metastable atoms depends on the gas used for neutralisation and its target thickness (line-integrated density) in the neutraliser. The neutraliser was operated with He in case of a pure He beam, and predominantly with D_2 in case of a doped He/D beam. The target thickness in the neutraliser of neutral beam heating systems is not well known due to the interaction between the powerful heating beam and the target gas. From the observed degree of neutralisation it could be deduced that the actual target thickness is only in the range of 1/3 to 1/2 of the target thickness in absence of the beam [36, 37].

The total metastable He fraction after neutralisation in a helium or hydrogen gas target and the associated cross-sections have been measured [38, 39]. By stepwise solving differential equations for the destruction and production of ground- and metastable atoms using the cross-sections from the above papers, the population from an initially pure ion beam, which has passed through a neutraliser with given target thickness, can be calculated. Fig 2.52 shows such results for a He target and Fig 2.53 for a hydrogen target, respectively. The range of the probable target thickness of the JET neutraliser is indicated by dotted lines.

From our HeI beam emission measurements only the 2^1S metastable fraction could be estimated. By comparing model calculations with the measured 2^1S-2^3D profiles an initial metastable 2^1S fraction of about 1 % for the doped He beam (D_2 gas target) with energies of 60, 70, and 135 keV, and of less than 0.5% for a 73 keV pure He beam (He gas target) could be determined. This is in agreement with [35], where it is stated that the metastable population is expected to be predominantly in the 2^3S state.

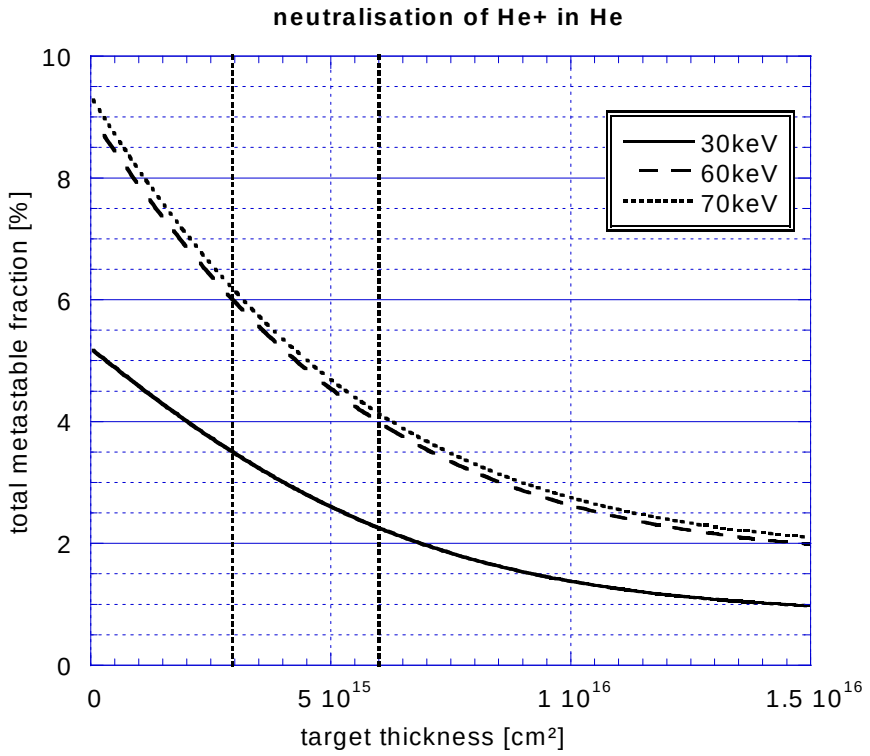

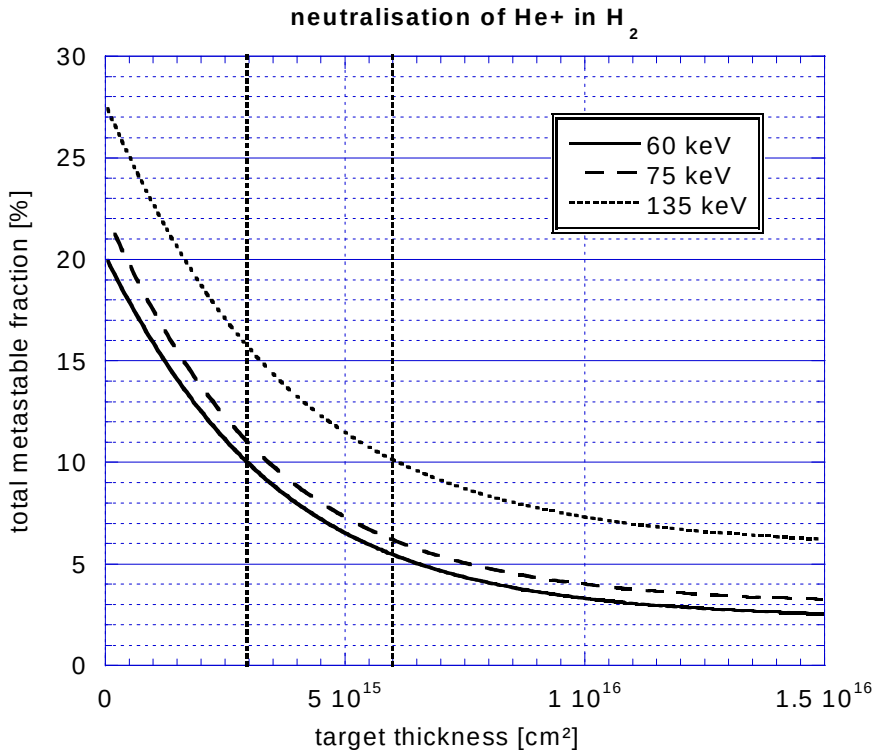

Fig. 2.52+2.53: Total metastable fraction (2^1S + 2^3S) of He beam obtained by neutralisation of He^+ in a gas target for different beam energies. The probable target thickness range of the JET neutraliser is indicated by dotted lines.

Left graph: **He gas target**
Right graph: **H_2 gas target**

2.6.3 Discrepancy with the modelled triplet profiles

For all beam energies the singlet beam emission could be well reproduced by the model calculations (`scotty_fwd`) – see Fig 2.41. For the triplet emission profiles, on the other hand, a significant discrepancy occurred for the width of the peaked profiles at all beam energies. In Fig 2.54 the triplet emission (2^3P-3^3D) at 587.6 nm measured for the pulse JPN 53881 (open symbols) is compared with two different model calculations using the same input-parameters. The solid line shows the result of the `scotty_fwd` calculations, and the dashed curve resuts from the `HEBEAM` code from M. Brix. The intensity of all profiles was normalised to 1.

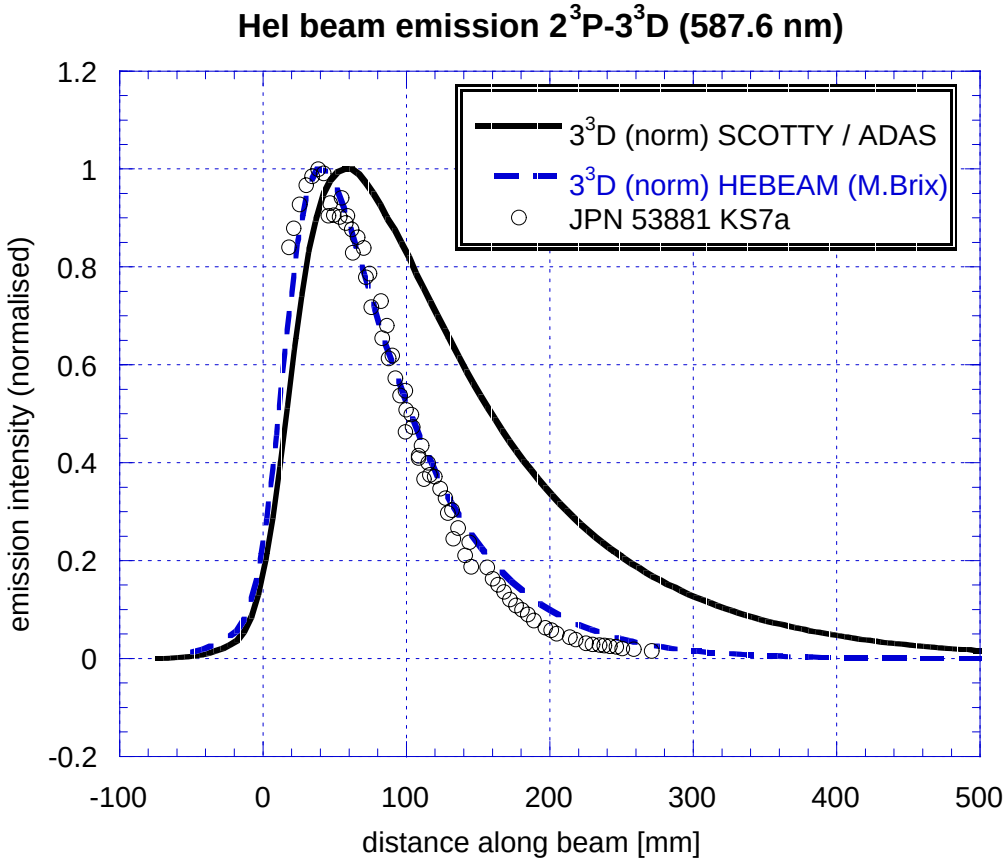

Fig. 2.54: Triplet beam emission (2^3P-3^3D) at 587.6 nm of the pulse JPN 53881. Open symbols are the measurements, the solid curves shows the model calculation with `scotty_fwd`, and the dashed line results from the calculations with `HEBEAM`.

In Fig. 2.55 the modelled populations of the ground-state and the two metastable states are compared from the two codes. A clear difference in the decay of the initial metastable population can be seen. The longer decay lengths in case of the `scotty_fwd` modelling (about twice the values from `HEBEAM`) gives rise to the wider peak-widths. Well inside the plasma ($z > 1000$ *mm*) the initial metastable population has decayed and the equilibrium population reached (flatter part). The decay-length of the equilibrium population are quite similar from the two models.

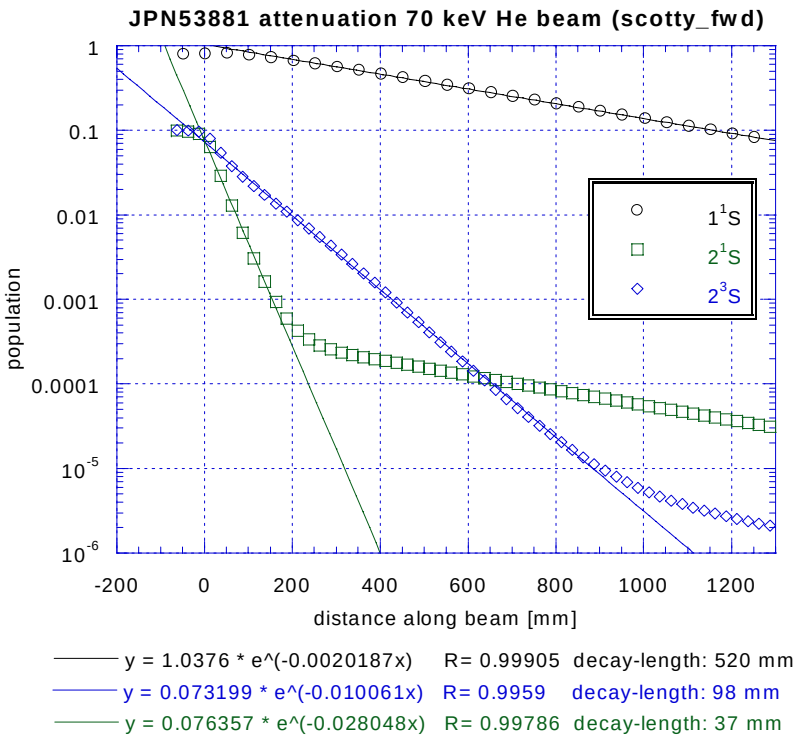

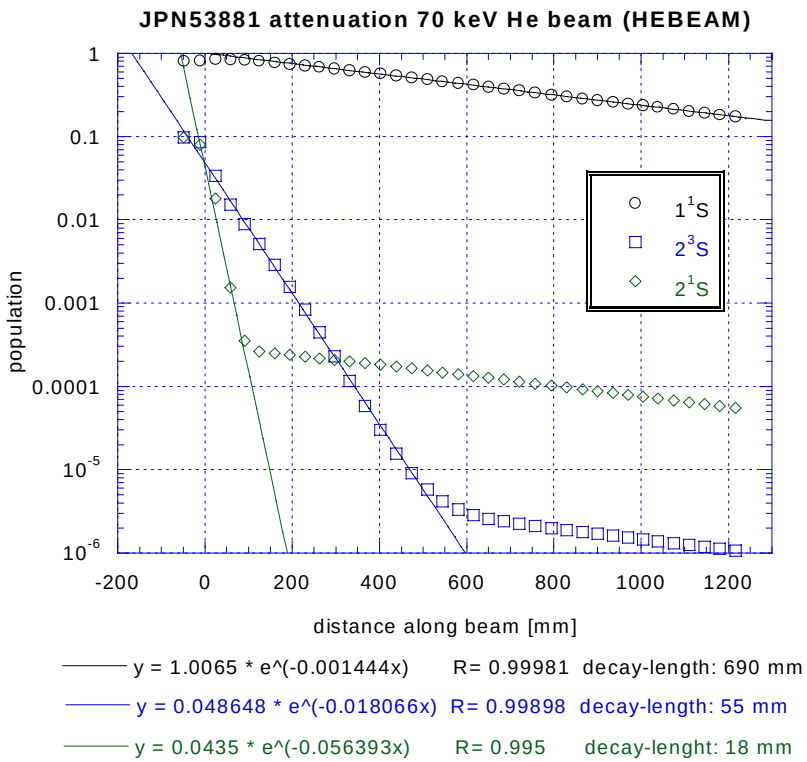

Fig. 2.55: Modelled populations of the ground-state and the two metastable states. The left graph shows results of the `scotty_fwd` modelling and the right graph results from `HEBEAM`. A clear difference in the decay of the initial metastable population can be seen.

One possible reason for the slower decay in the initial metastable fraction could be an error for the calculation of the distance. `Scotty_fwd` uses an

optimisation of its step-width, and an error in the distance calculation could arise from this complex procedure. For testing the code, beam emission profiles for given density- and temperature profiles with periodic squares were calculated (see Fig. 2.56). The resulting populations of the different levels show the expected behaviour. Furthermore, the numerical stability of the code has been tested. Therefore it is likely that the deviation is due to a problem in the atomic data base.

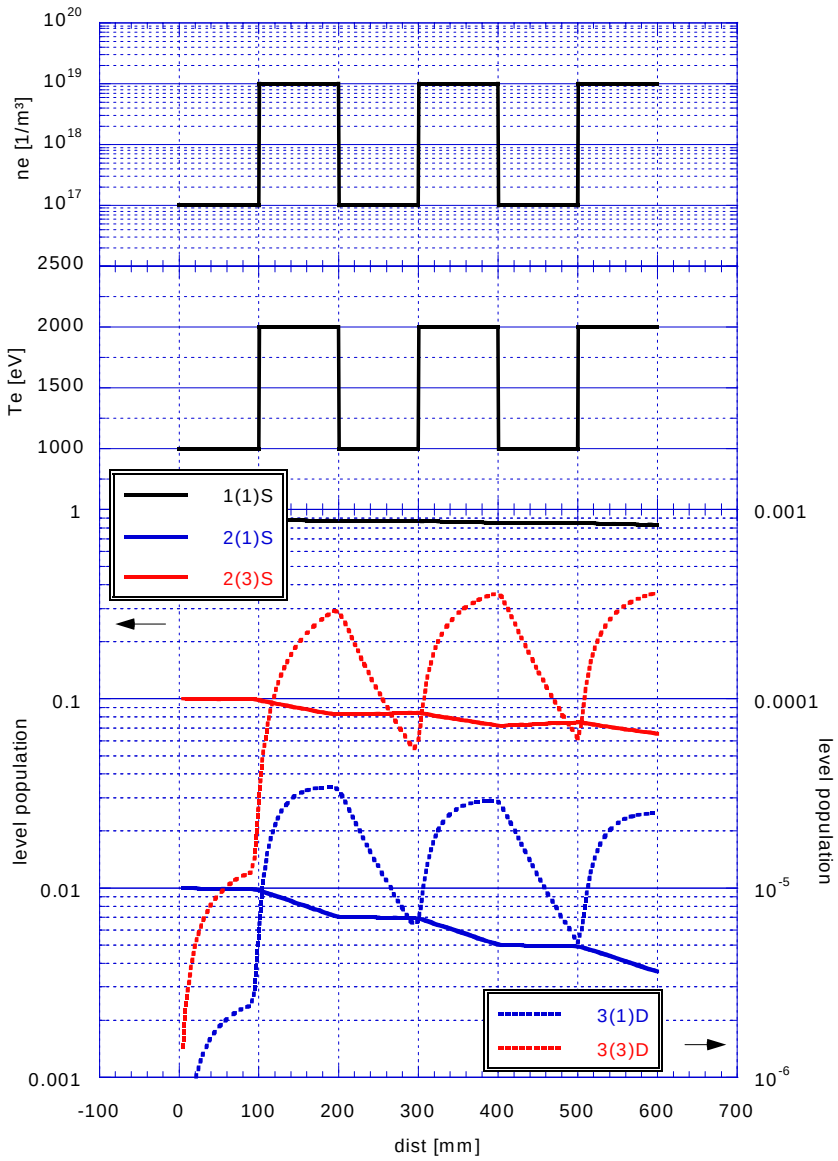

Fig. 2.56: n_e- and T_e-Testprofiles (periodic square profile) and the modelled population of some HeI levels. The resulting emission profiles show the expected spatial correlation, indicating correct calculation of the output distance.

`Scotty_fwd` uses look-up tables generated by a modified ADAS 311 code, whereas the first version of `Scotty` used look-up tables generated by the 311 code of the official ADAS release.

`Scotty_fwd` uses the same atomic data, but the generated data of the look-up tables are represented in a n_e-T_e-plane rather than the n_e-E_b-plane used by the official version of ADAS 311 (n_e = plasma density, T_e = electron temperature, E_b = beam energy).

In a comparison of results from `Scotty` with those from the new `scotty_fwd` it turned out, that the decay-length problem only occurs when using the new look-up tables. It is therefore likely that the n_e-T_e-projections from the ADAS data are responsible for the too wide triplet beam emission profiles.

Due to manpower restrictions on the ADAS side and some incompatibility problems between the ADAS- and the TU Wien computer systems it was not possible to solve these problems in the time frame of this paper. However, to avoid this problem for the development and testing of the reversion code, suitable test-data were generated using the same look-up tables used later for the reversion (see chapter 4.).

3 Analysis of the spectroscopic data

In this chapter the analysis of the HeI beam emission spectra is described. Both at AUG and JET the existing analysis codes where not entirely suitable for our purposes and therefore additional software had to be written.

AUG

At AUG we used the existing IDL code `cer_wid` to analyse the He beam emission data [40]. The code, written for the analysis of charge-exchange (CX) data, is not fully suitable for analysing the He beam emission spectra. The Doppler shift of the beam emission peak is, among other things, defined by the viewing angle and varies with viewing line. Within one profile the values vary over a wide range (more than 1 nm). The Doppler-shifts of the different tracks are so different that the code fails to "find" the Doppler-shifted peak for many tracks. Therefore one has to set the estimated position for the peak of interest (start value for the fit) by hand for every single track. An automatic calculation of the expected Doppler-shift would therefore be very helpful, but has not been implemented yet.

In some cases impurity lines with wavelength and intensity near that of the Doppler-shifted He line are observed. An automatic calculation of the expected Doppler shift would also help to distinguish between Doppler-shifted He beam emission and such disturbing impurity lines.

JET

At JET a complex spectroscopic fitting software called `KS4fit` was developed by M. von Hellermann for the IBM mainframe computer. Due to the complexity of this code it would have been difficult, however possible, to adapt it to our needs. Furthermore, it was clear from the start of our experiments that the then available IBM platform will be phased out. As the new computer platform (LINUX cluster) was already available, we decided to develop our own analysis code there, using IDL[1] for LINUX.

Both at AUG and JET the data acquired during a pulse are stored in big databases and can later be accessed through analysis software. The amount of data was particularly large for the plasma sweep experiments at JET (see chapter 2.3) in which spectroscopic data for many time-frames and channels have been stored. This large amount of data can only be handled by means of automatic access- and evaluation software.

For this purpose the code `he_wid` was developed. In chapters 3.1 to 3.3 the algorithm and the application of this analysis code and its subroutines is being described.

[1] IDL Version 5.3 from RSI research systems INC

3.1 Spectral fit procedure (`hespec_fit / mpfit`)

A typical HeI beam emission spectrum from a single viewing line is shown in Fig 3.1. The intensity of the beam emission corresponds to the area under the Doppler-shifted peak (shaded area). In the algorithm used, a curve-fit of the spectrum is performed and the beam emission intensity is calculated from the resulting fit-parameters (peak width and -height). This procedure ensures that the background and partially overlapping lines, if present (passive emission or impurity lines), are correctly taken into account .

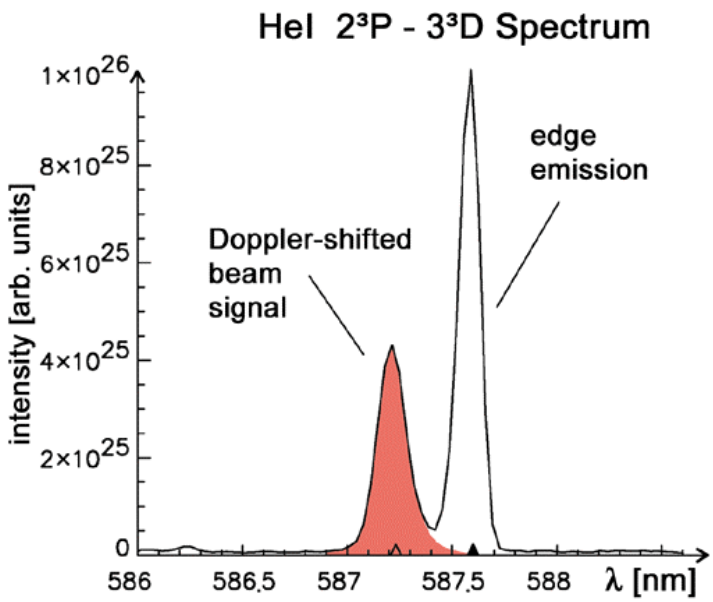

Fig 3.1: HeI beam emission spectrum of the 2^3P-3^3D transition (587.6 nm).

In case of `he_wid` software the curve-fit is performed by a subroutine called `hespec_fit`. The model function *f(x)* for the fit is defined as follows:

$$f(x) = \underbrace{A_0 + A_1 \cdot x + A_2 \cdot x^2 + A_3}_{\substack{\text{background} \\ \text{(polynomial)}}} \cdot \underbrace{\exp\left(-\frac{1}{2}\cdot\left(f_{FWHM}\frac{(x-A_4)}{A_5}\right)^2\right)}_{\substack{\text{Gauss function at } A_4 \\ \text{(unshifted passive emission)}}} + \ldots$$

$$\underbrace{+A_6 \cdot \exp\left(-\frac{1}{2}\cdot\left(f_{FWHM}\frac{x-(A_4+A_8)}{A_7}\right)^2\right)}_{\substack{\text{shifted Gauss function at } A_4+A_8 \\ \text{(Doppler-shifted beam emission)}}} + \ldots + \underbrace{A_{3i+6} \cdot \exp\left(-\frac{1}{2}\cdot\left(f_{FWHM}\frac{(x-A_{3i+8})}{A_{3i+7}}\right)^2\right)}_{\substack{\text{Gauss functions} \\ \text{(impurity lines)}}} \qquad (6)$$

The A_i are the so-called fit-parameters which are adjusted by the fitting procedure to match the data of interest. The background of the spectrum is represented by a polynomial (2. Order – parameters A_0 ... A_2), and each emission line by a single Gaussian distribution function. Impurity lines can be added to the two HeI emission lines – consisting of the passive emission from the plasma-edge and the Doppler-shifted beam emission. Every Gaussian-peak

is defined by its spectral position *(A_4, [A_4+A_8], A_{3i+8})*, its peak height *(A_5, A_7, A_{3i+7})* and its peak width *(A_5, A_7 and A_{3i+7})*.

Using the full width at half maximum (FWHM) for the peak width parameter is convenient, but requires an additional factor (f_{FWHM} in equ. 6). Using the definition of the FWHM and the Gaussian function

$$I(FWHM/2) \equiv \frac{I_0}{2} = I_0 \cdot \exp\left(-\frac{1}{2}\left(f_{FWHM} \cdot \frac{1}{2} \right)^2 \right) \tag{7}$$

the resulting value for f_{FWHM} is given by

$$f_{FWHM} = 2 \cdot \sqrt{-2 \cdot \ln(1/2)} = 2{,}355\,. \tag{8}$$

The subroutine `hespec_fit` itself calls the procedure `mpfitfun`, which is part of the freeware "`mpfit`" by Craig Markwardt [41]. It is based on `Minpack-1` (`Lmdif.f`) by Moré and collaborators and performs a Levenberg-Marquardt least-squares minimisation.

This technique is a particular strategy for iteratively searching for the best fit. This particular implementation is drawn from `MINPACK-1` [42], and appears to be more robust than routines provided by IDL (`curvefit`).

In comparison to the standard curvefit, another advantage is the option of assigning limits to the individual parameters. This turned out to be essential, especially for spectra with impurity lines.

3.2 Mapping of plasma parameters onto beam axis

In a magnetically confined toroidal plasma, so called nested flux surfaces are formed by the magnetic field lines twisting around the magnetic axis. Along these flux surfaces transport is fast and many plasma parameters are therefore kept constant. Consequently, the flux surfaces provide the obvious coordinate system for the plasma. The various diagnostics and their lines of sight are geometrically related to the fixed vacuum vessel and intersect different parts of the plasma. Plasma parameters (e.g. electron density or -temperature), measured by means of the various diagnostics, must therefore be mapped from the origin of the measurement to the system of nested flux surfaces.

Both AUG and JET have implemented an equilibrium code called EFIT which calculates the location and shape of the flux-surfaces from magnetic flux loop measurements, coil currents and the magnetic properties of the major machine parts (e.g. influence of the iron core). For each pulse the flux-surfaces for a certain number of time slices (at JET typically every 200 ms) are calculated and stored in a database.

Both AUG and JET provide code libraries called "`flush routines`" at JET and "`kk-library`" at AUG, respectively for mapping from one coordinate system into another.

For the modelling of the He beam emission it is necessary to know the electron density and -temperature along the beam path. Data taken by the various diagnostics are stored together with the location of the measurement. Either the actual position (e.g. R,ϕ,ψ) or the flux-surface coordinates at this position are given. In some cases the position is mapped to a standard plane (e.g. the mid-plane of the machine) and the respective radial position - major radius (R_{maj}) is given.

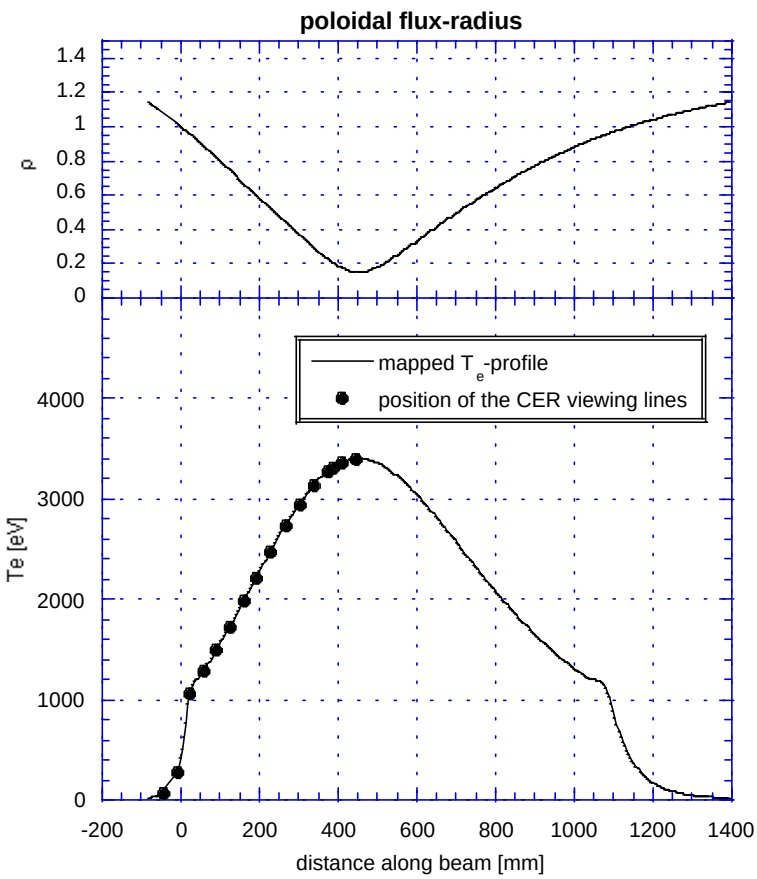

Fig. 3.2: Poloidal flux-radius along the beam (upper graph) and mapped and interpolated electron density along the beam (lower graph).

The poloidal flux radius (ρ_{pol}) is a "natural" coordinate system for flux-surfaces. Rho poloidal, the normalised poloidal flux radius, is defined by:

$$\rho_{pol} = \sqrt{\frac{\Psi - \Psi_a}{\Psi_s - \Psi_a}} \tag{9}$$

Ψ is the poloidal flux, the index s refers to the separatrix location and the index a to the magnetic axis. ρ_{pol} extends from the plasma axis ($\rho_{pol} = 0$ at magnetic axis) to the separatrix ($\rho_{pol} = 1$ at the separatrix) and beyond ($\rho_{pol} > 1$).

<u>AUG mapping code</u>

A small code (`map_beam`) has been written which provides ρ_{pol} for equidistant points along the beam path, by mapping the cylindrical coordinates of the beam trajectory to the flux-surfaces (see upper graph in Fig. 3.2).

From the so-called AUG ddf database plasma density and -temperature profiles can be accessed in poloidal flux-surface coordinates. By interpolating this data for the ρ_{pol} values of the beam trajectory, the density and -temperature profiles along the beam are derived. Fig. 3.2 shows the output of the mapping code (upper graph) and the interpolated plasma density along the beam path (lower graph). The dots mark the intersection of the lines-of-sight of the CER diagnostics with the beam trajectory.

At JET a similar code is being used. The precision of the EFIT reconstruction at JET is limited by some peculiarities:

- JET has an iron core transformer and the saturation of the iron must be incorporated into the code, adding to its complexity. As a consequence the code is not being updated as regularly as in other experiments.
- A considerable number of magnetic sensors have failed.
- The field ripple is only negligible near the magnetic axis, but becomes noticeable near the coils. Reciprocation probe measurements of the plasma edge location show discrepancies of up to 100 mm at the position of the probe, compared to the plasma edge calculated with EFIT.

3.3 Analysis code for the sweep experiments (`he_wid`)

For the analysis of the raw data from experiments at JET a code called `he_wid` has been developed. It is written in IDL and makes use of IDL-widgets (graphical user interfaces). Although specifically designed for the sweep experiments, the code has been kept versatile and is able to deal with data from different spectrometers. However, the code includes a lot of JET specific commands. Nevertheless it should be possible to adapt the software to other raw-data sources (file or AUG) with only minor changes. Especially the curve-fittig routine is independent of the origin of the data.

The code incorporates the following features:

- Access to JET database (JPF / PPF / raw-data)
- Absolute calibration of the spectra (software module `int_calibr`)
- Versatile spectral fit (making use of `mpfit`[2]):
  - Estimation of the Doppler-shift (automatic setting of the start parameters)
  - Option of limiting parameter ranges
  - Additional Gaussian-peaks can be added for disturbing impurity lines
  - Interactive input of the parameters for these additional Gaussian-functions.
- Different display options:
  - Spectra including resulting fits (free choice of tracks)
  - Interactive zooming (= range definition for fit)
  - Time trace of beam data
  - Interactive input of start-, end- and current-time frames
  - Plot of the resulting fitting-parameters (free choice of parameters)
  - Toggle between time-trace and distance along beam (mapping)
- Possibility of background subtraction for modulated beams (interpolated background)
- Automatic identification of frames with NBI-break-downs
- “overlap”-calibration (for sweep experiments)

MAIN WIDGET:

When starting `he_wid`, the main widget appears (see screen shot in Fig 3.3).

[2] see chapter 3.1

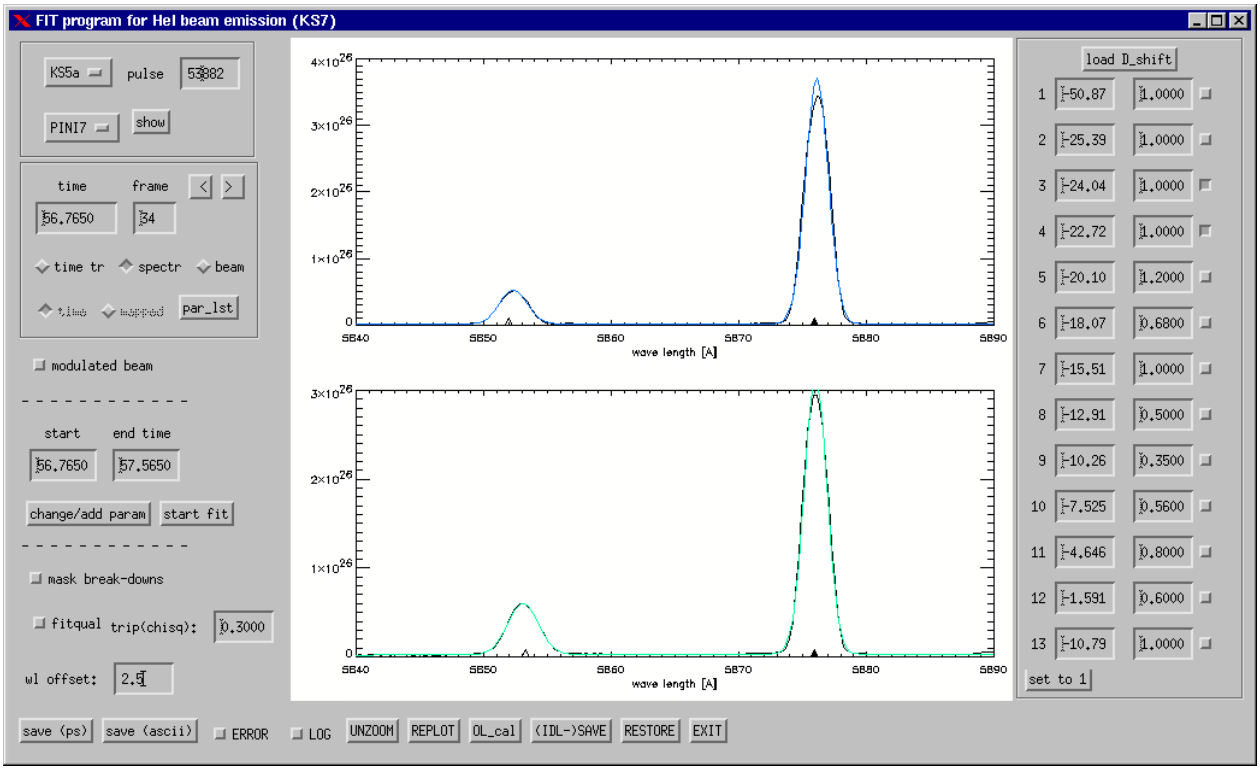

Fig. 3.3: Screen shot of the main widget of the IDL-program `he_wid`

Loading raw data:

The framed region in the upper left corner contains the buttons and fields for loading the raw data. The appropriate spectrometer can be chosen by operating the upper pull-down-list-button. The content of the second pull-down-list (useable beams – PINI numbers) is automatically adjusted to the selected spectrometer.

After selecting the spectrometer, PINI- and pulse-number, the data access can be started by pressing ENTER (“pulse field” needs to be the active field).

The following sequence is started:

- loading and displaying of the time-trace from the ppf-data for plasma position (XLOC/RBO) and beam power of the selected PINI.
- loading raw data of the selected spectrometer (call of `spec_jpfreader` by A.Meigs/JET).
- applying background subtraction from the raw data.
- applying absolute calibration to the data (converts counts into photons/Str*m²*s).
- pre-setting the start- and end-time frames to the times of the extreme positions of the plasma (horizontal sweep).
- displaying the spectra at the start time.

Absolute Calibration: The absolute calibration is carried out by a subroutine called `int_calibr` (more details see chapter 3.4).

Display modes:

The second framed region comprises the buttons and input fields for changing the plot display. There are three display modes available (row of toggle buttons):

1. time trace / mapped radius
2. spectrum
3. beam

During the loading procedure the display is set to the “beam”-mode. Once all data are loaded, the display changes to “spectr”-mode and displays the spectra of the active frame.

1) beam mode

Display of the time traces for beam power and plasma position:

- **beam power**: The nominal injected power of the selected PINI - ppf-data NBIx/NBLy where x is the number of octant of the beam (4 or 8) and y is the number of the PINI used.
- **plasma position**: The outer position of the Plasma boundary (LCFS) at the mid-plane of the machine ppf-data XLOC/RBO
- Start-, end- and active frame are display as vertical lines in the plot

Interactive mouse actions:

- A single mouse-click (left mouse button) within a plot sets the active time and changes the display-mode to “spectrum”
- By clicking within a plot, dragging the cursor to a second position and subsequently releasing the mouse button, the start- and end frame are set.

Start- and end time can also be typed into the respective fields of the main widget. The start- and end times define the time-range displayed in the “time trace”-mode and the frames to which the fit procedure will be applied to.

2) Spectrum mode

The spectra of the selected tracks at the active time/frame are displayed.

Selecting tracks: On the right side of the main widget is a list of fields/buttons. Each row belongs to a track. The fields are for Doppler-shift and relative calibration of each track. The checkbox on the right side of the fields is for activating or de-activating the respective track.

Selecting active time/frame:

- A time can be typed in the “time” field. By pressing ENTER the active frame is set to the closest frame and the respective time and frame-number are displayed.
  In case “spectrum” is the active mode, the respective spectra are plotted.
- Scrolling from frame to frame is possible with the two buttons to the right of the frame field.
- The active frame can be set interactively in the “beam” plot.

Zoom/unzoom:

The spectral range can only be selected interactively. The start- and end value of the wavelength range are set, by clicking within a plot (spectrum), dragging the cursor to a second position (within the same plot) and subsequently releasing the mouse button, .

The spectral range is applied to all tracks. For the input of the fit routine only the displayed part of the spectrum is used. In this way disturbing lines can easily be excluded, provided they are distinguishable from the Doppler-shifted lines.

The software has a zoom-history storing a limited number of zoom ranges. By pressing the "UNZOOM" button the displayed spectral range goes back one step in the zoom-history.

Wavelength offset:

The expected position of the unshifted peak is marked with a solid triangle at the bottom of each spectrum plot. When the Doppler-shift values are loaded, the expected position of the respective peaks are marked by open triangles. Due to inaccuracies in the wavelength calibration the whole spectrum can be slightly shifted. This shift can be incorporated by typing the wavelength shift in the field "wl offset" and acknowledging with ENTER. The estimated peak position must be sufficiently close to the actual peak position for the fit-procedure to succeed.

3) Time trace / mapped radius mode

This mode is for displaying the parameter of the fit and is therefore only available when the fit procedure has been started at least once for the current data.

In this mode another toggle button becomes available which allows to switch between time trace plot display and "mapped" plot.

- **Time trace plot:** The selected parameters are plotted over the selected time range [start-, end time].
- **"mapped" plot:** The parameters are displayed along the beam, taking the plasma movement into account. For the time being the mapping is approximate in the sense that the shape of the flux surfaces is regarded as fixed. This is the case for the slow sweeping experiments. The radial positions of the different active volumes (fixed in space) are supplied by other programs and stored in tables. The relative plasma movement over time is represented in an imaginary movement of the active volumes of the different tracks (the plasma is regarded as fixed in space). The relative movement is given by the relative change of the major radius of the plasma boundary at the mid plane of the machine (XLOC/RBO). The active time is taken, for the time point where the mapped values equals the actual positions of the active volumes.

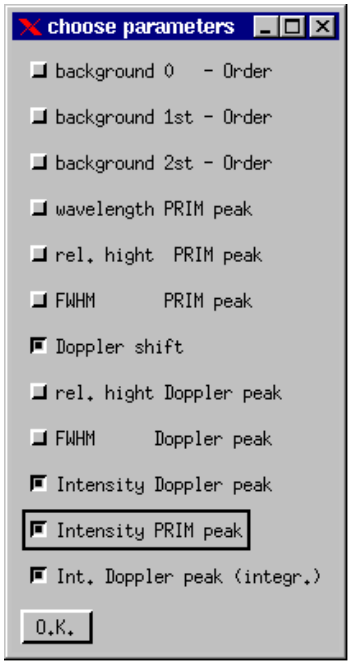

Fig. 3.4: Widget for choosing parameters to display

Choosing parameters:

The selection of the displayed parameter is done via a separate widget which can be called by pressing the "par_lst" button (i.e. parameter list button). Fig 3.4 shows the widget with the list of parameters to choose from. All parameters but the last are fit parameters.

The last one (intensity Doppler-shifted peak – integrated) is given by integration (summation) over the Doppler-shifted peak after background subtraction. For the background subtraction the resulting fit is used leaving out the Doppler-shifted peak. Thus only the peak of interest remains in the spectrum, provided that the fit-procedure was successful.

4) Masking of frames/time points

Breakdowns:

During the operation of the heating beams high voltage breakdowns can occur from time to time. In the case of a breakdown the beam is turned off for typically 30 ms. This affects the intensity of the beam emission and must be taken into account. The software looks for breakdowns in the beam data files and identifies the respective frames.

With the toggle button "mask break-downs" the masking of frames with a breakdown during the exposure can be turned on and off.

Fit qualtity:

The intention of implementing this feature was to make it possible to mask fits with bad quality.

The first attempt was to mask all frames where the chi-square value of the fit exceeds a certain trip level (field right to the toggle button). This option does not appear to be useful, but it is still implemented.

Activating the "fitqual" toggle involves another masking of the data. If at the end of the fit-procedure a parameter "still tends" to overcome its parameter limit, it will be indicated by the fit code. If the "fit quality-masking" is turned on, these frames are masked as well.

5) Error bars

Error-bars are calculated for each frame and track by the fitting procedure. The starting point for the calculation is the statistical error of the detector ($\sqrt{counts / gain}$) for each pixel of the spectrum. Additional calculations of the error are done by the `mpfit`-code (some more information see http://cow.physics.wisc.edu/~craigm/idl/fitting.html). There appear to be some inconsistencies in the error bars coming from `mpfit`. Therefore, the error bars should not be used at the present stage of the software development!

For the integral-intensity parameter the program calculates an error, which is defined by the difference between the area under the fitted peak and the integral value. This error is regarded as a meaningful empirical value.

Bottom row of buttons/fields:

- *save (ps):* saves the currently displayed plot to a post scrip file. The user is prompt to enter the name of the file in the terminal window.
- *save (ascii):* saves the currently displayed plot to a ASCII-file. The user is prompt to enter the name of the file in the terminal window.
- *error:* A toggle button to turn the display of the error-bar on and off.
- *log:* A toggle button for changing between logarithmic/linear y-axis display.
- *unzoom:* To go one step back in the zoom history.
- *replot:* Not all changes will automatically update the plot – In these cases clicking the "replot" button will update the plot.
- *Ol_cal:* Calculates the relative calibration factors (see overlap calibration).
- *(IDL)-save:* Will save actual program memory (not yet working!).
- *RESTORE:* Will restore saved program memory (not yet working!).
- *EXIT:* Kills the main widget and ends the main program.

Start Parameter

For the fit procedure an initial guess (set of start parameters) is required. The start values for the peak positions are given by the unshifted wavelength of the transition in question (= wavelength setting of spectrometer) and the Doppler-shift which is calculated from the geometry of the observation system and the He beam energy. The peak height is estimated by finding a local maximum in the vicinity of the estimated peak position. The peak-width is given by a constant value based on experience.

Parameter-widget: The start parameter for additional (disturbing) peaks are entered interactively. By clicking the "change/add param" button in the main widget, a new widget appears, showing the spectrum of the first active track at the active time (see Fig. 3.5). By clicking into the plot on the position of the disturbing peak, dragging the cursor to the flank of the peak at halfe maximum and releasing the mouse button, an additional Gaussian distribution is added and the position and FWHM are defined. These values are listed below the spectrum and can be edited there. The checkbox left of the fields indicates whether the fields are active or not.

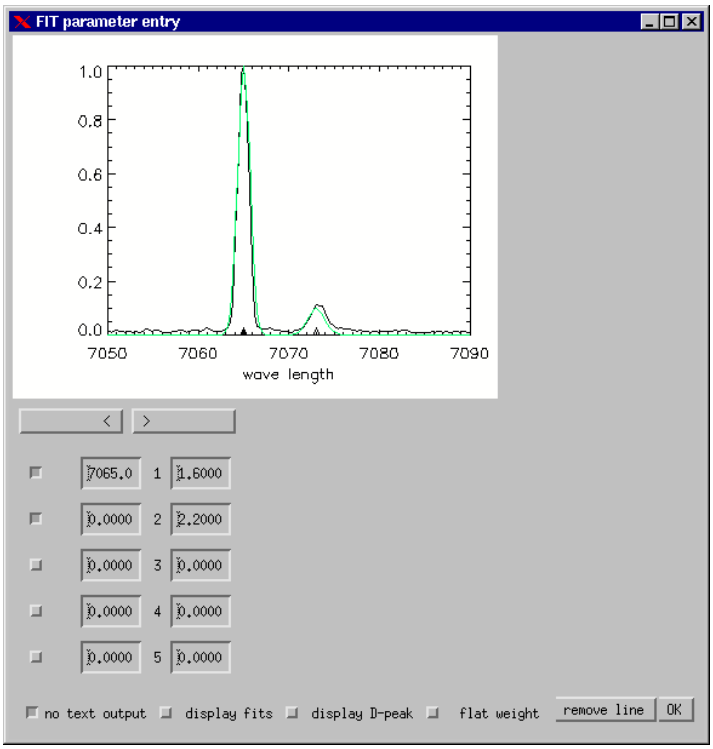

Fig. 3.5: Widget for the entry of the parameter for additional (disturbing) peaks.

If there are no additional (disturbing) peaks selected, only the first two rows of fields are active (unshifted and shifted HeI peak).

The initial guess of the fit-function is automatically displayed in colour on top of the spectrum to ease trouble shooting. The displayed spectrum can be changed by browsing through the active tracks with the back and forward buttons. However, the start values for position and FWHM of the disturbing peaks are the same for all tracks.

The bottom row of checkboxes in the widget have the following effect on to output of the fit program:

- No text output: If active, the extensive text output of `mpfit` will be suppressed.
- Display fits: The result of the fit (for all spectra of the active tracks for all frames of the selected time window) is being plotted instantly.
- Display D-peak: Instant display of the Doppler-shifted peaks, i.e. the measured spectrum subtracted from the resulting fit, leaving out the Doppler-shifted peak. Thus only the Doppler-shifted peak remains in the spectrum, provided that the fitting-procedure was successful.
- Flat weight: Overrules the standard weighting by a constant value for all pixels. In the standard mode the weighting decreases linearly with the distance outside the range of interest, defined by the two HeI peaks (shifted and unshifted).

Overlap calibration

In horizontal sweep experiments with a sufficiently large sweep range the mapped data for adjacent viewing lines are overlapping. Due to inaccuracies in the absolute calibration the profiles of neighbouring viewing lines are shifted in intensity against each other. By introducing an additional track-dependant calibration factor, the overlapping profile-parts can be matched against each other, leading to an increased quality of the profile shape. The automatic procedure performs a least-squares-optimisation of the calibration factors. During the run of the procedure all the overlapping profile-sections are plotted.

The resulting factors are displayed in the second column of the track information table. Below the table is a button (“set to 1”) for resetting this additional calibration factors to 1.

The size of the different active volumes are not taken into account, which means they are included in the track-dependent calibration factor!

3.4 Factors influencing the accuracy of the fit-result

3.4.1 Drift of the Doppler-shift during sweep experiments

The Doppler-shift is estimated by the analysis software (`he_wid`) taking the measured beam energy into account. The actual value of the Doppler-shift (converged value of the curvefit-parameter) can change during the sweep of the plasma. There are two reasons for the drift of the Doppler-shift.

1. Beam divergence

The finite beam divergence (typically ±0.7°) leads to a weighted sum of different Doppler-shifts. In Fig 3.6 this situation is illustrated. The angle between line-of-sight and the trajectory of the beam particle varies along the viewing line passing through the beam. In case the beam emission is almost constant within the active volume, the resulting Doppler-shifted peak is only broadened but not shifted. In case the beam emission has a steep gradient at the position of the active volume, one side of the beam has a higher weighting due to higher emission intensity. In Fig. 3.6 the beam emission is symbolised by the red shading. In the displayed case the emission is dominant in the upper region (smaller angle), and the observed Doppler-shift would be bigger then the expected (beam axis) value.

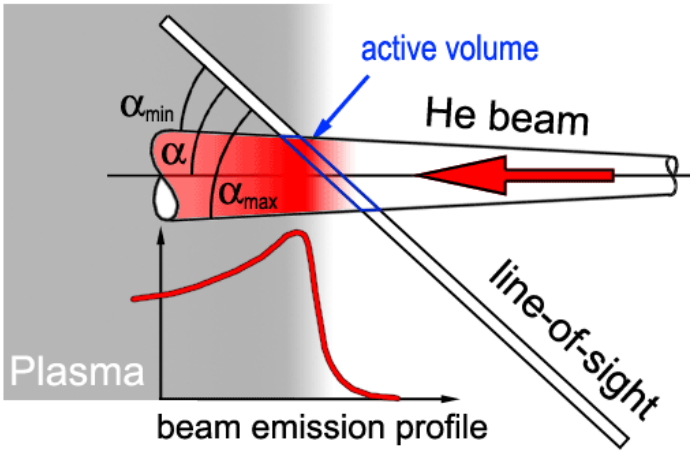

Fig 3.6: Sketch of the influence of the finite beam divergence on the net Doppler-shift.

In Fig. 3.7 the measured beam emission profile (upper plot) and the respective Doppler-shifts (lower plot) from a sweep experiment are displayed. In the Doppler-shift plot the different tracks corresponding to different viewing lines can easily be identified by their Doppler-shifts. The shown singlet emission profile (2^1P-3^1D) can be characterised by a sharp intensity increase near the plasma edge and a much slower decay towards the centre.

Only in the range with the large gradient we see a small drift of the Doppler-shift. Sufficiently deep inside the plasma the emission profile is almost constant and the Doppler-shift stays unchanged during the sweep.

For a beam energy of 134 keV and an observation angle $\alpha = 30°$ a change in the observation angle of ±0,5° would lead to a change in the Doppler-shift of ±0.05 nm for the $\lambda = 667.8$ nm line. The observed drift of 0.1 nm is therefore consistent with a very steep increase of the emission profile.

2. Disturbing peaks

Some of the observed drifts of the peak position are too high to be explained by the influence of the beam divergence.

In some of these cases an overlapping disturbing peak of low intensity could be identified. If the fit-procedure only interprets the two overlapping peaks as a single one, the spectral position of the compound peak will depend on the relative intensities of the two peaks.

During the sweep of the plasma the disturbing peak changes the intensity differently to the beam emission peak, leading to a drift of the compound peak.

This can be overcome by adding the disturbing peak to the fit-function used in the `he_wid` software. However, if the peaks are too close together, this fitting-procedure will fail. As a rule of thumb, if the merged peak can be visually identified as two peaks, the procedure has a good chance to succeed.

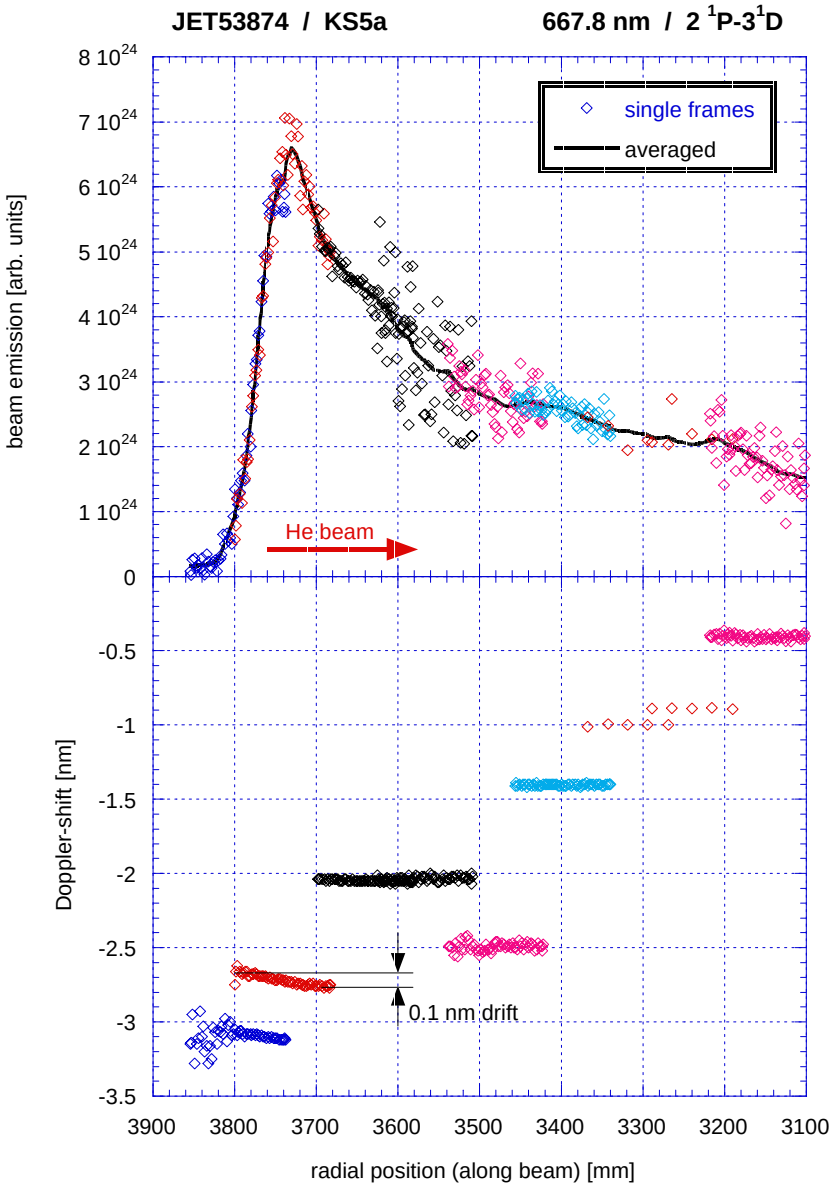

Fig 3.7: Intensity and Doppler-shift of the HeI (2^1P-3^1D) beam emission measured during a sweep experiment. At the location with high emission gradient a changing Doppler-shift is noticeable.

3.4.2 Dead pixel of the CCD sensor

For calibrating the KS4/5 diagnostics a white light source of know emissivity is observed (see chapter 3.5). Some pixels (picture elements) of the CCD sensors show for the whole wavelength range significant lower sensitivity than their neighbouring pixels. These so-called “dead” pixels can be identified in Fig. 3.9. In order to take the pixel dependence into account the sensitivity is measured pixel by pixel. The last calibration for the KS4/5 system was performed in 1999.

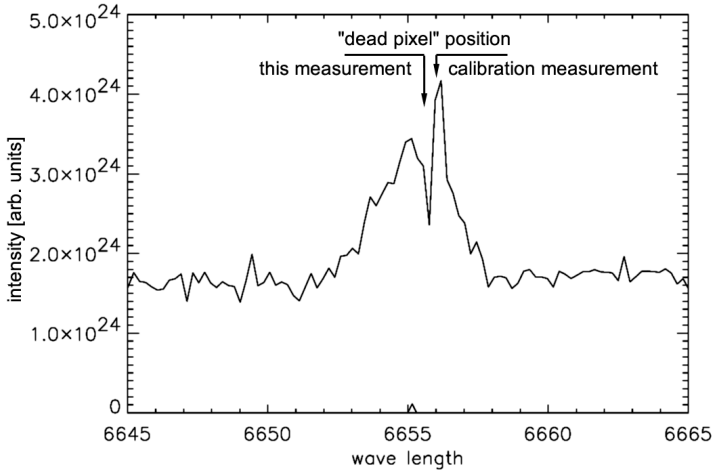

Fig. 3.8: Example of a spectrum with a dead pixel within the Doppler-shifted peak.

In the data taken in 2001 the position of the pixels with the low sensitivity appears to have moved by one or two pixel. The obvious drop in the number of counts for these pixels is independent of the wavelength setting of the spectrometer and was observed throughout the measurement campaign.

Fig. 3.8. gives an example where a “dead” pixel is within the peak of the Doppler-shifted beam emission. The data shown were already calibrated using the “1999” pixel by pixel sensitivity. At the position where the “dead” pixel was observed during the calibration measurements, the intensity is being overcompensated. On the other hand, a too high sensitivity is being applied to the neighbouring pixels, where the sensitivity has decreased since the last calibration measurements.

It is obvious that these inconsistencies in calibration can affect the peak height and width of the curvefit. This problem could be overcome by a new calibration of the instrument, which requires long torus-hall access and was therefore not possible at short-notice.

3.5 Absolute Calibration of the JET spectrometer

Ideally, the absolute calibration of the whole optical system (spectrometer, fibres, optical head and vacuum window) would be performed by monitoring the emission of a standard white light source (cavity with aperture with uniform emission in 2π) with a known emission placed at the location of the emitting plasma. In case of JET this is not possible. Instead, the optical head was taken out of the machine and placed in front of the light source, leaving the vacuum window excluded.

In case of our measurements with the KS7a system during the campaign the situation was worse. It was only possible to disconnect the fibres from the optical head and place them in front of the light source aperture, leaving the optical head and the vacuum window excluded. However, it should be sufficient for a relative calibration from wavelength to wavelength, because the wavelength dependence of the transmission of the optical head is expected to be small.

Comparing the measured intensity (counts/pixel) after the background subtraction at a given wavelength with the known emission of the lamp gives the sensitivity of the system at this wavelength. The spectrometer has been calibrated over the full range of wavelengths in steps of 10 nm. In order to get a statistical information of the calibration measurement, ten successive exposures with an exposure time just below signal saturation have been made for each measurement.

For the background subtraction (dark count rate), it is important to use the same exposure time for the background measurements. Therefore the respective set of background measurements with no light coming through the entrance slits has been made.

The single measurements are saved by the control software of the spectrometers into a binary file. All the files of the calibration measurements of one instrument are copied to a directory, including a ASCII-file containing a file-list with the important information of the measurements.

Three different IDL programs have been developed for processing the calibration measurements:

1) `build_sens_file.pro`
2) `merge_sens_files.pro`
3) `int_calibr.pro`

`build_sens_file.pro:`

This program reads in the ASCII-file containing the file list, all the binary files listed there, and the calibration file of the lamp used. It checks the consistency of the parameters stored in the file list with the information in the file headers of the binary files.

Sequence of processing the data from the calibration measurements:

- Building mean value and standard deviation for the 10 exposures (both measurements: background and light).
- Background subtraction (dark count rate).
- Calculate the wavelength for each pixel of the spectrum.
- Interpolate calibration curve of the lamp for each pixel (corresponding wavelength).
- Calculate sensitivity for each pixel from mean value of the measurement and the interpolated lamp emission.
- Store the calculated sensitivity in a three dimensional matrix [pixel, wavelength, track].

The 3D matrices of sensitivity and standard deviation are saved as an IDL save file. This file is afterwards accessed by the calibration routine (int_calibr).

It is important to keep the information of the pixel because the sensitivity can change substantially from pixel to pixel. In Fig 3.9 the calculated sensitivity is displayed as a contour plot together with one horizontal and one vertical cut. Because the standard display program was used the wavelength axis is marked with “time” instead of “wave length [Å]”. On can clearly see that some pixel have a significantly lower sensitivity over the full wavelength range (dead pixel or dust particle). In the near infra-red (NIR) region (λ>730 nm) the CCD sensor shows “etaloning”, an interference effect of back-illuminated CCD’s. They consist of thin films (typically 10-20 microns thick) which become semitransparent in the NIR. Reflections between the front and the back surface of these devices cause them to act as etalons, leading to unwanted fringes. These fringes can be seen in Fig 3.9 – if the bluish interference pattern around 750 nm.

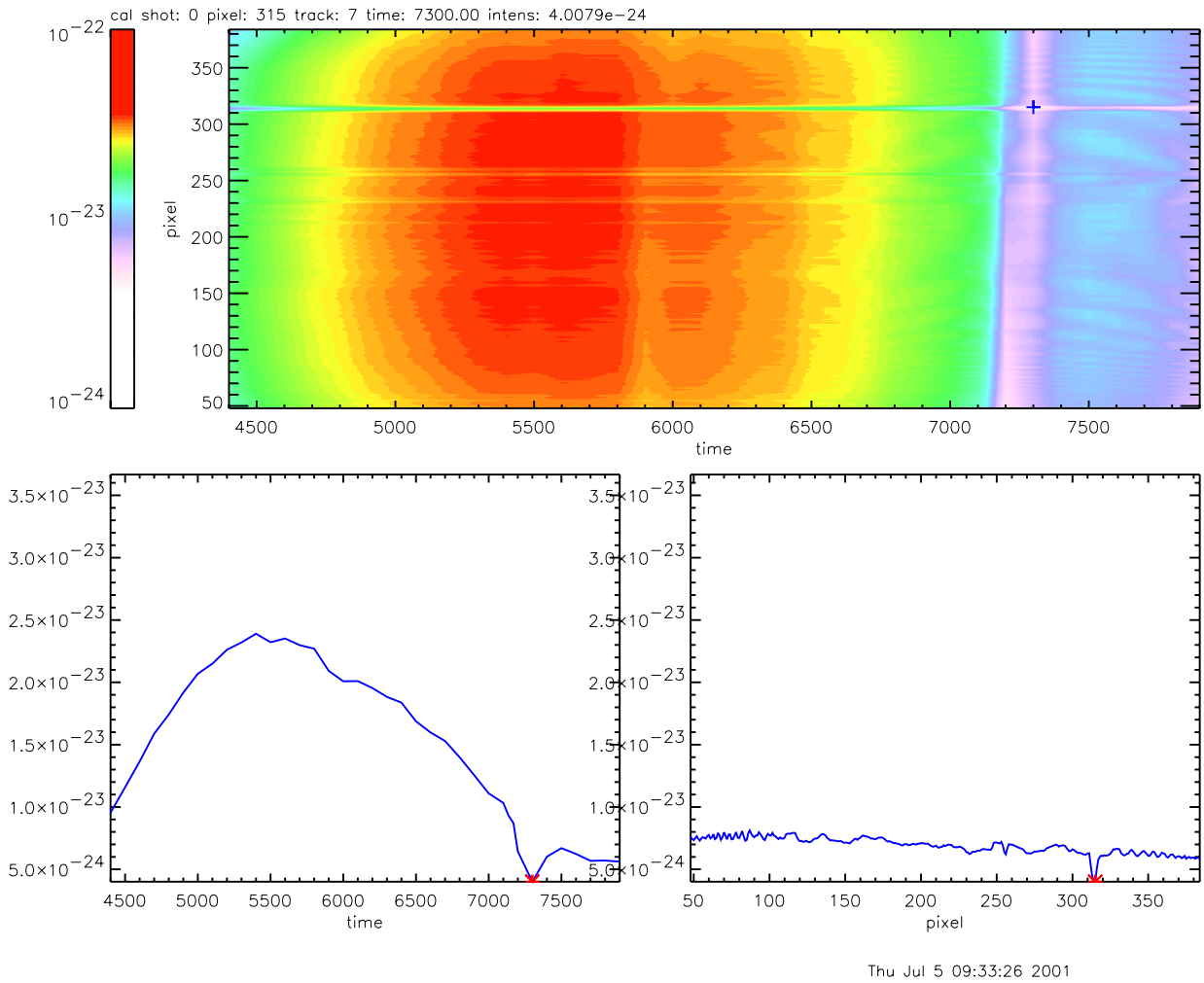

Fig 3.9: Sensitivity of track7/KS5a displayed with the `showspec` software (time = wavelength[Å]). "dead" pixel and etaloning can be clearly seen. The lower two graphs show horizontal and vertical sections through the upper graph, taken at the location of the cross.

The ratio between the measured standard deviation and the value for $\sqrt{counts/gain}$ yields a wavelength dependent value. If the noise would solely originate from photon statistics this ratio should be one and independent of the wavelength. One reason why a wavelength-dependent factor is being observed could be the continuous exposure of the CCD during the readout (shifting of the "image" across the sensor). Normally during the read-out of the CCD a shutter is closed in front of the sensor. At JET the shutters have been deactivated in order to reduce the minimum repetition time. Especially with only a small number of tracks (large binning) the readout time is very short compared to the exposure time. However, if the intensities between different tracks are very different, the influence of the exposure during readout of the "weak" track is not negligible.

`merge_sens_files.pro:`

The viewing lines of some diagnostic systems are grouped in two different periscopes and have to be calibrated separately. This is the case for KS7a and for KS5c. The program `merge_sens_files.pro` helps to merge two sets of calibration files and saves the combined sensitivities.

`int_calibr.pro:`

A call of this function returns the intensity calibrated data. It uses the sensitivity-files generated with build_sens_file.pro and merge_sens_files.pro for the respective spectrometer. At the moment sensitivity files for KS5a and KS7a are generated with the data from the latest available calibration measurements. It is planned to extend the code with a history of sensitivity-files, to be able to apply the appropriate calibration for each pulse number.

3.6 Alignment correction for AUG data

During the HeI beam emission measurements at AUG the alignment of the CER diagnostic to the beam was not perfect, making a correction of the measured beam emission intensities necessary.

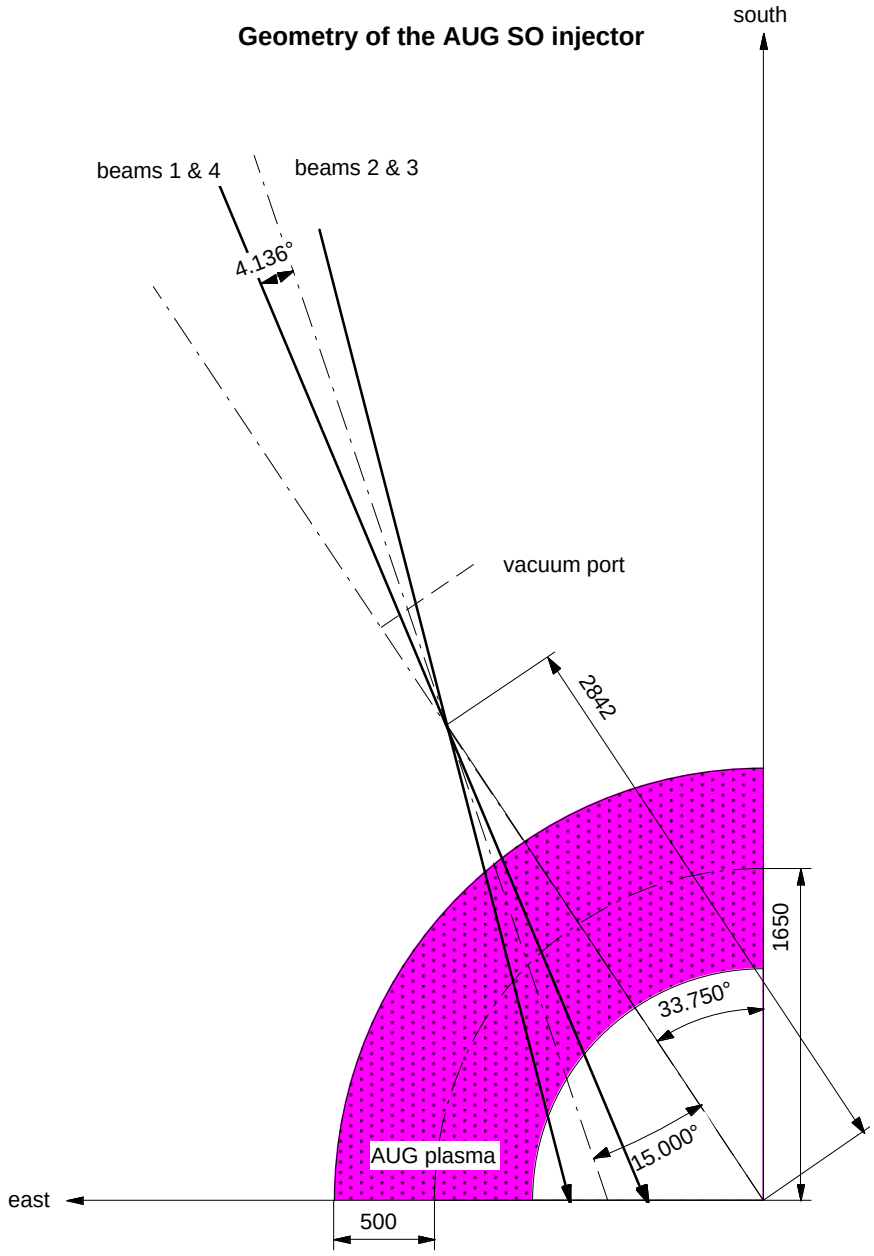

Fig. 3.10: Geometry of the AUG 60 kV injector. He beam emission measurements were performed with beam 3.

3.6.1 Geometry of the beam axis.

The co-ordinate system of the SO injector is shifted and inclined against that of the AUG tokamak. A point $\{u,v,w\}$ of the injector frame converts into the AUG $\{x,y,z\}$ frame through the transformation (cf. Fig. 3.10) .

$$\begin{aligned} x &= u\cos\varphi + v\sin\varphi + R\cos\gamma \\ y &= -u\sin\varphi + v\cos\varphi + R\sin\gamma \\ z &= w \\ \text{with}\quad R &= 2.842m,\quad \gamma = 33.75^0,\quad \varphi = -18.75^0 \end{aligned} \tag{10}$$

Using two points on the beam axis, namely the centre of the grid $\{u_1,v_1,w_1\} = \{6.5,\ -0.47,\ -0.6\}$ and the cross-over of the beam axes from source Q3 and Q4 with the co-ordinates $\{u_2,v_2,w_2\} = \{0,\ 0,\ -0.0429\}$ we get the equation of the beam axis in the form

$$\frac{x-x_1}{x_2-x_1} = \frac{y-y_1}{y_2-y_1} = \frac{z-z_1}{z_2-z_1} \Leftrightarrow \frac{x-x_1}{a} = \frac{y-y_1}{b} = \frac{z-z_1}{c} \tag{11}$$

3.6.2 Geometry of the optical lines-of-sight

From the optical lines of sight the locations of the mirror and of a calibration target are known. The calibration target was installed inside the AUG vacuum chamber near the axis. By converting into Cartesian co-ordinates, we get the equations for the individual lines of sight in the same form as for the beam axis using $\tilde{a}, \tilde{b}, \tilde{c}$ *and* $\tilde{x}_1, \tilde{y}_1, \tilde{z}_1$ for the respective constants. The minimum distance between beam- and line-of-sight axis is then given by equation (12) and can found in [#Bronstein#].

$$d_{\min} = \frac{\begin{vmatrix} x_1-\tilde{x}_1 & y_1-\tilde{y}_1 & \tilde{z}_1-\tilde{z}_1 \\ a & b & c \\ \tilde{a} & \tilde{b} & \tilde{c} \end{vmatrix}}{\sqrt{\left\{\begin{vmatrix} a & b \\ \tilde{a} & \tilde{b} \end{vmatrix}^2 + \begin{vmatrix} b & c \\ \tilde{b} & \tilde{c} \end{vmatrix}^2 + \begin{vmatrix} c & a \\ \tilde{c} & \tilde{a} \end{vmatrix}^2\right\}}} \tag{12}$$

The angle α between the line of sight and the and the beam axis is given by

$$\cos\alpha = \frac{\vec{x}_1\vec{x}_2}{|x_1|\cdot|x_2|} \tag{13}$$

where $\vec{x}_1$ and $\vec{x}_2$ are vectors parallel to He beam axis and the line-of-sight.

Finally, the radius of the point of minimum distance between beam axis and line-of-sight can be estimated from the projection of the two axes into the z = 0 plane. This is justified as the cross-over is actually very close to the mid plane. From the minimum distance between beam axis and line-of-sight, we can calculate a correction factor which compensates for the reduced beam current when moving away from the beam axis. Neutral

beams at a sufficiently large distance from the beam source are normally well described by a Gaussian curve and the correction factor is therefore

$$c_v = e^{-\frac{d_{\min}^2}{\lambda^2}} \text{ with } \lambda = l \cdot \tan\omega . \tag{14}$$

l is the distance between beam source and cross-over point, and ω is the divergence angle of the beam. The correction is required as the individual lines of sight are staggered in z direction and thus have an alternating distance from the beam axis leading to a zigzag profile. The exact value of the correction is critically dependent on the quality of the alignment. The beam alignment is normally different from the optical alignment of the ion source due to deformation of the vacuum housing, sagging of the accelerator grid support, bending and thermal expansion of the grids, and deflection by earth magnetic or stray magnetic fields. Therefore, the accurate alignment of a powerful neutral beam can only be achieved by using the beam itself[3], and it is limited by the quality of the beam diagnostics.

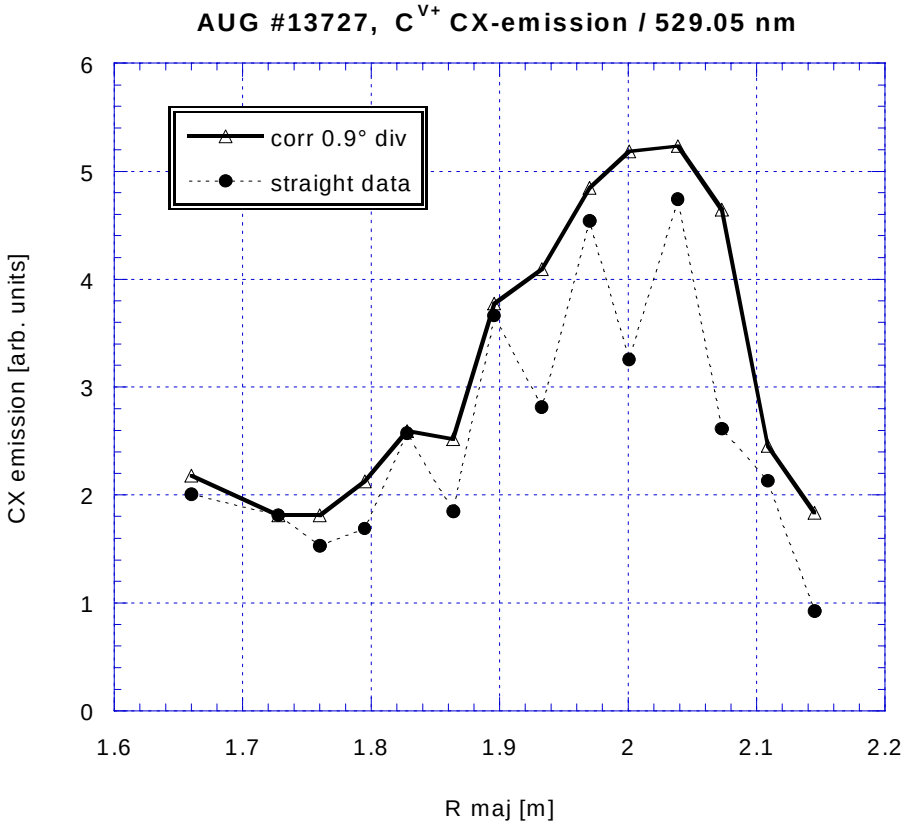

Fig. 3.11: The zigzag of the data retrieved with the "`cer-wid`" evaluation software disappears if the intensities are corrected by the beam intensity at the crossover between beam and viewing line. Assumed beam divergence: 0.9°.

[3] In the case of the AUG injectors, the beam alignment is adjusted so that the power loading on scrapers above and below the beam are equal.

Using the standard C^{5+} CX-line emission at 5290.5 Å, for which the CER spectrometer is calibrated and normally used for, we find that the raw data[4] in Fig. 3.11 are well smoothed if we assume a beam divergence of 0.9 degree and no misalignment of the beam. It is noteworthy that the quoted divergence of 0.9^0 is practically identical with the measured divergence of a D-beam.

The dissociation of D_2-molecules in the ion source leads to an additional energy spread of the beam particles and consequently to a higher beam divergence then in the case of the atomic He beam. Therefore a divergence of 0.75° is assumed for the He beam (or He fraction of a doped beam). Fig 3.12 shows the HeI beam emission profile (667.8 nm / 2^1P-3^1D) of a doped He/D beam. The zigzag behaviour of the straight data (solid dots) is not compensated over the whole radial range when applying a correction with a beam divergence of 0.75° and no misalignment of the beam (dashed line). When assuming the same beam divergence, but a misalignment of 0.15° the correction seems to work for a different radial range (solid line).

A different alignment of the beam could be explained by stray- or earth magnetic fields before the neutralisation occurs, which influences the D- and He fractions differently. Furthermore, the smaller divergence of the He beam leads to an even higher sensitivity to misalignment.

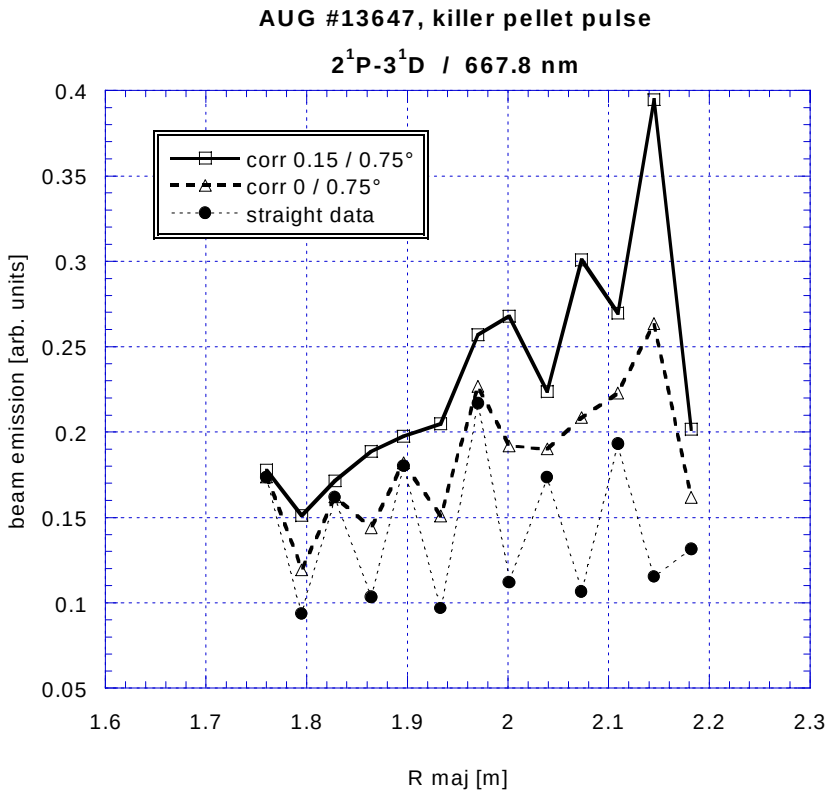

Fig. 3.12: HeI beam emission profile (667.8 nm / 2^1P-3^1D) of a doped He/D beam.The straight data and two corrections with different parameters are shown.

[4] Raw data are the output data of the `cer-wid` program. These are already processed data but without the correction for the beam alignment.

4 Reversion of HeI beam emission profiles into density- and temperature profiles (code: yttocs)

In this chapter the algorithm of the reversion code "yttocs" and some first results are presented. The code extracts desired electron density- and -temperature profiles from a set of HeI beam emission profiles. The inverse problem (modelling of the beam emission from given density- and temperature profiles) is calculated by the code "scotty", therefore the name "yttocs" was chosen for the reversion code.

IDL (interactive data analysis language) is used as development platform for various reasons:

- Compatibility: IDL is used for the data analysis at JET and AUG, and also as the graphical user interface (GUI) in ADAS.
- The graphics output, which can be easily integrated into the programmes, is ideal for testing the code during all development stages.
- GUI windows (so called "widgets") for a comfortable and interactive user interface are easy to create.

4.1 Basic algorithm

The basic algorithm of the conversion code is a variation method with two nested iteration loops. The code calculates the HeI beam emission profile from an initial guess of the electron density-, electron temperature- and Z_{eff}-profiles (forward calculation). The input-profiles are then adapted iteratively with the aim to minimise the quadratic deviation between calculated and measured beam emission profiles. As profiles parametrised functions are being used. This limits the number of parameters of the optimisation procedure and avoids unphysical profile shapes.

The flow diagram (Fig. 4.1) shows the two levels of iteration. Within the two inner loops the parameters from either the electron density- (n_e) or the electron temperature (T_e) profile are varied and the beam emission profile is calculated. This iteration continues until the quadratic deviation between the calculated and measured emission profiles has converged (i.e. the change in the quadratic deviation of consecutive steps is below a given limit). The optimisation of these inner loops is performed by the fit-procedure mpfit, which is also used in the spectral fit software he_wid (see chapter 3.1).

The code of the outer loop is kept versatile in the sense that the sequence of variations (e.g.: n_e, T_e, n_e, T_e, ...) and the choice of the respective emission profiles to be fitted ones can be changed easily. More details on the sequence of variations can be found in chapter 4.4. The straightforward approach is as follows:

A sensitivity analysis [43] has shown, that the 667.8 nm line (2^1P-3^1D) is almost exclusively sensitive to electron density, and several of the investigated triplet lines (incl. the intensive 2^3P-3^3D transition 587.6 nm) are sensitive to both electron temperature and -density. Therefore, within

the n_e-loop (first inner loop) the density profile is optimised based on the 667.8 nm emission profile. Subsequently the density profile is kept fixed, and the temperature profile is optimised based on the 587.6 nm emission profile (second inner loop). Both loops are being repeated (outer loop) until a truncation condition is reached. This is the case when the change of the total deviations of consecutive steps (from the outer loop) is below a given limit. The total deviation is defined by the sum of the quadratic deviations between measured and calculated emission profiles of both lines.

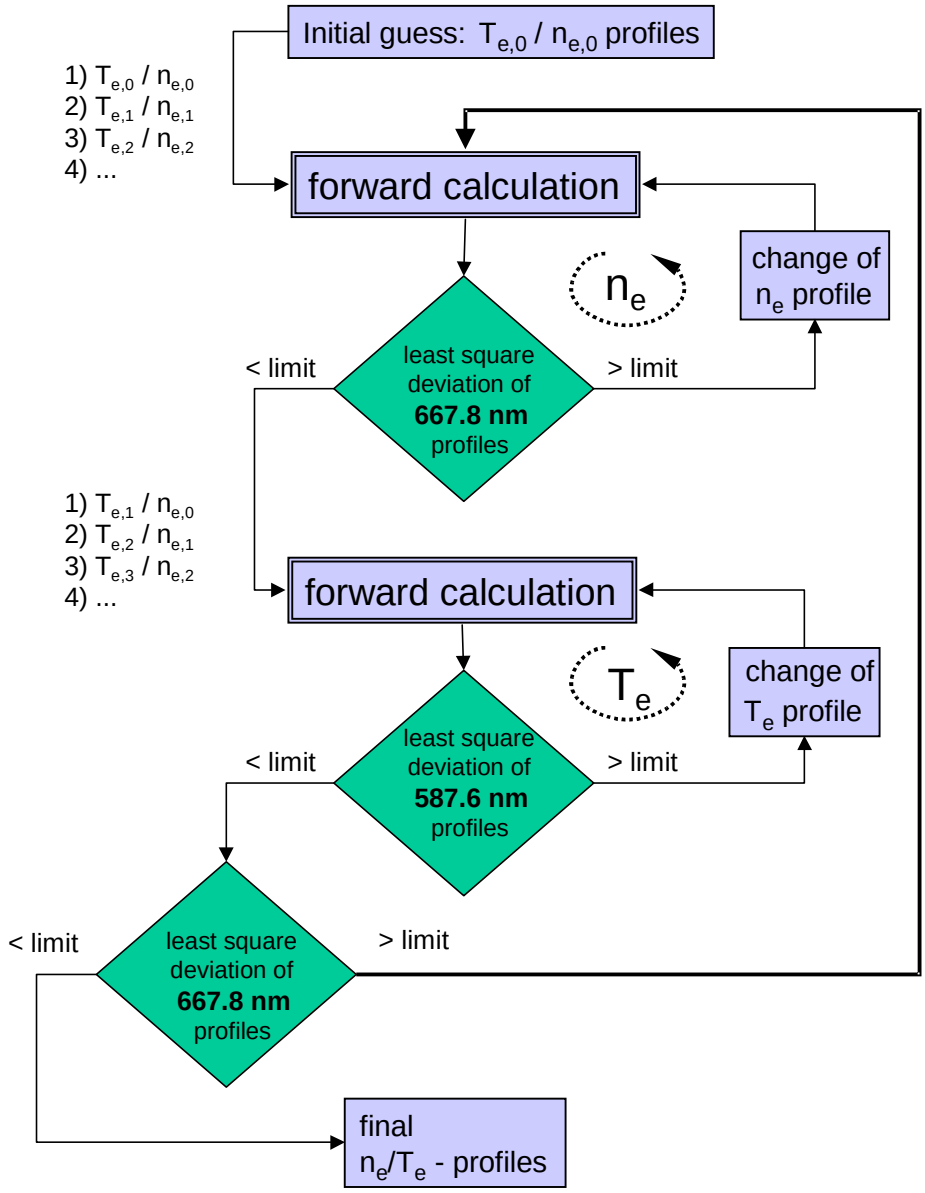

Fig. 4.1: Flow diagram of the basic algorithm of `yttocs`. The wavelengths and the order of variations within the inner loop are only examples.

The code was developed in four stages

1) The **"forward calculation"** of the emission profiles, i.e. the calculation of the HeI beam emission from given n_e, T_e and Z_{eff}-profiles. This code is based on the C-code "Scotty", written for the He beam modelling [29]. The code has been rewritten in IDL and is now called "scotty_fwd". The extension "_fwd" indicates that the actual calculation of the beam emission is performed by a subroutine called "forward_calc" which is a streamlined version of Scotty suitable for the variation method of the conversion code (see chapter 4.2).
2) Derivation of n_e- or T_e-profile with all other parameters fixed. These so called **"inner loops"** have been developed and tested separately. The beam emission profile is fitted by varying the parameters of the n_e- or T_e-profile, making use of the mpfit-package [41]. Part of this development step was to define a suitable parametrisation for the n_e- and T_e-profiles (see chapter 4.3).
3) Derivation of n_e- and T_e-profile using Z_{eff} (given and fix).
4) Including Z_{eff} in the optimisation.

4.2 Forward calculation (scotty_fwd)

For the forward calculation – i.e. model calculation of the HeI beam emission with given n_e-, T_e- and Z_{eff}-profiles – both programms scotty_fwd and yttocs are calling the subroutine forward_calc. Their algorithm is based on the original scotty code [32]. However some substantial improvements as described in the following have been implemented.

The forward_calc routine solves a collisional-radiative model for a given He beam into a given D-Plasma. A short summary of the model is given in chapter 1.3, for more details see [29]. The atomic data used by the code are accessed from lookup tables generated by the ADAS 311 code [31]. In these ASCII-files, tables of so-called 'generalized radiative coefficient'-matrices (GRCs) are stored for a certain number of plasma-densities and -temperatures.

The matrix element M_{ij} gives the effective change in population of level j out of level i. For i=j the matrix element M_{ii} gives the loss rate due to ionisation. The number of HeI levels to be included can be set for the generation of the lookup tables. The other levels are assumed to be in equilibrium with the included non-equilibrium levels.

The original scotty code used GRCs of the size 3 x 3 (ground- and the 2 metastable states) and assumed all other levels to be in equilibrium with them. The new subroutine forward_calc was designed for variable matrix sizes, however it was only tested for 11x11 matrices (all levels with n<4).

For the concept of an iterative conversion code it is essential to keep the computation time of the forward calculation sufficiently low.

The new scotty_fwd code needs less then 5 seconds which is acceptable for the reversion code. This performance improvement could be achieved by the following measures.

1) The new code loads the whole lookup table into the memory, eliminating the slow file access for each calculation step (several 1000 steps per profile).
2) The step-width is dynamically changed, keeping the total number of steps to a minimum.
3) The size of the matrix (number of non-equilibrium levels included in the calculation) can be changed. The gain of calculation speed with smaller matrices is twofold. All the matrix operations are faster and the numerical stability of the code is better leading to bigger step-widths and consequently a smaller total number of steps.

Synthetic emission data

For the development of the reversion code it is adventageous to generate synthetic "measurement" data. The small code art_data performs a forward calculation (call of scotty_fwd) extracting beam emission profiles from density- and temperature profiles. This emission profiles are then modified in order to get realistic "measurement" data. The modifications include the averaging of the emission data over a given radial range (typical 50 mm) to simulate the limited resolution of the BES, and the addition of a realistic level of noise (typical 5%). The advantage of using synthetic data is twofold. First the original input-data are known, and therefore the correct result of the reversion, and secondly the influence of the uncertainties in the atomic data-set cancel out.

4.3 Profile parametrisation

There are two different ways of defining the input profiles for the fitting procedure - a global and a local approach.

1) global: The entire input profiles are represented by parametrised functions (some 5 parameters), and the profile as a whole is matched.
2) "local": The profiles are defined step by step, starting from outside of the plasma. The word "local" is under quotation, because the measured beam emission is not only a function of the local density and temperature, but also dependent on the local population of the atomic levels in the beam produced in the layers which the beam has already passed.

In the stepwise attempt errors would sum up quickly and propagate with progressing forward calculation (in beam direction). The method would therefore be very sensitive to noise in the data and local imperfections of the calibration.

The global approach, on the other hand, can introduce unintended limitations in the profile-shape if unsuitable fit-functions are selected. The main advantage of the global approach is that it is easier to incorporate global properties as the initial metastable population in the beam or the

impurity profile in the plasma. That was the main reason for using a global approach for the development of `yttocs`.

The function `prof_funct` calculates the profile defined by the fit-parameters varied and matched to the data by the fit-code and some fixed parameters. The latter are passed via common block variables. The fixed parameters are the name of the defining function (e.g. 'spline + exp') and the positions of spatial fixed points (e.g. spline-knots).

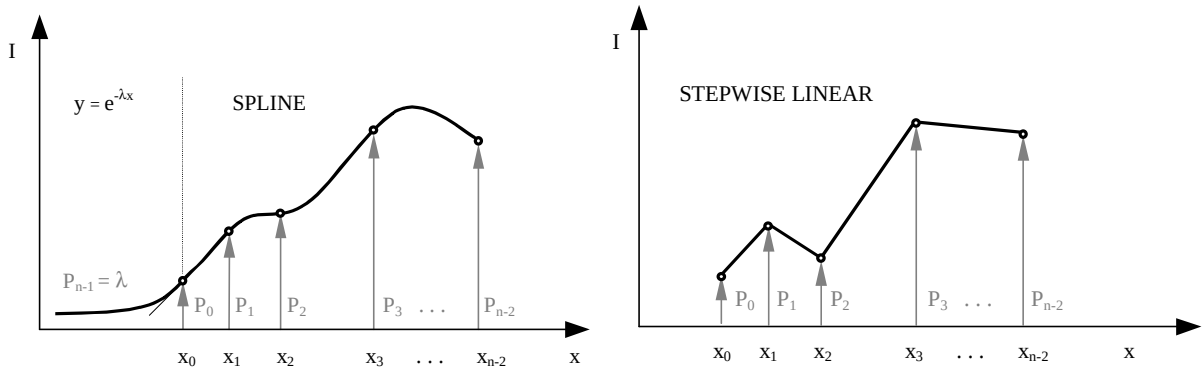

Fig 4.2: Examples for the parametrisation of the profiles. P_i are the parameters changed by the fitting-procedure. In both examples they are restricted to positive values. The x_i are the fixed spatial positions of the knot points.
Left: SPLINE-curve (plasma core) joined to an exponential decay (plasma edge) is used to describe the electron density profile.
Right: Stepwise linear profile, with positive values only, but no further restrictions, is used to describe the electron temperature profile.

Part of the development was to define a suitable parametrisation, compromising between excessive freedom and too many restriction. Excessive freedom can lead to unphysical solutions, too many restrictions can suppress features of the profile and also hinder the convergence. A good description of the electron density appears to be a spline-curve (plasma core) joined to an exponential decay (plasma edge). For T_e and Z_{eff} continuous spline-curves or stepwise linear functions (see Fig 4.2) are suitable. The code is written in a way to make the addition of new profile parametrisation quite simple.

When choosing the parametrisation one has to be aware of the fact that it defines the possible profile shapes, but also may influence the convergence behaviour.

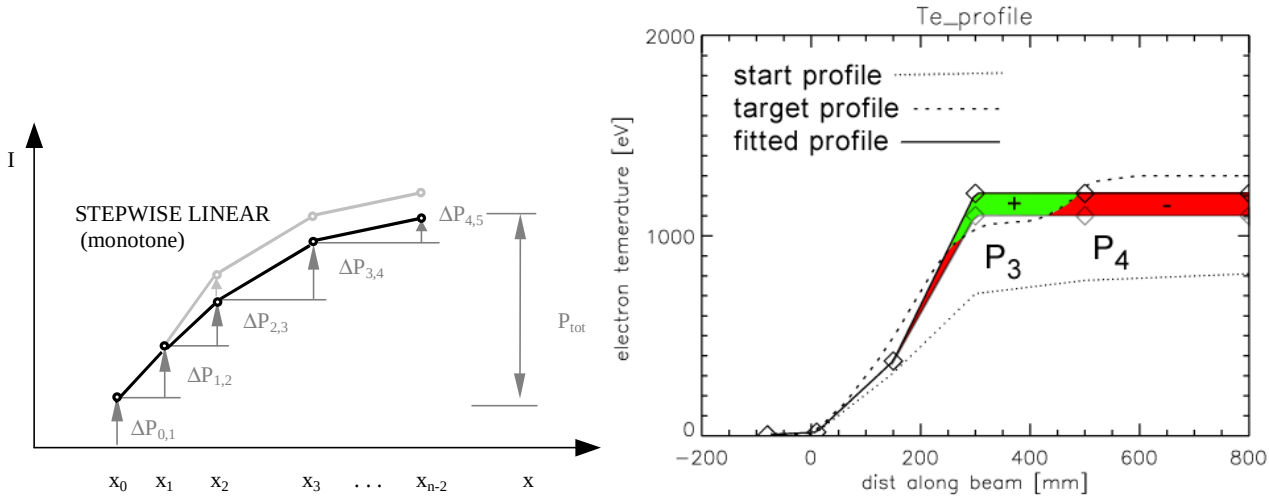

Fig 4.3: Illustration of the convergence problem due to parameter restriction. Left: Parametrisation for monotonously increasing function (stepwise linear). Right: An illustration of the resulting convergence problem. The dashed line shows the target profile, the dotted line the start profile of the fit-procedure, and the upper solid line the "converged" result.

A typical convergence problem due to parameter restriction is shown in Fig 4.3. On the left side the parametrisation of a stepwise linear function is sketched. The positions $x_0 ... x_{n-2}$ are given, and the parameters P_0 ... P_{n-1} are restricted to positive values, allowing only monotonously increasing profiles. This restriction leads to a convergence problem illustrated in the right plot of Fig 4.3. The dashed line shows the target profile (i.e. the original temperature profile used to generate synthetic emission data), the dotted line shows the profile at the beginning of the fit-procedure, and the upper solid line shows the resulting "converged" profile. Obviously the value of the knot defined by P_3 is too high, although the chosen profile-type would allow to reproduce the target profile. The reason behind this is that parameter P_4 is defined from P_3 through the increment $\Delta P_{3,4}$. Reducing the value of P_3 (only) also changes the value of the nodes P_4 and P_5 in the way indicated by the lower solid line. The profile-segments where this parameter-change would have a beneficial effect on the total deviation are shaded green and marked with a plus symbol (+) and those with adverse effect are shaded red and marked with a minus symbol (-). One can see that reducing the value P_3 would increase the total deviation between emission-data and forward calculation. A combined variation of P_3 (increasing) and P_4 (decreasing) would lead to a better match. However, the number of permutations to cover all possible combinations is quite high already for a small number of parameters. Equation 15 gives the total number of combinations *N* for a given number of parameter *n* is calculated (taking positive and negative changes into account):

$$N = 3^n - 1 \qquad (15)$$

For the case discussed above (6 parameters) the number of forward calculations for one iteration of the fit-procedure would be $N = 728$. Taking the typical duration of one forward calculation (5 seconds), a single iteration of the fit procedure taking all *N* combinations into account would last more then one hour and is therefore impracticable.

Additional (global) parameters

Some additional parameters – i.e. parameters which do not define the shape of n_e- and T_e-profile – can be included in the list of parameters to be adjusted by the fit-routine:

- The initial population of the He metastable singlet level (2^1S)
- The initial population of the He metastable triplet level (2^3S)
- The shape of the Z_{eff} profile (Fig. 4.4). The Z_{eff} profile is assumed to be parabolic. The mean value is treated as input parameter, while the value of Z_{eff} at a certain position (e.g., the plasma core) can be used to improve the fit.. This definition allows to define the parameter range for hydrogen plasmas to:

$$1 \leq Z_{eff,core} \leq Z_{eff,mean}$$

$$Z_{eff,core} \leq Z_{eff,mean}$$

A flat profile is defined by $Z_{eff,core} = Z_{eff,mean}$.

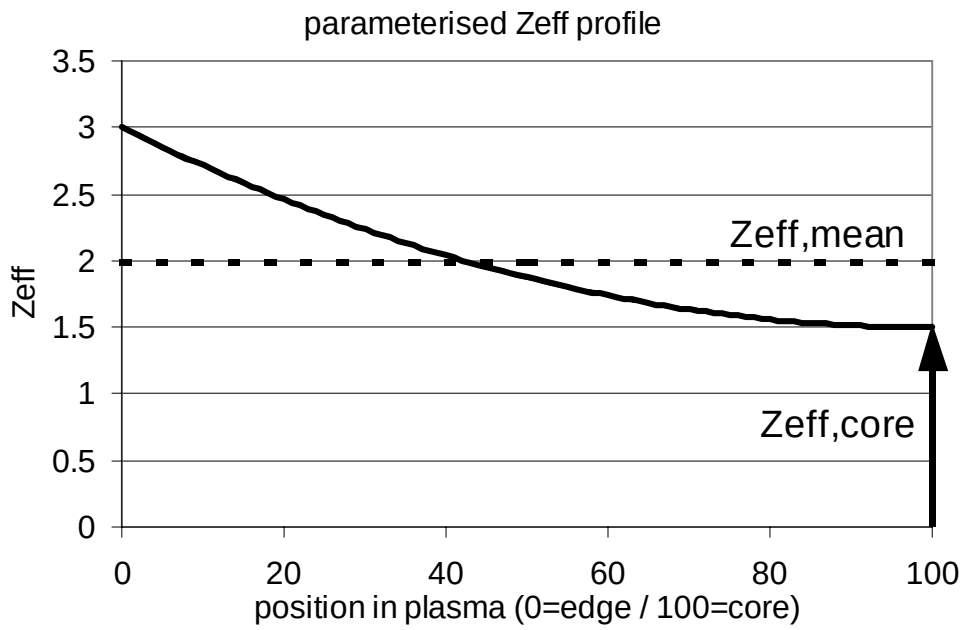

Fig. 4.4: Parametrisation of the Zeff-profile, defined by only two values: $Z_{eff,mean}$ (given and fixed) and $Z_{eff,core}$ (to be adjusted by the fit-procedure).

This definition of Z_{eff} reflects that the impurities mostly originate from the plasma wall or from impurity puffing. The actual impurity profiles in fusion plasmas are not well known yet, and the present definition has to be regarded as a first artificial step.

4.4 Weighting and mixing

The independent variation of electron temperature- and -density profiles can cause the following minor problems :

1. For some test data the convergence of the whole calculation (not of the single fits) showed an oscillation between the two independent optimisation loops (fit of singlet- and triplet emission profile).
2. Although the used HeI transitions are mainly sensitive to either electron temperature (T_e) or -density (n_e), in particular for the triplet lines there is a certain sensitivity to the respective other parameter as well. Features from the T_e-profile can for example be seen in the beam emission profile used to derive the n_e-density profile. However, the fitting algorithm tries to reproduce this "T_e"-feature in the n_e-profile.

These problems can be overcome by introducing some kind of damping or by modifying the sequence of fitting beam emission profiles.

<u>Weighting</u>

In order to damp possible oscillations, an "underrelaxation" parameter w is introduced. The weight *w* determines to which extent the old parameters (p_i) are changed towards the values (p_{i+1}) returned by the fit.

$$\bar{p}_{i+1} = p_i + (p_{i+1} - p_i) \cdot w \tag{16}$$

In equation (16) the parameter value *p* after the iteration *i+1* (outer loop) is calculated. The weight *w* must stay within the range

$$\begin{cases} 0 \text{ ... the old parameter } p_i \text{ stays unchanged (maximum damping).} \\ 1 \text{ ... the new parameter } \bar{p}_{i+1} \text{ is used unchanged (no damping).} \end{cases}$$

A weight $w = 0.5$ leads therefore to a parameter value which is the mean value of the preceding and the current value.

Because the calculation of the beam emission (forward calculation) is non-linear in n_e and T_e, the combination of both parameters is not necessarily a solution. However, once converged, "old" and "new" parameters are the same and therefore their "combination" is also a solution of the forward calculation.

Examples for a yttocs-calculation with and without damping of the parameters are shown in Figs. 4.5 and 4.6. The output-sheet for each run consists of the density- and temperature profiles at the top, the beam emission profiles of a singlet- and a triplet line (middle), and the convergence plot (bottom). The input profiles, emission data and profile parametrisations have been the same for both runs. "Measurements" shown

as symbols in the beam emission plot are synthetic data. The density and temperature profiles which the reversion code should return are therefore known (see chapter 4.2) and shown as dashed lines in the density- and temperature profile plots. For the damped case the weights are 0.8 for the n_e-parameter and 0.7 for the T_e-parameter.

Comparing the convergence plots in Fig. 4.5 (without damping) and Fig 4.6 (with damping) clearly shows the improved convergence achieved by the damping. Apart from a faster convergence, the damping also results in better fits, as can be seen from the smaller total deviation in the case of damping or from the better profile match between fitted result and actual input profile.

In the case of a calculation with damping the temperature profile is correct in the range where the beam emission data are sufficiently large. On either side of the beam emission profile of the triplet line the data converges towards zero and the fit returns very high temperature values. This unrealistic high temperature at 800 mm pushes the returned density up beyond its correct value.

Description of the `yttocs`-output-sheet (Fig 4.5+4.6):

The output-sheet stored by `yttocs` contains five plots and a text-section.

The two plots of the first row show the input-profiles (n_e and T_e). The dotted lines show the start-profiles at the beginning of the optimisation, the dashed lines the artificial input-profiles used to generate the data, and the solid lines the result of the optimisation. The knot points defining the parametrised profiles are shown as diamond symbols in the same plots.

The two plots of the second row show the two emission profiles, both the assumed measured data (diamonds) and the results of the fit (solid lines). The emission profiles which were forward-calculated from the start profiles are plotted as dotted lines.

The bottom plot shows the convergence behaviour by giving the total deviation between fit and measurement for the iterations of the outer loop. The abscissa gives the number of `fwd_calc`-calls.

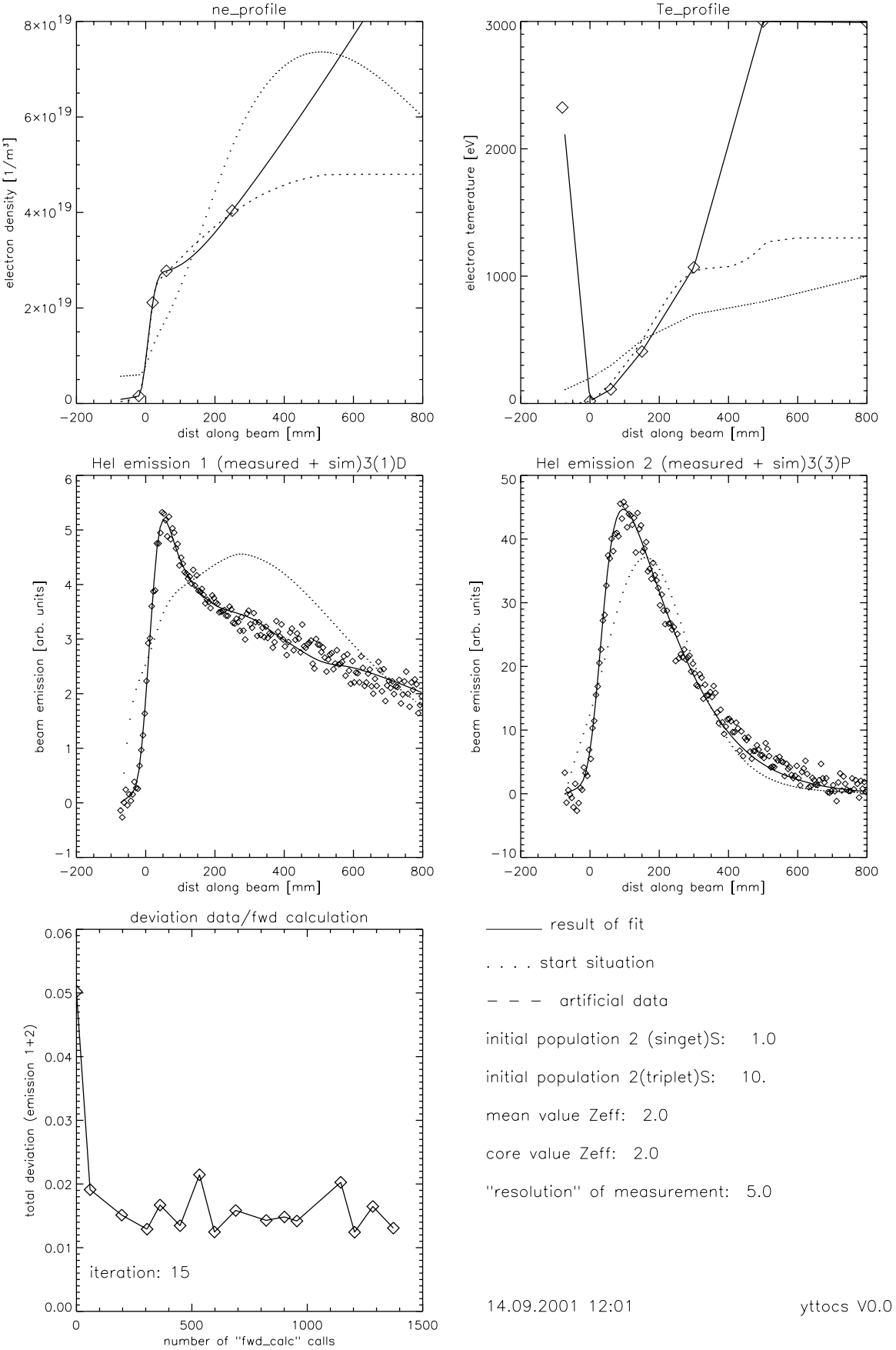

Fig 4.5: Output sheet from `yttocs` for a undamped variation sequence.
A description of the output-sheet is given on the preceding page.

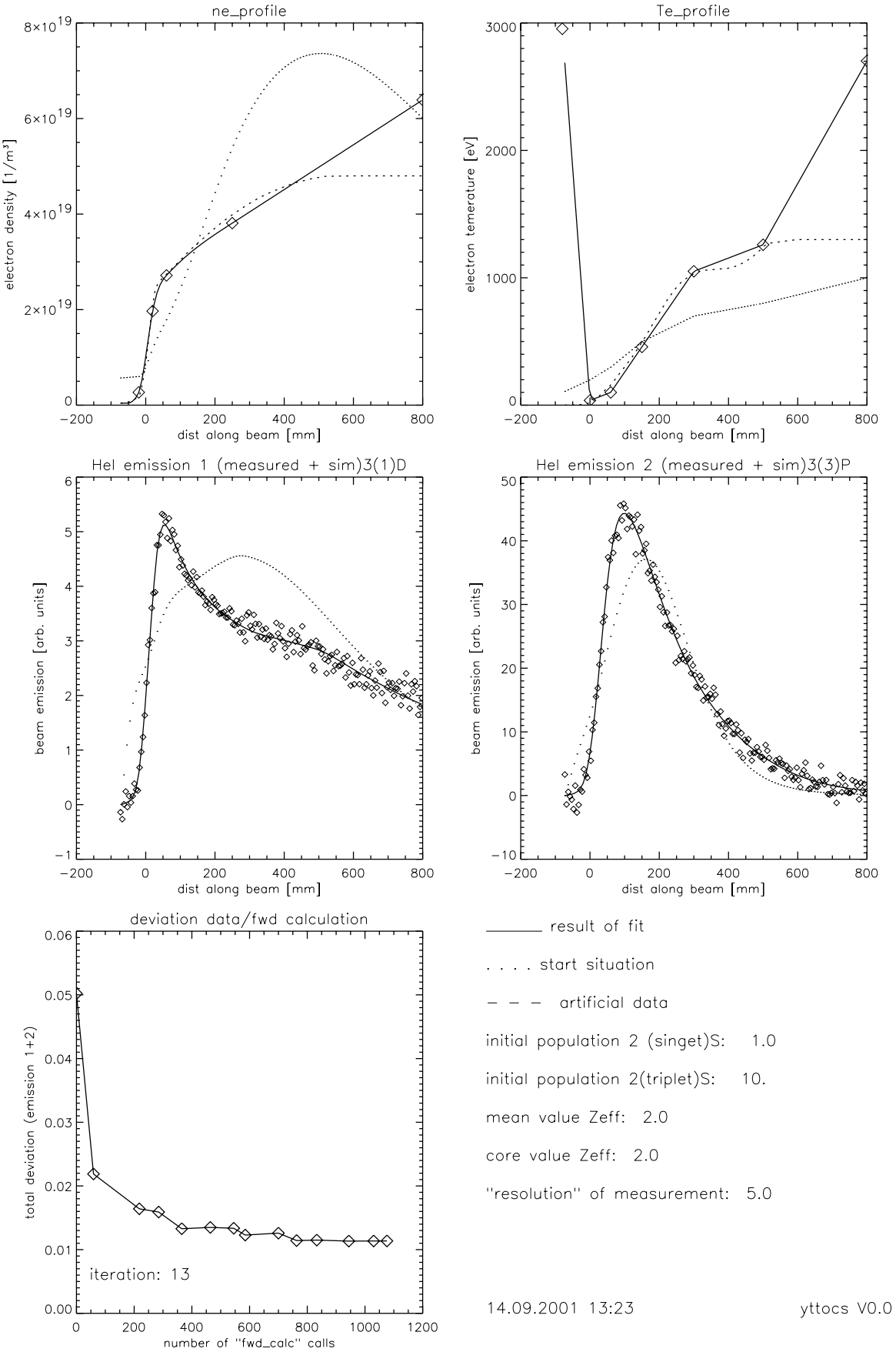

Fig 4.6: Output sheet from `yttocs` for a undamped variation sequence.
A description of the output-sheet is given on the page 102.

Variation of the fitting sequence

Instead of following the sequence shown in Fig. 4.1, where the density profile is sequentially used to fit the beam emission profile of the singlet line, and the temperature profile to fit the emission profile of the triplet line, a predefined sequence can be used.

In the actual yttocs-code this sequence can be defined easily by editing the three defining arrays:

- loop_seq ..... Array containing the code for the parameter set to be optimised
- level_seq ..... Array containing the index for the emission profile to be fitted to
- weight_seq ..... Array of the weights

Example:

```
loop_seq  =['ne','te','ne','ne','te','te','ne','te']
level_seq =[ 1  , 2  , 1  , 2  , 1  , 2  , 1  , 2  ]
weight_seq=[ 0.8, 0.7, 0.8, 0.4, 0.4, 0.7, 0.8, 0.7]
```

In order to see the effects from both n_e- and T_e-profile on the beam emission profile, a sequence of combinations of emission-profile and fit-parameter set can be run through. Different weighting for each step results in a defined combination of the results from consecutive steps.

E.g., two steps with both n_e-profile variation – the first for optimising a singlet-emission-profile (e.g. 667.8 nm) and the next step a triplet-emission-profile (e.g. 587.6 nm) – would lead to a n_e-profile which is a weighted combination of both results. In some cases the convergence of the whole problem is improved in that way. However, it is important to choose the right weights. A too small weight can lead to a false convergence too close to the start-values, and a too high weight leads to oscillations.

The code can deal with all possible combinations and permutations. To make the idea behind it clearer, three examples are shown below

1) Derivation of the electron density by fitting one emission profile can be realised by defining the following “sequence”:

```
loop_seq  ='ne’
level_seq = 1
weight_seq= 1.
```

   The electron temperature is given and remains unchanged.

2) The electron density can be also derived by including the information from two emission profiles with different weights, and leaving the given temperature profile unchanged. This would be realised with the sequence:

```
loop_seq  =['ne','ne']
level_seq =[ 1  , 2  ]
weight_seq=[ 1. , 0.4]
```

3) The standard sequence used for the analysis of the measurements:

```
loop_seq  =['ne','te']
level_seq =[ 1  , 2  ]
weight_seq=[ 0.8, 0.7]
```

4.5 Factors influencing the accuracy of the result

We have to distinguish between uncertainties of the atomic data-set and errors of the measurements. This chapter focuses on the latter.

4.5.1 Absolute Calibration

The `yttocs` code provides absolute values for the density- and temperature profiles. This output is only correct provided if the spectrometer is absolutely calibrated, the atomic data are without errors and the current density profile of the beam is known. The absolute calibration of the spectrometer is a difficult task, and therefore its accuracy is limited and can change with time (e.g. darkening of the window). The atomic cross-sections are normally regarded as more reliable in the energy dependence than in the absolute value, and finally the current density profile in particular of the doped beam is only approximately known. Therefore, it is necessary to calibrate the output of the code against measurements from other diagnostics. In general one calibration factor for each of the beam emission profiles used in the fitting routine is required (in the code the array: `m_factors`). Reliable measurements of the plasma core density are generally available, and therefore an automatic determination of the calibration factor would be possible on a shot-by-shot basis. However, this calibration of the system is actually only required in case the calibration of the spectroscopic system has changed.

4.5.2 Initial metastable population

The fast neutral helium beam consists of atoms produced by charge exchange from accelerated ions; these atoms are either in the 1^1S ground state or in one of the two metastable states 2^1S and 2^3S. In the following the population of the latter two at the entry of the beam into the plasma is called the initial metastable population.

The initial beam composition is of large influence on the intensity, as well as on the shape of the beam emission profiles. This is due to the fact that the metastable population of a fast neutral He beam decays by orders of magnitude from the initial population to the equilibrium value inside the plasma. The decay length is typically of the order of 100 mm. Fig 4.7 shows the beam attenuation modelled for a JET discharge, and its decay-lengths are approximated through exponential fits. One can see that an equilibrium for the 2^1S state is only reached at about 200 mm inside the plasma.

For the correct n_e- and T_e-deduction an accurate knowledge of the initial metastable population is important. However, at the moment there are no independent measurements available under the conditions of a neutraliser of the heating beam (cf. chapter 2.6.2).

The initial metastable singlet (2^1S) population leads to a characteristic hump, in the singlet beam emission profile. This hump can be used to obtain a reasonably accurate estimate of the initial metastable singlet population in the beam.

A change in the initial metastable triplet population (2^3S), on the other hand, does not change the shape of the triplet beam emission profile. This can be explained by the fact that the metatstable triplet population shows an exponential decay through the plasma without reaching an equilibrium level. The entire triplet beam emission is therefore dominated by the initial triplet population. The actual initial metatstable triplet fraction can therefore only be estimated within the accuracy of the absolute calibration.

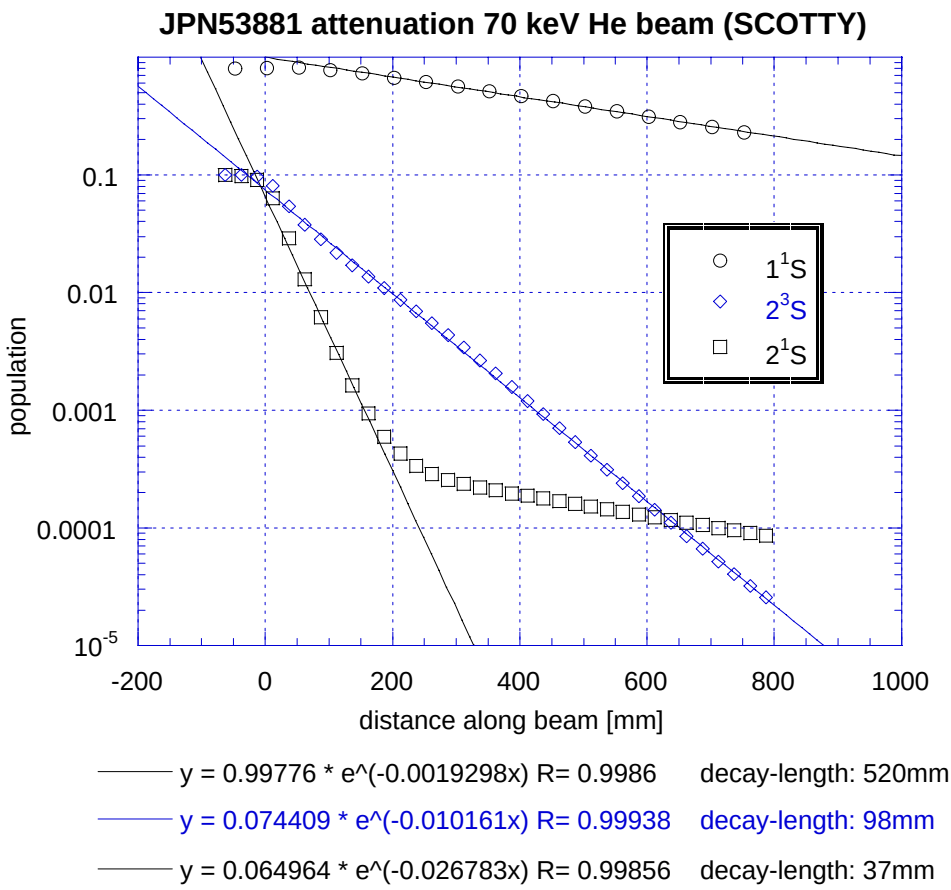

Fig 4.7: He beam attenuation of initially populated levels, modelled for the JET discharge 53881.

<u>Accuracy for estimating the initial metastable singlet population:</u>

In order to assess the possibility of determining the initial 2^1S population from the shape of the singlet emission profile (e.g.: 2^1P-3^1D / 667.8 nm), the `yttocs` code was tested with synthetic data (see chapter 4.2). Emission data where generated for an initial metastable population of 1% singlet (2^1S) and 10% triplet (2^3S) – this is marked with the solid black dot in Fig 4.8.

`Yttocs` gives the possibility to include the initial singlet population in the variation procedure – i.e. the initial singlet population is derived by the code. Running the code with a wide range of initial triplet populations produces the initial singlet populations plotted in Fig 4.8. The correct initial singlet population is reproduced within a 20% error margin when the

initial metastable triplet fraction is varied between 0 – 20%. This means that it is possible to get a good estimate of the initial metastable singlet fraction for the full range of initial metastable triplet fractions which can be expected under the experimental conditions used.

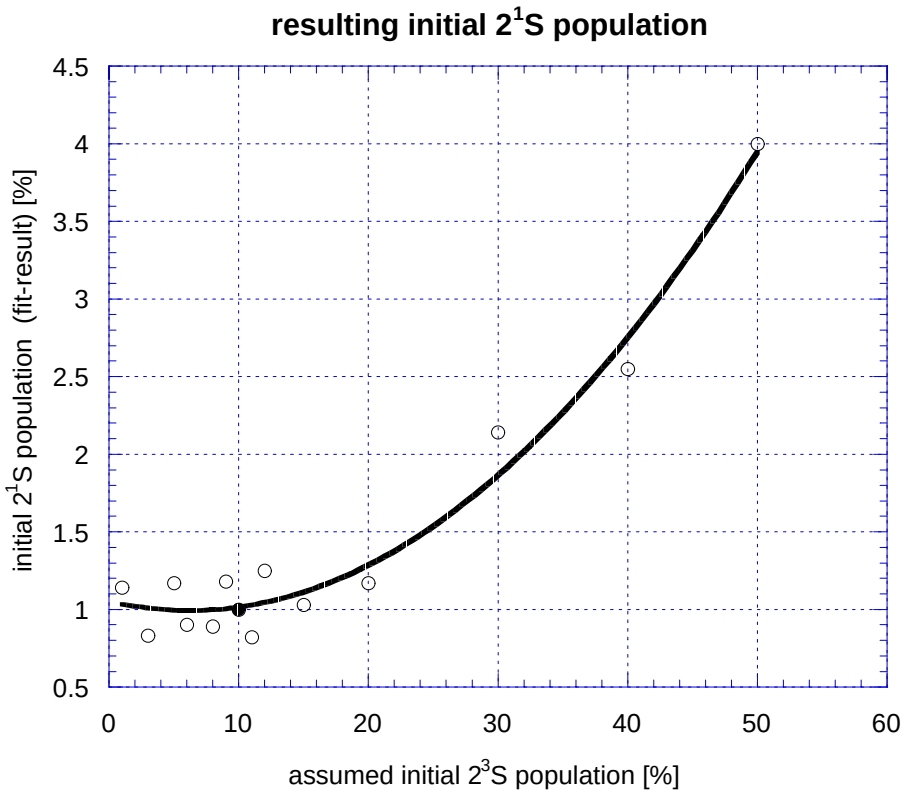

Fig 4.8: Initial metastable singlet population (2^1S), derived by the `yttocs` code, for synthetic data generated with initial metastable populations of 1% singlet (2^1S) and 10% triplet (2^3S) states (solid black dot). The open points represent the derived initial singlet population for a given initial triplet population. For up to 20% 2^3S population not much difference of the 2^1S population is found.

4.5.3 Finite resolution of the observation system

Because of the finite size of the observation volumes the modelled emission profile needs to be smeared out somewhat to reproduce the measurement. The active volume covers typically some 40 mm of the beam trajectory (depending on the instrument and the line-of-sight), and an additional factor for the finite diameter of the heating beam (typically ∅150 mm).

4.6 Comparison with evaluation procedures for other beam emission diagnostics

For the thermal He beam diagnostics line intensity ratios are used to derive the local electron temperature and density. The origin for line rations which are mainly sensitive to either electron temperature or -density is the different behaviour of the rate-coefficients for spin-changing (population of the triplet- out of the singlet system) and spin-conserving electron collisions (for details see [44]).

For the fast He beam line ratios which are mainly sensitive to one of these parameters do not exist anymore, because of the following reasons:

1) The generation of a fast neutral He beam from accelerated He ions via charge exchange leads to significant initial populations of metastable states (2^1S and 2^3S), which are by orders of magnitude higher than their equilibrium levels, which in the fast beam will be reached after passing through a sufficiently large section of the plasma. In a pure ground state beam, singlet-to-triplet line rations are mainly sensitive to temperature. Due to the different collisional life times of singlet and triplet metastable states, this feature is lost.
2) At higher energies (>2keV) the impact of proton collisions cannot be neglected anymore [45].
3) The light collected from a thermal He beam gives a local information directly from the collection volume (also called: active volume). In contrast to this, for the fast He beam the emitted light originating from a given position is the sum from processes along the beam trajectory preceding this position. To extract the desired density- and temperature profiles a non-local deconvolution technique must be applied, similar to that used for fast Li beam diagnostics [46].

5. Summary, Conclusions, and Outlook

In order to assess if the emission from fast He beams can be used for electron density- and -temperature diagnostics of fusion plasmas, HeI beam emission experiments have been performed at two relevant TOKAMAK Experiments, namely JET (Joint European Torus / largest TOKAMAK world-wide) and AUG (ASDEX Upgrade / Germany), by making use of the neutral beam heating systems to generate either a pure He beam or a doped He/D beam, as neither experiment has a dedicated fast diagnostic beam. For the spectroscopic measurements of the HeI beam emission the CX-diagnostic systems were used on both machines. The diameter of the heating beam defines the spatial resolution of the beam emission profile. Using a comparatively large heating beam results in a low resolution of the resulting beam emission profile which is therefore only of limited use for plasma edge diagnostics. However, it is sufficient for the presented proof-of-principle experiments. At AUG, beam emission experiments were performed using a pure 30 keV He beam and a 60 keV doped beam, respectively. At JET the octant 4 injector was used to generate both pure and doped He beams with about 75 keV beam energy, and the octant 8 injector to generate a 135 keV doped He/D beam.

The doping of D-heating beams with He worked so successfully and reliably at both machines that the so called diagnostic beam source could be used for the experiments with doped helium beams. As the spectroscopic systems were aligned to this diagnostic beam it provided the most favourable viewing geometry. The doping of the diagnostic beam does not reduce the available NBI power and since the timing of the He doping is freely selectable it gives access to interesting phases of plasma discharges.

The first beam emission experiments in 1999 were carried out parasitically during steady state phases of the plasma discharge, and plasma operation was only affected by the restriction that for the respective pulse the CX diagnostic was not available for ion temperature measurement. The signal intensities of $n = 3 \rightarrow 2$ and $n = 4 \rightarrow 2$ HeI lines have been assessed, and it has been investigated whether the Doppler-shifted HeI peak can be easily recognised and separated from other emission in the close spectral vicinity. In both machines it has been observed that the HeI beam emission appears in the spectra as clean Doppler-shifted peak and is thus largely undisturbed by impurity peaks for most of the wavelengths.

For the doped He/D-beams only one singlet (2^1P-3^1D) and two triplet lines (2^3P-3^3D and 2^3P-3^3S) could be measured with sufficient signal-to-noise ratio. On either end of the visible range the sensitivity of the CCD-sensor was low, yielding a weak signal in spite of a relatively intensive beam emission (e.g. 2^3S-3^3P at 388.9 nm). With the pure He beam also the emission profile of the 501.5 nm line (2^1S-3^1P) could be measured.

At AUG, HeI beam emission profiles for the two strongest lines (transition 2^1P-3^1D at 667.8 nm and 2^3P-3^3D at 587.6 nm) were obtained for four

different discharges. Repetitive measurements allowed additionally to estimate the scatter in the data to ±10%. A systematic deviation of some channels indicates a non-perfect calibration, which was partly due to an unfavourable alignment of the CER viewing-lines to the beam axis.

At JET singlet and triplet HeI beam emission profiles with good spatial resolutions could be obtained as a result of dedicated experiments, using radially swept high clearance L-mode plasmas. The problem of inaccurate calibration of the spectroscopic systems could partially be overcome by the in-situ cross-calibration of neighbouring channels.

The shapes of the singlet and the triplet HeI beam emission profiles are significantly different. The triplet emission profiles are dominated by the initial fraction of the 2^3S population and its strong attenuation when passing through the plasma. The triplet emission is therefore peaked and only measurable in the outer part of the plasma - 200 mm in case of AUG and 300 mm in case of JET. The intensity of the equilibrium emission further inside the plasma is much lower and could not yet be resolved by the spectroscopic systems.

The singlet beam emission profile could be observed over the full range from the plasma edge to its centre. However, even the most intensive singlet HeI beam emission (2^1P-3^1D) was about by one order of magnitude lower in intensity than the maximum of the strongest triplet emission (2^3P-3^3D). As the equilibrium emission can be measured, emission originating from the initial metastable 2^1S population can be seen as a significant peak near the plasma edge. This emission is again dominated by the strong attenuation of the metastable singlet population passing through the plasma.

By comparing model calculations with the measured profiles an initial metastable 2^1S fraction of about 1 % for a doped He beam and less then 0.5% for a pure He beam could be determined. The initial metastable fraction differs as the neutraliser target consists mainly of deuterium in case of a doped He/D-beam and helium in case of a pure He beam.

It is expected that the metastable population is predominantly in the 2^3S state. The exact composition of the metastable fraction could not be derived, as this would require an absolute measurement of the beam emission signal.

The impurity content of the plasma has been varied by puffing alternatively CD_4 or D_2 into the discharge for some pulses. It could be observed that Z_{eff} has an influence on the shape of both singlet and triplet emission profiles. In particular, the peak width of the triplet emission profiles becomes smaller with increasing Z_{eff}.

The code for modelling of the HeI beam emission (`scotty`) has been rewritten in order to meet the requirements of the reversion code (reduced run-time) and to increase the number of independent states involved. The new code (`scotty_fwd`) was designed as a subroutine and optimised in performance. The atomic data are accessed via look-up tables generated by the ADAS 311 code. In case of the new `scotty_fwd` code a modified ADAS 311 code

(not part of the official ADAS release) was used, which represents the atomic data in projections that are more suitable for beam modelling. Good agreement between modelled and measured beam emission profiles has been obtained for the singlet emission. A significant mismatch is however observed between modelled and measured triplet emission profiles. It is likely that the generation of the look-up tables by the modified ADAS 311 code is responsible for the discrepancy. Due to manpower restrictions on the ADAS side it was not possible to solve the problem in the time frame of this work. Therefore it was only possible to test the reversion code with synthetic data generated with the same look-up tables.

The newly developed reversion code (`yttocs`) for the determination of electron density and -temperature is based on the variation of the respective profiles. Starting from an initial guess for electron density and –temperature, the code adapts these profiles iteratively until calculated and measured emission profiles are well matched. The convergence of the code with synthetic data and realistic noise levels is satisfactory. The singlet beam emission (e.g. 2^1P-3^1D) is used to determine the electron density- and the triplet emission to determine the electron temperature profile. As the singlet emission was visible over the whole plasma range but the triplet emission is limited to the outer part, the density can be determined over the whole range while the temperature determination is limited to that range where the triplet emission is actually visible (outer 300 mm). The quality of the results depends largely on the accuracy of the atomic data, therefore additional effort in bringing the data-base up to date would be beneficial. The influence of the impurity content (Z_{eff}) on the beam emission is already included in the reversion code, but only as a global parameter. The potential of developing this sensitivity to impurity levels into a Z_{eff}-profile diagnostic has to be examined further.

The profiles obtained from the JET sweep experiments are suitable for testing of the beam model and the development of the reversion code. However, emission profiles of this quality are only available for one pulse type (L-mode). For benchmark purposes and further development of the code, beam emission profiles from other pulse types with different electron temperature- and -density profiles are needed.

In-situ cross-calibration of neighbouring channels by sweeping the plasma across the viewing-lines was very successful at JET. The application of this method to AUG would improve the quality of the emission profile. Since the last measurements the alignment and calibration of the CER diagnostic at AUG has been improved, which should lead to a higher beam emission signal and a lower scatter of the profiles. The settings of the spectrometer (slit width and exposure time) offers an additional handle for optimising the signal intensity.

For the strongest lines the noise are dominated by the plasma even at an integration time of only 50 ms, and therefore also the prospect of measuring

plasma fluctuations is given. This would require a faster detector with a higher sensitivity (e.g. photomultiplier tubes with interference filters).

For routine application of the fast He beam as a plasma edge diagnostic a dedicated diagnostic beam is essential, as the diameter of the heating beam limits the spatial resolution. HeI beam emission spectroscopy based on He-doped heating beams gives valuable additional information to the existing CX- and BE-spectroscopy. As all these measurements are made with the same observation system they originate at the same location. This reduces uncertainties otherwise introduced by mapping errors. Furthermore, the HeI beam emission spectrum is much simpler than the complex D_α-spectrum. This has already been exploited for the cross calibration and could also be beneficial for measuring plasma fluctuations.

In summary, the results of this thesis show convincingly that fast He beam emission spectroscopy can be used as an electron density- and -temperature diagnostics particularly for the plasma edge. Furthermore, there is some prospect for other diagnostic applications (impurity profiles, plasma fluctuations).

Appendix A

Bibliography

[1] M.G. von Hellermann, and H.P. Summers, JET report JET-P(93)34 (1993)[1]

[2] R.C. Isler, L.E. Murray, S. Kasai, J.L. Dunlap, S.C. Bates, P.H. Edmonds, E.A. Lazarus, C.H. Ma, M. Murakami, Phys. Rev. A 24 2701 (1981)

[3] R.J. Groebner, F.H. Brooks, K.H. Burrell, L. Rottler, Appl. Phys. Lett. 43 920 (1983)

[4] R.J. Fonck, D.S. Darrow, K.P. Jaehnig, Phys. Rev. A 29 3288 (1984)

[5] A. Boileau, M. von Hellermann, L.D. Horton, J. Spence, and H.P. Summers, Plasma Physics Controll. Fusion 31 779-804 (1989)

[6] W.L. Rowan, R.D. Bengtson, R.V. Bravenec, H. He, J. Jagger, D.M. Patterson, D.W. Ross, P.M. Valanju, A.J. Wootton, E.S. Marmar, J.H. Irby, J.A. Snipes, and J.L. Terry, Rev. Sci. Instrum. 68 300-3 (1997)

[7] R.J. Fonck, P.A. Duperrex, S.F. Paul, Rev. Sci. Instrum. 61 3487 (1990)

[8] R.D. Durst, E.R. Denhartog, R.J. Fonck, J.S. Kim, and Y. Karzhavin, Rev. Sci. Instrum. 66 842-4 (1995)

[9] G. Schilling, S.S. Medley, and S.J. Zweben, Rev. Sci. Instrum. 61 2940-2 (1990)

[10] H. Evensen, D. Brouchous, D. Diebold, M. Doczy, R.J. Fonck, and D. Nolan, Rev. Sci. Instrum. 63 4928-30 (1992)

[11] F.M. Levinton, R.J. Fonck, G.M. Gammel, R. Kaita, H.W. Kugel, E.T. Powell, D.W. Roberts, Phys. Rev. Lett. 63 2060 (1989)

[12] K. Takiyama, T. Katsuta, H. Toyota, M. Watanabe, K. Mizuno, T. Ogawa, T. Oda, J. Nucl. Mater. 241-43 1222-7 (1997)

[13] N. Nishino, H. Kubo, A. Sakasai, Y. Koide, N. Akaoka, T. Sugie, Y. Tsukahara, T. Ito, and H. Takeuchi, Rev. Sci. Instrum. 62 2695-9 (1991)

[14] R. Gianella, JET report JET-P(93)47 (1993)

[1] Publication officer, JET Joint Undertaking, Abingdon OX14 3EA, United Kingdom

[15] E.V. Aleksandrov, V.V. Alfrosimov, E.L. Berezovskii, A.B. Izvozchikov, V.I. Marasev, A.I. Kislyakov, E.A. Mikhailov, M.P. Petrov, and G.V. Roslyakov, JETP Lett. 29 1 (1979)

[16] A. A. E. van Blokland, E.P. Barbian, A.J.H. Donné, A. F. van der Grift, T. W. M. Grimbergen, Th. Oyevaar, F.C. Schüller, H.F. Tammen, H.W. van der Ven, T.F. Vijverberg, and F.D.A. de Winter, Rev. Sci. Instrum. 63 3359-68 (1991)

[17] H. Takeuchi, K. Tobita, Y. Kusama, M. Nemeto, T. Itoh, Y. Tsukahara, and JT-60 team, Rev. Sci. Instrum. 59 1652-7 (1988)

[18] G. Schilling, T.A. Kozub, S.S. Medley, and K.M. Young, Rev. Sci. Instrum. 57 2060-2 (1986)

[19] A.H. Sarkissian, Rev. Sci. Instrum. 69 923-5 (1998)

[20] E.S. Marmar, J.L. Terry, W.L. Rowan, and A.J.R. Wootton, Rev. Sci. Instrum. 68 265-8 (1997)

[21] T. Itoh, S. Matsuda, M. Matsuoka, Y. Ohara, M. Shitomi, and K. Watanabe, Proc. 4th Int. Symp. on Heating in Toroidal Plasma. Int. School of Plasma Phys., Varenna, Italy, June 1984, 2 1081-6 (1984)

[22] Y.J. Kim, R.A. Breun, D.A. Brouchous, and R.J. Fonck, Rev. Sci. Instrum. 61 3046-8 (1990)

[23] A.S. Schlachter, J.W. Stearns, and W.S. Cooper, Rev. Sci. Instrum. 59 1729-31 (1988)

[24] Y. Kusama, K. Tobita, T. Itoh, M. Nemeto, Y. Tsukahara, H. Kimura, and H. Takeuchi, Rev. Sci. Instrum. 61 3220-2 (1990)

[25] E. Wolfrum, F. Aumayr, E. Hintz, D. Rusbült, R. P. Schorn, D. Wutte, and HP. Winter, Rev. Sci. Instrum. 64 2285-92 (1993)

[26] B. Schweer, M. Brix, and M. Lehnen, J. Nucl. Mater. 266-269 673-8 (1999)

[27] W. Mandl, *"Development of Active Balmer-Alpha Spectroscopy at JET"*, PhD Thesis, JET report JET-IR(92)05 [1]

[28] H. D. Falter, M. Proschek, S. Menhart, F. Aumayr, D. Ciric, S. Cox, A. Dines, D. Godden, N. Hawkes, T. T. C. Jones and HP. Winter, Rev. Sci. Instrum. 71 3723-7 (2000)

[29] S. Menhart, *"On the applicability of fast neutral He beams for fusion plasma diagnostics"*, PhD Thesis, TU Wien / Austria[2]

[30] HP. Summers, Atomic data analysis structure, user manual, JET internal report JET-IR(94)06 1994[1]

[31] H. Anderson, PhD thesis, Univ. of Strathclyde, Glasgow (1999)

[32] G. Dragosits *"Modellierung von Heliumstrahlen in Randschichtplasmen"*, project report, TU Wien / Austria[2]

[33] N. Hawkes and N. Peacock, Rev. Sci. Instrum. 63 5164(1992)

[34] N. Hawkes, *"Experimental Studies of Ion Pressure, Impurity Flows and their Influence on Transport in the JET Tokamak"*, PhD thesis, Imperial Collage of Science, Technology and Medicine (1995)

[35] W.G.F. Blair, R.W. McCullough, F.R. Simpson, and H.B. Gilbody, *"Excitation of helium in He^+-H4 and He-He collisions: The influence of metastable helium atoms"*, J. Phys. B: Atom. Molec. Phys. 6 1265-1276 (1973)

[36] R.S. Hemsworth et. al., *"Nerutralisation mearurements for the JET injector"*, Proc. 13th Conf. on Contr. Fus. and Plasma Heating, Schliersee. FDR. 297-300 (1986)

[37] R.S. Hemsworth et. al. *"Testing of the upgrade JET neutral injector"*, proc. 12th Symp on Fusion Enfineering, Monterey, CA, IEEE Cat No 87CH 1 2507-2 (1987)

[38] H.B. Gilbody, K.F. Dunn, R Browing, and C.J. Latimer, *"Formation of metastable helium atoms by electron capture during the passage of fast He^+ ions through gases"*, J. Phys. B: Atom. Molec. Phys. 4 800-813 (1971)

[39] H.B. Gilbody, K.F. Dunn, R Browing, and C.J. Latimer, *"Electron loss from fast metastable and ground state helium atoms in passage through gaseous targets"*, J. Phys. B: Atom. Molec. Phys. 3 1105-1112 (1970)

[40] http://www.ipp.mpg.de/~spek/home.html

[41] C.B. Markwardt, *"mpfit"*, http://cow.physics.wisc.edu/~craigm/idl/fitting.html

[42] J. Moré, B. Garbow, and K. Hillstrom, *minpack-1*, Argonne National Laboratory, http://www.netlib.org/minpack/

[2] Institut für allgemeine Physik, TU Wien, Wiedner Hauptstr. 8-10, A-1050 Wien, Austria

[43] M. Proschek, S. Mendart, H.D. Falter, H. Anderson, H.P. Summers, A. Stäbler, P. Franzen, H. Meister, J. Schweinzer, T.T.C. Jones, S. Cox, N. Hawkes, F. Aumayr, and HP. Winter, Proc. 18th IAEA Fusion Energy conference, Sorrento, Italy (2000)

[44] M. Brix, "*Messung von Elektronentemperatur und -dichte mittels Heliumstrahl-diagnostik im Randschichtplasma eines Tokamaks*", PhD Thesis, Ruhr-Universität Bochum (1998)

[45] M. Brix, Abschlußbericht zum Forschungsauftrag Nr. 021/41362607/930 an die Forschungszentrum Jülich GmbH (1999)

[46] J. Schweinzer, E. Wolfrum, F. Aumayr, M. Pöckl, HP. Winter, R.P. Schorn, E. Hintz, and A. Unterreiter, Plasma Phys. Contr. Fusion 34 1173-83 (1992)

Appendix B

List of Abbreviations

ADAS	**A**tomic **D**ata and **A**nalysis **S**tructure
ASDEX	**As**symetric **D**ivertor **Ex**periment
AUG	**A**SDEX **U**p**g**rade
BES	**B**eam **E**mission **S**pectroscopy
CCD	**C**harge **C**oupled **D**evice (optical sensor array)
CER	**C**harge **E**xchange **R**ecombination (Spectroscopy)
CXRS	**C**harge E**x**change **R**ecombination **S**pectroscopy
ECE	**E**lectron **C**yclotron **E**mission
EFIT	**E**quilibrium **Fit**ting (code for calculating shape and position of the flux surfaces)
ELM(s)	**E**dge **L**ocalised **M**ode(s)
FWHM	**F**ull **W**idth at **H**alf **M**aximum
GRC(s)	**G**eneralised Collisional **R**adiative **C**oefficient(s)
H-mode	**H**igh confinement mode (improved edge confinement)
IDL	**I**nteractive **D**ata **L**anguage by Research Systems Inc.
ITB	**I**nternal **T**ransport **B**arrier
JET	**J**oint **E**uropean **T**orus
JPF	**J**ET **p**ulse **f**ile (JET database for raw data)
JPN	JET puls number
LCFS	**L**ast **C**losed **F**lux **S**urface
LIB	**Li**thium-**B**eam
L-mode	**L**ow confinement mode
MHD	**M**agneto-**H**ydro-**D**ynamic

List of Abbreviations (cont.)

MSE	**M**otional **S**tark **E**ffect (Diagnostic)
NBI	**N**eutral **B**eam **I**njection
NIB	**N**eutral **I**njection **B**ox
NTM	**N**eo-classical **T**earing **M**ode
PINI	**P**ositive **I**on **N**eutral **I**njector (Plug In Neutral Injector)
PPF	**p**rocessed **p**ulse **f**iles (JET database for derived signals)
SNR	**S**ignal to **N**oise **r**atio
TOKAMAK	**To**roidalnaya **Ka**mera sz **Ma**gnitnimi **K**atuschkami = toroidal chamber with magnetic coil (a particular magnet configuration for fusion plasmas)

List of Symbols

$\mathbf{n_e}$	electron density [1/m³]
$\mathbf{T_e}$	electron temperature [eV]
$\mathbf{Z_{eff}}$	effective nuclear charge (Z_j ... charge of impurity j) $$Z_{eff} = \frac{\sum_j n_j Z_j^2}{\sum_j n_j Z_j}$$
$\mathbf{R_{maj}}$	Major radius of the TOKAMAK plasma [m]
z	distance along beam axis [mm] ($z = 0$ for LCFS)

`Computer codes and their names are written in this font.`

Danksagung

Ich möchte mich an dieser Stelle herzlich bei meinem Doktorvater, Herrn o. Univ.-Prof. Hannspeter Winter für die Anregung dieser Arbeit und deren stete Förderung bedanken. Vor allem meine damit verbundenen Aufenthalte bei JET und AUG waren für mich sehr lehrreich. Durch das Vertrauen, das er in mich gesetzt hat, hatte ich auch während längerer Auslandsaufenthalte weitgehende Freiheit. Die zahlreichen internationalen Workshops und Konferenzen, die ich dank Prof. Winter besuchen konnte, haben mir einen Einblick in die multidisziplinäre Welt der Fusionsforschung gewährt und auch sehr zu meiner Motivation beigetragen.

Besonders dankbar bin ich Herrn Dr. Hans Falter von dessen Erfahrung ich während unserer engen Zusammenarbeit sowohl fachlich als auch persönlich sehr profitieren konnte. Nicht zuletzt dank seiner Hilfe wurde ich bei JET so herzlich aufgenommen. Mit seinen Anregungen, Diskussionen und Hilfestellungen hat er wesentlichen Anteil am vorliegenden Ergebnis.

Für die zeitaufwendigen Korrekturen dieser Arbeit bin ich neben Hans Falter auch Prof. Winter zu Dank verpflichtet.

Den Kollegen aus der Arbeitsgruppe in Wien und vor allem deren Leiter Friedrich Aumayr bin ich für zahlreiche kritische Diskussionen und für das angenehme Arbeitsklima dankbar, das während der gesamten Zeit herrschte.

Und zu guter letzt verdanke ich dem Zufall, dass ich von meinem letzten Aufenthalt in Oxford meine nunmehrige Lebensgefährtin Rebecca mit nach Hause bringen konnte.

Diese Arbeit wurde im Rahmen der Assoziation EURATOM-ÖAW durchgeführt und von der Friedrich Schiedel-Stiftung für Energietechnik gefördert.

Further acknowledgements

I am very grateful to the JET team and in particular to Dragoslav Ciric, Carin Giroud, N. Hawkes, Tim Jones, Andy Meigs and Klaus-Dieter Zastrow for all their support and advice. Out of the colleagues from the European associations I met at JET, in particular Mathias Brix has been very supportive in numerous discussions. The excellent teamwork and the professional and friendly attitude of this team is greatly apreciated.

I want to thank specifically Mathias Brix, but also many other colleagues from European associations from the good teamwork I found at JET.

From the AUG team I am particularly thankful for the help from Hans Meister, Joe Schweinzer, Albrecht Stäbler and Lisl Wolfrum. Furthermore, I would like to thank Prof. Hugh Summers from Strathclyde University, Glasgow for his support and advice.